

A STUDY OF PARTON DYNAMICS AT LOW x WITH ZEUS AT HERA

by

SABINE WEDAM LAMMERS

A dissertation submitted in partial fulfillment of the
requirements for the degree of

DOCTOR OF PHILOSOPHY

(PHYSICS)

at the

UNIVERSITY OF WISCONSIN – MADISON

2004

© Copyright by Sabine Wedam Lammers 2004

All Rights Reserved

Abstract

Inclusive jet production in neutral current deep inelastic positron-proton scattering has been measured for boson virtualities $Q^2 > 25 \text{ GeV}^2$. The data were taken at the HERA collider with center-of-mass energy $\sqrt{s} = 300 \text{ GeV}$ using the ZEUS detector and correspond to an integrated luminosity of 38.7 pb^{-1} . Jets were identified using the longitudinally invariant k_T -cluster algorithm. Measurements of differential inclusive jet cross sections are presented as functions of jet transverse energy (E_T^{jet}), jet pseudorapidity (η^{jet}), Q^2 and Bjorken x with $E_T^{jet} > 6 \text{ GeV}$ and $-1 < \eta^{jet} < 3$. The data are compared to leading-logarithm parton-shower model predictions and next-to-leading-order QCD calculations using DGLAP evolution and parametrizations of the proton parton distribution functions.

Measurements are made in three phase space regions, each one more restrictive, in order to enhance the contribution from events which may be better characterized by BFKL parton evolution. A large discrepancy between data and theory as computed with the NLO calculation at high η_{jet} and low x_{Bj} is seen in the most inclusive measurement. This discrepancy is largely diminished when limiting the phase space, and is, therefore, not attributed to BFKL dynamics. In the most limited region of phase space, a small discrepancy is again seen between data and theory, and may indicate the onset of BFKL dynamics. However, the theoretical uncertainties are very large, and a definitive statement can only be made once an improved theoretical calculation, perhaps implemented with BFKL parton dynamics, is made available.

Acknowledgements

Thanks to my advisor, Wesley Smith, for giving me the opportunity to learn and work at DESY. His knowledge of structure functions has helped me understand my measurement in a wider context and his dedication to the success of his students is awesome.

Thanks to Juan Terron, without whose intimate knowledge of jet physics and whose creativity and intellectual leadership, this analysis would never have been realized.

Thanks to Doug Chapin and Richard Cross, for helping me through the teething stage of learning HERA physics and the CFLT.

Thanks to Nils Krumnack for many useful insights throughout the development of the analysis and for being so generous with his time.

Thanks to all the members of the ZEUS Wisconsin Group: Don, Matti, Sascha, Dorian, Liang, Adam, Pat and Michelle for many good discussions, plus lots of laughs over the last couple of years.

Thanks to Erich Lohrmann, for being an exemplary physicist and for simply taking an interest.

Thanks to Eram Rizvi for being such a good friend and the best housemate anyone could ask for.

Thanks to Enrico Lunghi for being wonderful.

Thanks to all my friends in Hamburg and beyond. Life without my friends would be unimaginable.

Finally, the greatest thanks goes to my family, whose unwavering support and love have made hurdles easy to overcome, accomplishments all the more sweet, and life so rich.

Contents

Abstract	i
Acknowledgements	ii
1 Introduction - Basics of Particle Physics	1
2 Theoretical Overview - Highlights of Perturbative QCD	5
2.1 Hadron Spectroscopy	5
2.2 Confinement and Asymptotic Freedom	7
2.3 Running Coupling and Renormalization	8
2.4 Deep Inelastic Scattering	9
2.4.1 Quark Parton Model	12
2.4.2 QCD improved parton model	14
2.4.3 Factorization and Parton Density Functions	17
2.4.4 Solution to the DGLAP Evolution Equations and the Leading-Log Approximation	19
2.4.5 Double Leading-Log Approximation	21
2.4.6 BFKL Evolution	22
2.5 From Theory to Experiment	25
3 Experimental Setup	27
3.1 HERA Collider	27
3.2 ZEUS Experiment	29
3.2.1 Uranium-Scintillator Calorimeter	31

3.2.2	Central Tracking Detector	33
3.2.3	Trigger System	34
3.2.4	Luminosity Measurement	37
3.2.5	Detectors for Correcting Electron Measurements	38
3.2.5.1	Hadron-Electron Separator	38
3.2.5.2	Preshower Detectors - Presampler and SRTD	38
4	Event Generators and Detector Simulation	41
4.1	The Monte Carlo Approach	41
4.2	Parton Density Functions (PDF's)	42
4.3	Parton Shower Evolution	43
4.3.1	Matrix-Element and Parton Shower Models (MEPS)	43
4.3.2	Color Dipole Model	44
4.4	Hadronisation Models	45
4.4.1	Lund String Model	46
4.4.2	Cluster Fragmentation	47
4.5	QED Effects	47
4.6	Detector Simulation	48
5	NLO QCD Predictions	49
5.1	DISENT Program	51
5.1.1	Subtraction Method for Singularity Cancellations	51
5.1.2	Implementation	52
5.2	Theoretical Predictions and Uncertainties	52
5.2.1	Renormalization Scale Dependence and Uncertainty	52
5.2.2	Parton Density Functions and Uncertainties	53
5.3	Hadronisation Corrections	53
6	Jet Physics in DIS at HERA	55
6.1	Reconstruction of the Kinematic Variables	55

6.1.1	Double-Angle Method	56
6.1.2	Electron Method	57
6.1.3	Jacquet-Blondel Method	58
6.2	Jet algorithms	59
6.3	Breit Frame	61
7	Event Selection	65
7.1	Triggering on DIS Events	65
7.1.1	GFLT	66
7.1.2	GSLT	66
7.1.3	TLT	67
7.2	Offline Event Reconstruction	68
7.2.1	Positron Reconstruction	69
7.2.2	Jet Reconstruction	69
7.2.3	Jet Energy Correction	69
7.2.4	Cuts to Reject Background	70
7.2.5	Phase Space Selection	71
8	Description of the analysis	77
8.1	Inclusive Jet Measurement	80
8.1.1	Comparison of Data and Monte Carlo	81
8.1.2	Purities, Efficiencies, Correction Factors	84
8.1.3	Resolutions	86
8.1.4	ISR/FSR Corrections	86
8.2	QPM Suppressed Phase Space Measurement	89
8.2.1	Comparison of Data and Monte Carlo	89
8.2.2	Purities, Efficiencies, Correction Factors	91
8.2.3	Resolutions	91
8.2.4	ISR/FSR Corrections	91

8.3	BFKL Forward Jet Measurement	96
8.3.1	Comparison of Data and Monte Carlo	96
8.3.2	Purities, Efficiencies, Correction Factors	97
8.3.3	Resolutions	98
8.3.4	ISR/FSR Corrections	98
9	Results	103
9.1	Measurement of the Inclusive Jet Cross Section	103
9.2	Measurement of the Inclusive Jet Cross Section in the QPM Suppressed Phase Space .	111
9.3	BFKL Forward Jet Cross Section	116
9.4	Systematic Uncertainties	120
10	Conclusion	129

List of Tables

1.1	Properties of the fermions (quarks and leptons) and gauge bosons	2
2.1	Classification of the light hadrons	6

List of Figures

2.1	Deep Inelastic Scattering Microscope	10
2.2	Schematic of the proton with varying Bjorken x	10
2.3	Kinematic reach of DIS experiments	11
2.4	Quark Parton Model Feynman Diagram	12
2.5	Measurements of the structure function F_2	15
2.6	Diagrams of the QCD Splitting Functions	16
2.7	Gluon Ladder	20
2.8	The structure function F_2 versus x	22
2.9	Parton Evolution Schemes	24
3.1	HERA Ring	28
3.2	History of HERA Luminosity	29
3.3	The Zeus Detector	30
3.4	BCAL module	32
3.5	Cross sectional x-z slice of the Zeus Calorimeter	33
3.6	One CTD Octant	34
3.7	ZEUS Trigger and Data Acquisition System	36
3.8	The ZEUS Luminosity Monitor System	37
3.9	Rear Presampler and SRTD Boundaries	39
4.1	Diagram of the Hadronization Process	42
4.2	MEPS approach to parton showers as implemented in LEPTO	43

4.3	CDM approach to parton showers as implemented in ARIADNE	45
4.4	Hadronization scheme according to the Lund String and Cluster Fragmentation Models	46
4.5	QED radiation diagrams	47
5.1	Boson Gluon Fusion Diagrams with real and virtual gluon emissions.	50
5.2	Hadronization correction uncertainty	54
6.1	Lines of constant hadronic angle in $x - Q^2$ plane	56
6.2	Lines of constant electron angle in $x - Q^2$ plane	58
6.3	The QPM and QCD-Compton diagrams in the Breit Frame	62
6.4	Distribution in x_{Bj} for events with jets selected in the lab frame versus breit frame . .	63
6.5	Cell boundaries in laboratory and Breit frames	64
7.1	Jet Energy Correction	70
7.2	Event picture from Inclusive Phase Space sample	74
7.3	Event picture from QPM Suppressed Phase Space sample	75
7.4	Event picture from QPM Suppressed Phase Space sample	76
8.1	Comparison of data and MC for kinematic and hadronic quantities in Inclusive Phase Space	81
8.2	Comparison of data and MC for event variables in Inclusive Phase Space	82
8.3	Comparison of data and MC for jet quantities in Inclusive Phase Space	83
8.4	Jet finding efficiency and purity for Inclusive Phase Space	84
8.5	Event finding efficiency and purity for Inclusive Phase Space	85
8.6	$Q^2, E_{T,jet}, \eta_{jet}$ resolution for Inclusive Phase Space	87
8.7	QED corrections for cross sections in the Inclusive Phase Space	88
8.8	Comparison of data and MC for kinematic and hadronic quantities in QPM Suppressed Phase Space	89
8.9	Comparison of data and MC for event variables in QPM Suppressed Phase Space . . .	90
8.10	Comparison of data and MC for jet variables in QPM Suppressed Phase Space	91

8.11	Jet finding efficiency and purity for QPM Suppressed Phase Space	92
8.12	Event finding efficiency and purity for QPM Suppressed Phase Space	93
8.13	$Q^2, E_{T,jet}, \eta_{jet}$ resolution for QPM Suppressed Phase Space	94
8.14	QED corrections for cross sections in the QPM Suppressed Phase Space	95
8.15	Comparison of data and MC for kinematic and hadronic quantities in the BFKL Phase Space	96
8.16	Comparison of data and MC for event quantities in the BFKL Phase Space	97
8.17	Comparison of data and MC for jet variables in QPM Suppressed Phase Space	98
8.18	Jet finding efficiency and purity for the BFKL Phase Space	99
8.19	Event finding efficiency and purity for the BFKL Phase Space	100
8.20	$Q^2, E_{T,jet}, \eta_{jet}$ resolution for the BFKL Phase Space	101
8.21	QED corrections for cross sections in the BFKL Phase Space	102
9.1	Inclusive jet cross section as a function of the jet pseudorapidity	104
9.2	Inclusive jet cross section as a function of the jet transverse energy	106
9.3	Inclusive jet cross section as a function of Q^2	108
9.4	Inclusive jet cross section as a function of x_{Bj}	109
9.5	The total inclusive DIS cross section and the inclusive jet cross section in the variables Q^2 and x_{Bj}	110
9.6	Inclusive jet cross section as a function of the jet pseudorapidity in the QPM suppressed phase space	111
9.7	Inclusive jet cross section as a function of the jet transverse energy in the QPM sup- pressed phase space	113
9.8	Inclusive jet cross section as a function of Q^2 in the QPM suppressed phase space . . .	114
9.9	Inclusive jet cross section as a function of x_{Bj} in the QPM suppressed phase space . .	115
9.10	Inclusive jet cross section as a function of the jet pseudorapidity in the QPM suppressed phase space	116
9.11	Inclusive jet cross section as a function of the jet transverse energy in the QPM sup- pressed phase space	117

9.12	Inclusive jet cross section as a function of Q^2 in the QPM suppressed phase space . . .	118
9.13	Inclusive jet cross section as a function of x_{Bj} in the QPM suppressed phase space . .	119
9.14	Systematic uncertainties for cross sections in the Inclusive Phase Space	122
9.15	Systematic uncertainties for cross sections in the Inclusive Phase Space	123
9.16	Systematic uncertainties for cross sections in the QPM Suppressed Phase Space	124
9.17	Systematic uncertainties for cross sections in the QPM Suppressed Phase Space	125
9.18	Systematic uncertainties for cross sections in the BFKL Phase Space	126
9.19	Systematic uncertainties for cross sections in the BFKL Phase Space	127

Chapter 1

Introduction - Basics of Particle Physics

The birth of particle physics began with relatively small scattering experiments. For example, the Rutherford experiment which scattered alpha particles off gold foil led to the observation that the atom contains a very heavy, dense core, later to be called the nucleus. Experiments like these were inspired by the first questions of particle physics: What are the building blocks of matter and how do those building blocks interact? One hundred years later, those are still the questions driving and directing particle physics research.

Subsequent to the Rutherford experiments, the nucleus of the atom was discovered to contain protons and neutrons and to be enveloped by a cloud of electrons. The proton and neutron were discovered to be made up of particles called quarks which, along with leptons such as the electron, are the most fundamental, i.e. structureless, building blocks of the atom currently known.

Much like the organization of the chemical elements into the Periodic Table, a classification of the fundamental particles observed in nature according to certain rules has been made that reflects the results of many scattering experiments. Much like Rutherford's method of analyzing the topology of the scattered electrons to infer the existence of substructure in the nucleus of the atom, modern particle physics experiments observe final state properties of particles in high-energy scattering experiments. These lead to a natural classification system describing the properties of the particles observed in nature. For example, the quarks and leptons can be classified according to their charge, spin and mass as shown in Table 1.

Quarks are objects which are not observed isolated in nature. Rather, what we observe are combinations of quarks, called mesons (2-quark systems) and baryons (3-quark systems). In addition

Flavor	Charge	Spin	Mass
up	$+\frac{2}{3}$	$\frac{1}{2}$	3 MeV
down	$-\frac{1}{3}$	$\frac{1}{2}$	6 MeV
charm	$+\frac{2}{3}$	$\frac{1}{2}$	1.2 GeV
strange	$-\frac{1}{3}$	$\frac{1}{2}$	120 MeV
top	$+\frac{2}{3}$	$\frac{1}{2}$	174 GeV
bottom	$-\frac{1}{3}$	$\frac{1}{2}$	4.25 GeV
electron	-1	$\frac{1}{2}$	0.51 MeV
muon	-1	$\frac{1}{2}$	106 MeV
tau	-1	$\frac{1}{2}$	1.78 GeV
ν_e	0	$\frac{1}{2}$	< 3 eV
ν_μ	0	$\frac{1}{2}$	< 0.19 MeV
ν_τ	0	$\frac{1}{2}$	< 18.2 MeV
γ	0	1	0
W^\pm	± 1	1	80.4 GeV
Z	0	1	91.2 GeV
gluon	0	1	0

Table 1.1: Properties of the fermions (quarks and leptons) and gauge bosons

to charge, spin and mass, these hadrons (multi-quark systems) display properties such as baryon number, strangeness and isospin [1], which allow us to further distinguish them from each other. Each combination of these properties, or quantum numbers, gives rise to a unique particle that can be observed in nature. A plethora of particles have been observed and new resonances are still being discovered.

Particle physics, in addition to classifying the matter particles, tries to understand how these particles interact. There are, up to now, four known forces in nature: gravity, the weak nuclear force, electromagnetism and the strong nuclear force. These forces are carried by particles. The electromagnetic force is mediated by photons. The two forces that act only at very small distances, the weak and strong nuclear forces, are mediated by the W and Z particles (weak) and the gluon (strong). These particles, although they can be described by the same properties (i.e. mass, spin, charge, etc.) as the quarks and leptons, obey very different physical laws. As a result, particle physics categorizes all the fundamental particles into two groups: fermions, which describe the behavior of quarks and leptons, and bosons, which describe the behavior of the force mediators.

The Standard Model of particle physics represents our understanding of both the classification

schemes of the fundamental particles, and the way these particles behave. It is based on the principles of quantum field theory, and has successfully described almost all experimental data which has tested the weak and strong nuclear forces.

The goal of this thesis is to make a test of an application of the theory of the strong nuclear force, Quantum Chromodynamics (QCD). In particular, to test whether the currently accepted understanding of how quarks and gluons interact with each other inside the proton is valid in heretofore unexplored values of the momentum of the parton (quark or gluon) inside the proton. Access to these energies is given by deep inelastic electron-proton scattering (DIS), in which an electron and proton collide. As the electron and proton approach each other, a photon is emitted from the incoming electron which breaks the proton apart in the collision. The particles emitted in the collision undergo a process of showering and clustering before depositing their energy in the detector. By measuring the energy and position of the final particles entering the detector, we can extrapolate back to the initial particles that came out of the collision and perform a statistical analysis of the final state topologies in order to test predictions of QCD.

This measurement is concerned with a certain class of DIS events in which a highly collimated stream of final-state particles, called a jet, is located in the forward region (direction of the incoming proton) of the detector. The data used for this analysis were collected by the ZEUS experiment during the 1996 and 1997 running periods. Events in which the parton participating in the collision has a small fraction of the proton's momentum and which contain a forward jet may not be well described by the conventional QCD prescription, the one where the parton dynamics in the proton are given by the DGLAP equation (see Sec. 2.3.3). We have attempted in this analysis to uncover a kinematic region in which the DGLAP prescription begins to lose relevance, and where a possible transition to BFKL dynamics (another QCD prescription for the interaction between quarks and gluons) may be applicable. Such a discovery would have important implications for QCD, because it would show that the calculational approach to modeling how the partons behave under QCD is valid in a different kinematical regime.

Three measurements of the forward jet cross section are described in this thesis, each in turn more focused on the region where the BFKL prescription is expected to gain relevance. The data are

compared to the most accurate QCD calculations currently available, in which the strong coupling constant is calculated to second order. The parton momentum dependence for this calculation is given by the DGLAP QCD evolution, so a deviation between data and the theoretical prediction could indicate the onset of BFKL dynamics. The theoretical background and challenges are discussed in more detail in Chapter 2. A detailed description of the accelerator, detector, and data acquisition are found in Chapter 3. Chapter 4 describes the Monte Carlo programs used for unfolding the cross section and determining various corrections that need to be applied. Chapter 5 describes the program used for the theoretical calculation we use to compare to the data measurements. An overview of the issues relevant to making a jet measurement is given in Chapter 6. The event selection and reconstruction are described in Chapter 7. Chapter 8 holds the description of the unfolding of the cross section and studies performed that substantiate the result. Chapter 9 holds the final cross sections and Chapter 10 summarizes the conclusions drawn from the measurements.

Chapter 2

Theoretical Overview - Highlights of Perturbative QCD

This theoretical background to the measurement begins with some of the historical precursors to the development of QCD which were fundamental strides in developing the Standard Model. The classification of observed particles and resonances (known to us as mesons and baryons) in the early days of modern particle physics are introduced, along with the vital concepts of confinement and asymptotic freedom, which are the cornerstones on which QCD is built. Because this analysis is a test of the QCD prescription for parton evolution, a more detailed explanation of factorization and the evolution equations are given in the latter part of the chapter.

2.1 Hadron Spectroscopy

Quarks are not free particles, but cluster into groups of two or three to form bound states called hadrons. When these hadronic resonances were first being observed, starting in the late 1940's, they were not recognized as bound states of confined quarks. An accounting system for classification of the hadrons based on their mass and quantum numbers (charge and strangeness) was proposed independently by both Gell-Mann and Ne'eman in 1961, in which the hadrons are members of an $SU(3)$ symmetry group. The scheme, called the "Eightfold-Way", involved making unique assignments of the quantum numbers to each hadron according to certain patterns, and was substantiated when it correctly predicted the mass and quantum numbers of the hadrons not observed up until that point. The light hadrons, which we now know are made up of the light up, down and

strange quarks, are given in Table 2.1.

Mesons		Baryons	
$J^P = 0^-$	1^-	$\frac{1}{2}^+$	$\frac{3}{2}^+$
$\pi^0 (u\bar{u})$	ρ^+	p	$\Delta^{++} (uuu)$
$\pi^+ (u\bar{d})$	ρ^0	n	$\Delta^+ (uud)$
$\pi^- (d\bar{u})$	ρ^-	Λ	$\Delta^0 (udd)$
$\eta (d\bar{d})$	ω	Σ^+	$\Delta^- (ddd)$
$K^+ (u\bar{s})$	K^{*+}	Σ^0	$\Sigma^{*+} (uus)$
$K^0 (d\bar{s})$	K^{*0}	Σ^-	$\Sigma^{*0} (uds)$
$K^- (s\bar{u})$	K^{*-}	Ξ^0	$\Sigma^{*-} (dds)$
$\bar{K}^0 (s\bar{d})$	\bar{K}^{*0}	Ξ^-	$\Xi^{*0} (uss)$
$\eta' (s\bar{s})$	Φ		$\Xi^{*-} (dss)$
			$\Omega^- (sss)$

Table 2.1: Classification of light hadrons in the Meson Nonet and Baryon Decuplet. The quark constituents are given in parentheses.

The hadrons are separated into two groups according to their spin quantum number, which can be thought of as the particle's inherent angular momentum. Mesons, or two-quark systems have integer spin, while baryons, or three-quark systems, have half-integer spin. Each one of these groups is divided again into two, once again according to the spin, J^P , where J is the spin of the particle (either 0 or 1 for mesons and 1/2 or 3/2 for baryons) and P is the parity quantum number used to reflect mirror symmetry (either + or -).

Gell-Mann and Zweig proposed the concept of quarks in 1964 as a basis of the SU(3) symmetry, which later became the foundation for the quark-parton model of the proton. One major problem with the Eightfold-Way classification was the existence of the Δ^{++} , Δ^- and Ω^- particles, which, once identified as bound states of three identical quarks, violated the Pauli exclusion principle. In 1964, O.W. Greenberg proposed a solution by introducing a new quantum number: color. There are three basic colors: red, green and blue, corresponding to the three color states the quark can be found in. Similarly to anti-charge, the three colors have corresponding anti-colors, \bar{r} , \bar{g} and \bar{b} . The hadrons observed in nature do not carry a color charge, rather they are always produced as color-singlets. This implies that either the total amount of color is zero, i.e. there is as much color as anti-color contributing from the quarks or all three colors are present in equal amounts [2].

2.2 Confinement and Asymptotic Freedom

Although hadron spectroscopy and the Eightfold-Way had great success in classifying the hadrons, the Quark Model that evolved from it had a major unresolved question: Why aren't quarks, if they really are the fundamental constituents of hadrons, observable in nature? Having fractional charge, they should have been fairly easy to detect. Skepticism of the quark model was laid to rest, however, through a series of experimental discoveries beginning with the early deep inelastic scattering experiments at the Stanford Linear Accelerator Center (SLAC), which observed that the proton had substructure. Much like the Rutherford experiment that detected nucleon substructure, deep inelastic scattering, in which a high-energy beam of particles is fired into the proton, observed that the beam particles scattered off the proton in such a way to suggest three solid lumps of charge inside, i.e. the valence quarks. Furthermore, the proton structure did not depend on the distance scale at which the proton was being probed. This "scaling" behavior was expected if the electron scatters off point-like constituents. The subsequent discovery of the J/Ψ particle was described nicely by the Quark Model as a $c\bar{c}$ bound state [2].

During this period, the foundations of quantum field theory were being developed which ultimately made the Quark Model into a viable theory. Quantum field theory provided the needed framework to describe how all the quarks and hadrons interact. Richard Feynman gave the intuitive picture of the quark parton model (QPM - see Sec. 2.4.1) to understand Bjorken scaling in 1969. The proton was regarded as a collection of partons off which the probe scattered elastically and the deep-inelastic scattering cross section was just the incoherent sum of these individual cross-sections. [3]. Fundamental to quantum field theory is the notion that all the forces of nature are a result of particle exchange. With the emergence of Quantum Electrodynamics (QED) by Feynman, Schwinger and Tomonaga, followed by the addition of theory of the weak interactions by Glashow, Weinberg and Salam [4], predictions for the properties of the exchange particles mediating the electroweak force were made, and in 1983 the predictions were verified by the discovery of the W and Z particles at CERN. The photon, the mediator of the electromagnetic force can be described by the rules of Electroweak Theory as well. Quantum Chromodynamics (QCD), the quantum field theory describing the strong nuclear force, provided an explanation for confinement of quarks inside a nucleon.

The quarks are bound by this strong force, overruling the electromagnetic repulsion of same-signed charged quarks, and this force is mediated by the gluon. Gluons are the quanta of the color field that bind quarks in nucleons and also nucleons into nuclei, and quarks interact strongly by exchanging colored gluons.

Certain parallels can be drawn between the role of the exchange bosons in QED and the gluon in QCD. In addition, the mathematical formalism used to describe the strong and electromagnetic forces within the framework of quantum field theory is similar. One major difference, however, is that gluons, unlike photons, can couple directly to other gluons. In addition to the fundamental interaction between quarks and gluons, 3 and 4 gluon self-interactions are also possible. The strength of the strong interactions is given by the strong coupling constant, α_s , which is analogous to the electroweak coupling constant, α_{EM} , better known as the fine structure constant. Because α_{EM} has the small value of $1/137$, the perturbative approach used in quantum field theory to calculate the rate of observed interactions between elementary particles works well in QED. However, α_s varies according to the separation distance between the interacting particles. This property of QCD called asymptotic freedom was discovered in 1973 by Wilczek, Gross, Politzer and T'Hooft [5, 6]. It states that the strength of the interaction, or magnitude of the coupling, decreases at very short distances (around 0.1 fermi) and increases at very large distances. In the short distance limit, quarks and gluons can be treated as free particles since their coupling is small, and the ability to make perturbative calculations is restored [7].

2.3 Running Coupling and Renormalization

In the context of field theory, Feynman developed a graphical formalism for describing elementary particle interactions. These Feynman diagrams have rules associated with them for determining the amplitude, or rate, of a given process. A Feynman diagram for the deep inelastic scattering process is given in Fig. 2.4. The amplitude for one diagram does not, however, correspond to the amplitude for a given physical process. Among other effects, the self-interactions of the particles participating have to be included as well, for example, the splitting of a photon into an e^+e^- pair in QED or a gluon emitted from a quark and then reabsorbed in QCD. Each additional self-interaction in a Feynman diagram decreases the amplitude of that diagram if the coupling for the self-interaction

(i.e. α_{EM} for electromagnetic interactions and α_s for strong interactions) is small.

Predictions for an observable associated to a given scattering process are obtained by perturbative methods using the Feynman rules, which can be thought of as summing the amplitudes of all possible Feynman diagrams for that scattering process. In the calculation of diagrams with self-interacting loops, divergencies appear which originate from the integration over the loop momenta. They are called ultraviolet divergencies because they appear when the loop momenta tend to infinity (small wavelength). These singularities need to be removed via a renormalization procedure in which a cutoff μ_R on the loop momenta is introduced. As a result of this procedure, the strong coupling constant α_s acquires a dependence on μ_R . As μ_R is an arbitrary and unphysical parameter, the value of any physical observable should be independent of μ_R . The requirement is expressed mathematically through the Renormalization Group Equation:

$$\mu_R^2 \frac{dC}{d\mu_R^2} = \left(\mu_R^2 \frac{\partial}{\partial \mu_R^2} + \mu_R^2 \frac{\partial \alpha_s}{\partial \mu_R^2} \frac{\partial}{\partial \alpha_s} \right) C = 0 \quad (2.1)$$

where C is the physics observable of interest. The dependence of the strong coupling constant on the renormalization scale is shown in the second term inside the brackets of Eqn. 2.1. This dependence has been calculated explicitly and can be written in terms of a perturbative expansion in powers of α_s using the Callan-Symanzik β function.

$$\mu_R^2 \frac{d\alpha_s}{d\mu_R^2} = \beta(\alpha_s(\mu_R^2)) = -\beta_0 \alpha_s^2 - \beta_1 \alpha_s^3 - \beta_2 \alpha_s^4 - \dots \quad (2.2)$$

The β coefficients can be found in [8]. Incidentally, it was the calculation of the one-loop coefficient β_0 , which led to the discovery of asymptotic freedom in QCD. $\beta_0 = \frac{1}{4\pi}(11 - (\frac{2}{3}n_f))$ where n_f is the number of quark flavors in the theory. If n_f is smaller than 17, the coefficient β_0 is positive and when $\mu_R^2 = Q^2$, α_s tends to zero as Q^2 gets large. If there were 17 or more quark flavors, QCD would not be an asymptotically free theory.

2.4 Deep Inelastic Scattering

Deep Inelastic Scattering (DIS) is an ideal environment to study the strong nuclear force. DIS involves a probe (most often a lepton), colliding with a nucleon at high energy via an exchange boson and breaking up the proton. “Deep Inelastic” refers to the regime where the momentum transferred

by the lepton and the center of mass energy of the boson-nucleon system are larger than the mass of the nucleon [9].

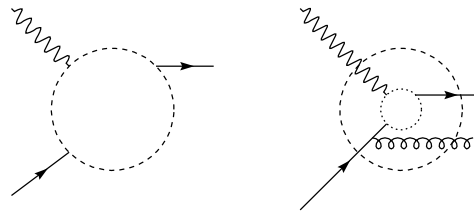


Figure 2.1: A visualization of how Deep Inelastic Scattering acts as a microscope for probing the structure of the proton. On the left, the photon probe has low momentum, and cannot resolve object inside the dotted line representing an area within the proton. On the right, the photon has higher momentum, allowing it to resolve shorter distances and more particles that then become visible [7].

As illustrated in Fig. 2.1, the distances which can be probed, and therefore the resolving power of the probe, is related to the energy of the probe by the equation $q = 1/\lambda$, where q is the momentum of the probe and λ is the DeBroglie wavelength of the probe. As an example, the left side of Fig. 2.1 illustrates how a low energy photon resolves the proton substructure up to the diameter given by the dotted circle. On the right side of the figure, a higher energy probe can probe smaller distances inside the proton, thus resolving particles like gluons.

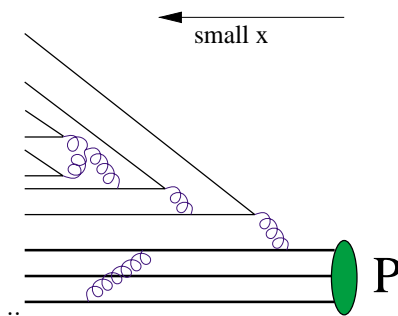


Figure 2.2: A schematic of the proton at varying values of the kinematic variable Bjorken x . The lower the value of x , the more phase space available for gluon radiation, which thereby increases the sea quark density as well.

Another important variable in describing the short-distance interactions is Bjorken x , which in the high proton momentum limit is the fraction of the proton's momentum carried by the parton participating in the scattering. As shown in Fig. 2.2, the lower the value of x , the more phase space is available for gluonic radiation inside the proton, thereby increasing the density of sea quarks.

The fixed target experiments which pioneered the study of deep inelastic scattering gave the first substantive understanding of how the quarks and gluons are distributed inside a proton, and provided an impressive confirmation of perturbative QCD. HERA, which collides 27.5 GeV electrons with 820 or 920 GeV protons to produce a center-of-mass energy $\sqrt{s} = 300/318$ GeV, is the first colliding experiment to study DIS. It has been named by some a “QCD-factory” due to the much larger center of mass energy compared to the fixed-target experiments, and to the greater kinematic reach, as shown in Fig. 2.3.

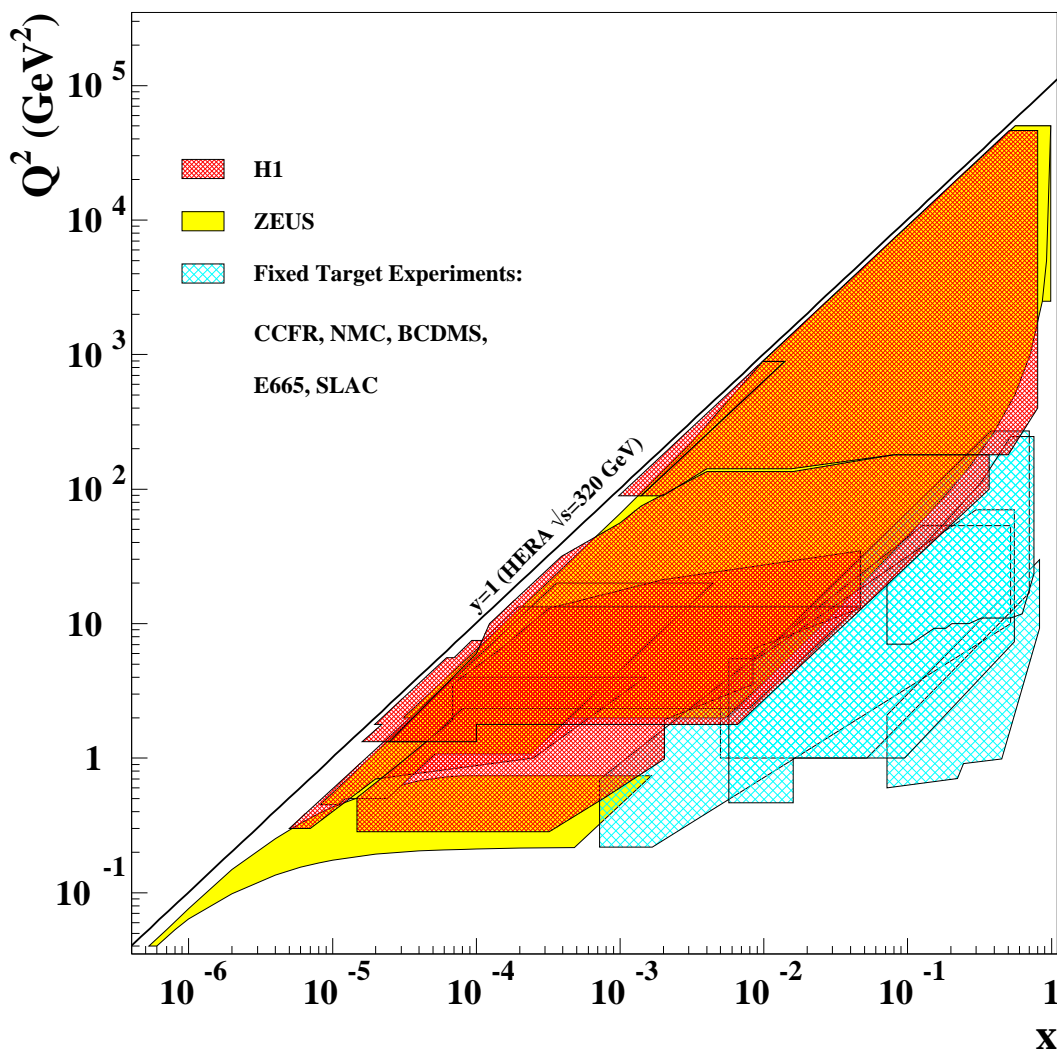


Figure 2.3: Kinematic reach of the DIS collider experiments, ZEUS and H1, and fixed target experiments. The collider experiments extended the measurable kinematic region by several orders of magnitude in x and Q^2 beyond that accessible to fixed target

2.4.1 Quark Parton Model

At lowest order, the DIS process at HERA is shown in Fig. 2.4. The lepton, in our case an electron or positron, with initial 4-momentum k interacts with a quark in the proton, with 4-momentum xp , via an exchange boson with 4-momentum q . The electron scatters at an angle θ_e and with momentum k' , while the recoiling quark scatters with angle γ_h and momentum $xp + q$. The proton remnant continues along the same trajectory as the incoming proton. The exchange boson can be either a photon, Z or W^\pm . In the case of the neutral photon and Z particles, the process is called neutral current DIS, and in the case of a charged W boson, the process is called charged current DIS. The DIS regime is specified kinematically by $Q^2 \gg 1\text{GeV}^2$, where Q^2 is defined below.

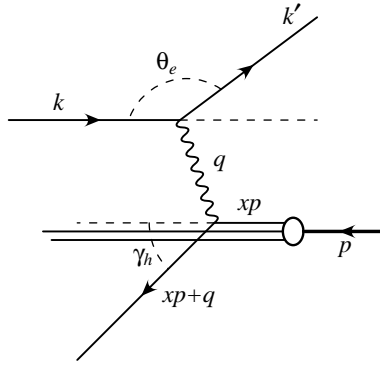


Figure 2.4: The Feynman Diagram of the lowest-order DIS process, the Quark-Parton Model process.

The DIS process can be characterized by a set of DIS variables. If \sqrt{s} is the center-of-mass energy of the electron-proton system, E_p and E_e are the incoming energies of the proton and electron respectively, the system is kinematically defined by

$$s = (k + p)^2 \simeq 4E_p E_e \quad (2.3)$$

$$q^2 = (k - k')^2 \quad (2.4)$$

In this quark-parton model picture, the relevant Lorentz-Invariant kinematic variables are:

$$Q^2 = -q^2 \quad (2.5)$$

$$x = \frac{Q^2}{2p \cdot q} \quad (2.6)$$

$$\nu = \frac{p \cdot q}{m_p} \quad (2.7)$$

$$y = \frac{q \cdot p}{k \cdot p} \quad (2.8)$$

Q^2 is the negative square of the four-momentum transfer which specifies the virtuality of the exchange boson. x is the Bjorken scaling variable which in the Quark-Parton-Model can be interpreted as the fraction of the proton momentum carried by the struck quark. y is the relative energy transfer between the lepton and the target hadron in the rest frame of the proton. Using the Mandelstam variables given in [8], it can be shown that the variables x , y and Q^2 are related by the square of the center-of-mass energy s .

$$Q^2 = sxy \quad (2.9)$$

In the experimental setting, these variables can be constructed from two measurements of the electron and hadronic systems, as described in Sec. 6.1.

DIS Cross Section

The total ep DIS cross section can be written in terms of its leptonic and hadronic tensors.

$$d\sigma = L_{\mu\nu}W^{\mu\nu} \quad (2.10)$$

The leptonic tensor, $L_{\mu\nu}$ can be calculated exactly from QED and is symmetric with respect to μ and ν exchange for an unpolarized beam of electrons. The hadronic tensor, $W^{\mu\nu}$, serves to parameterize the structure of the proton and the details of the interaction at the hadronic vertex. $W^{\mu\nu}$ can be written in terms of proton structure functions (for details see [7]), which are now used to parameterize the different contributions to the interaction. The ep differential cross section can be expressed in terms of these structure function by the equation

$$\frac{d^2\sigma(e^\pm p)}{dx dQ^2} = \frac{4\pi\alpha_s^2}{xQ^4} [Y_+ F_2(x, Q^2) - y^2 F_L(x, Q^2) \mp Y_- x F_3(x, Q^2)] \quad (2.11)$$

where $Y_\pm = 1 \pm (1 - y)^2$ and the initial lepton can have positive or negative charge. F_2 is the contribution to the cross section due to exchange of transversely and longitudinally polarized virtual bosons and is related to the density of quarks and anti-quarks in the proton. The longitudinal structure function, F_L , is the contribution due to longitudinally polarized bosons and is small. Finally,

F_3 is the contribution due to parity violating exchange of a Z-boson and only makes a significant contribution in the region $Q^2 > M_Z^2$.

The structure function F_2 has been studied in great detail by the ZEUS and H1 experiments at HERA, and measurements extracted from the total ep cross section in the ranges $6 \cdot 10^{-5} < x < 0.65$ and $1 \text{ GeV}^2 < Q^2 < 10^5 \text{ GeV}^2$. Fig. 2.5 shows the kinematic reach of the measurements as compared to the fixed target data.

Inherent in the Quark-Parton Model is the assumption that the quarks in the proton are the only particles and are point-like objects. This phenomenon can be tested with measurements of the proton structure as a function of Q^2 . For if there are only point-like objects in the proton, the structure function F_2 should be independent of the momentum of the probe, i.e. the resolution achieved in the scattering. No matter how high the resolution is, point-like objects will always be measured in the same way. This behavior was predicted by Bjorken as early as 1968 and confirmed with the fixed target DIS experiments. The scaling behavior can be seen at medium values of Bjorken x , e.g. $x=0.08$, in Fig. 2.5, and is violated at low and high values of x , which leads to the improved quark-parton model discussed in the next section.

2.4.2 QCD improved parton model

The Quark-Parton Model was also tested for momentum sum conservation. If the quarks are the only constituents of the proton, the sum of their momenta should add up to the momentum of the proton. Experimental evidence, however, indicated that the charged partons only added up to about half of the proton's momentum. To rectify this problem, it was proposed that the gluons of QCD, the neutral particles that mediate the strong force, accounted for the missing momentum. The structure function measurements reflect the existence of the gluon by exhibiting a dependence on the energy scale Q^2 , particularly at low values of x , as seen in Fig. 2.5. This behavior is called scaling violation. The structure function F_2 , as mentioned in the previous section, is a measure of the quark content in the proton. It can be written as:

$$F_2(x, Q^2) = \sum_i e_i^2 [xq_i(x, Q^2) + x\bar{q}_i(x, Q^2)] \quad (2.12)$$

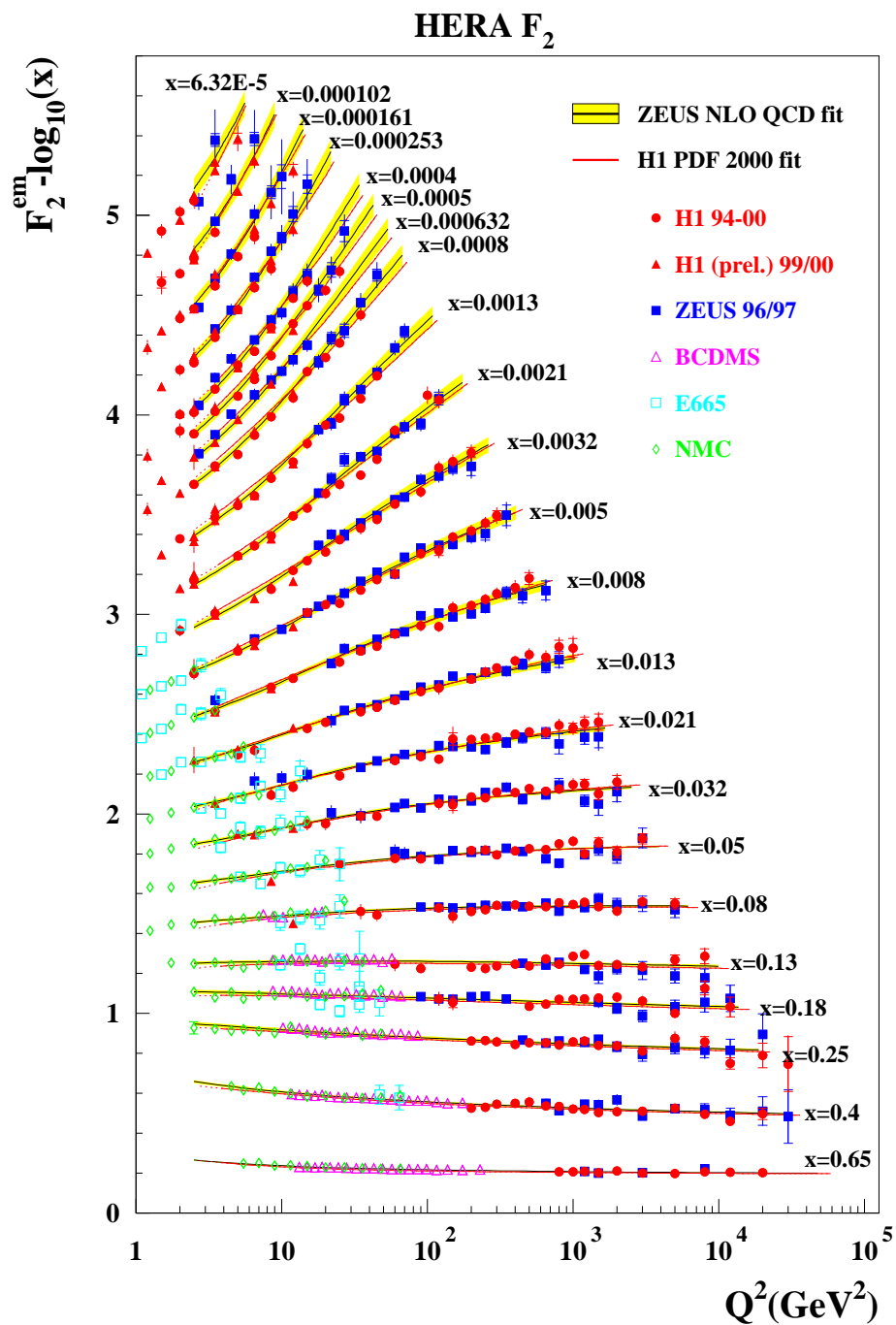


Figure 2.5: Measurements of the structure function F_2 by the HERA experiments ZEUS and H1, and fixed target experiments. HERA data span the kinematic region $6 \cdot 10^{-5} < x < 0.65$ and $1 \text{GeV}^2 < Q^2 < 10^5 \text{GeV}^2$. The F_2 measurement exhibits Bjorken scaling at medium values of x , and scaling violation at very low and high values of x [10].

where the sum is over quark flavors and anti-quark flavors. The functions $q(x, Q^2)$ and $\bar{q}(x, Q^2)$ can be thought of as the quark and antiquark densities in the proton (see Sec. 2.4.3). The interpretation of the rise of F_2 with Q^2 at low x as an indication of the gluon content is justified by the tenet of QCD that gluons can split into $q\bar{q}$ pairs, much like the $\gamma \rightarrow e^+e^-$ splitting in QED. So what is being measured is the additional quark content arising from that splitting, the so-called sea quark distribution. The splitting of the gluons is described in more detail in the next section.

The processes that comprise the fundamental interactions of the strong nuclear force are shown in Fig. 2.6. They are the splitting of a gluon into 2 (or 3) gluons, the gluon splitting into a quark-antiquark pair, and a gluon radiating off a quark or antiquark. The coupling strength for all the processes are related to the strong coupling constant α_s . The P, or splitting, functions shown below each diagram represent the amplitude for each process. It is through combinations of these processes that the quarks interact with each other in the proton, and it is through gluon radiation that quarks acquire transverse momentum.

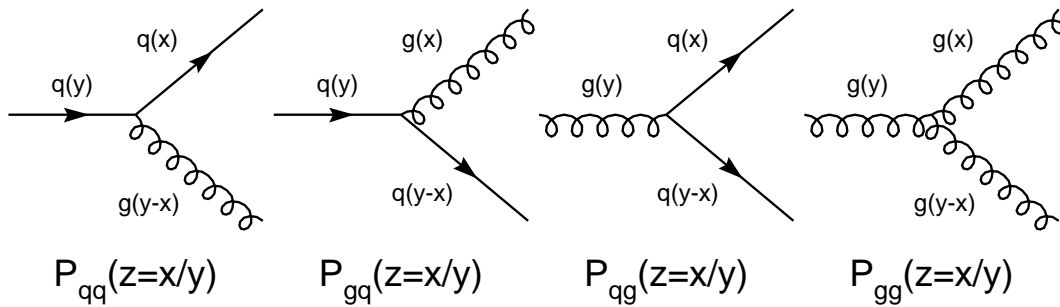


Figure 2.6: Diagrams of the QCD Splitting Functions

For “hard” processes in which α_s is small and the perturbative approach is valid, the splitting functions can be expanded in the series

$$P_{ij}(z, \alpha_s) = P_{ij}^0(z) + \frac{\alpha_s}{2\pi} P_{ij}^1(z) + \left(\frac{\alpha_s}{2\pi}\right)^2 P_{ij}^2(z) + \dots \quad (2.13)$$

The leading order splitting functions, P_{ij}^0 , have been calculated and are [8]:

$$\begin{aligned}
P_{qq}^0(z) &= \frac{4}{3} \left(\frac{1+z^2}{1-z} \right); \\
P_{gq}^0(z) &= \frac{4}{3} \left(\frac{1+(1-z)^2}{z} \right); \\
P_{qg}^0(z) &= \frac{1}{2} (z^2 + (1-z)^2); \\
P_{gg}^0(z) &= 6 \left(\frac{(1-z)}{z} + \frac{z}{1-z} + z(1-z) \right)
\end{aligned} \tag{2.14}$$

These are the leading order probabilities of a parton j emitting a parton i with momentum fraction z of the parent parton.

2.4.3 Factorization and Parton Density Functions

The Quark-Parton Model, coupled with QCD, was shown to work very well in the region where perturbative techniques are valid. This is the region where the partons inside the proton are asymptotically free and where Q^2 is large. However, quantifying the effect of scaling violation has two major challenges. The first arises from the fact that the full proton structure function cannot be calculated from first principles. There are contributions to the cross section that come from long-range interactions where α_s is large, which are non-calculable. Secondly, the partonic cross section that involves point-like interactions between the photon and parton suffer from logarithmic divergencies. These divergencies occur when a parton is either soft (low momentum) or collinear to its parent parton.

Both of these problems can be dealt with by using the concept of factorization. Similar to the renormalization procedure described in Sec. 2.3, an arbitrary factorization scale μ_F is introduced, in this case to separate the long-range and short-range processes. One introduces a parton distribution, $q(x, \mu_F^2)$ at the scale μ_F which is related to the probability of finding a parton with momentum fraction x inside the proton. This distribution is convoluted with the partonic cross section $\hat{\sigma}(x, \mu_F^2)$ to give the total DIS cross section:

$$\sigma_{DIS} = \sum_i q_i(x, \mu_F^2) \otimes \hat{\sigma}(x, \mu_F^2) \tag{2.15}$$

where the index i runs over all gluons and quark flavors. This parton distribution function is universal, that is once it is defined for one process, it can be applied to any other. The factorization scale

eliminates the divergencies in the partonic cross section by introducing a cutoff in the transverse momentum of the emitted parton. If the transverse momentum of the parton is below the value chosen for the factorization scale, it is absorbed into the parton distribution function. If it is above the factorization scale, it is included in the calculation of the partonic cross section.

The newly factorized parton distribution function takes the generalized form

$$q(x, \mu_F^2) = q(x) + \frac{\alpha_s}{2\pi} \int_x^1 \frac{dy}{y} q(y) f(P_{ij}^0, \mu_F) \quad (2.16)$$

where the P_{ij}^0 are the leading order QCD splitting functions given in the previous section. There are actually two separate expressions for the parton distributions, one for quarks which involve splitting functions P_{qq} and P_{qg} , and another for the gluon distribution function involving the splitting functions P_{gg} and P_{gq} . By differentiating Eqn. 2.16 with respect to the factorization scale μ_F , setting $\mu_F = Q$ and separating the pieces associated with quark radiation and gluon radiation, the following coupled equations are found:

$$\frac{dq_i(x, Q^2)}{d \ln Q^2} = \frac{\alpha_s(Q^2)}{2\pi} \int_x^1 \frac{dy}{y} \left(\sum_i q_i(y, Q^2) P_{qq}\left(\frac{x}{y}\right) + g(y, Q^2) P_{qg}\left(\frac{x}{y}\right) \right) \quad (2.17)$$

$$\frac{dg(x, Q^2)}{d \ln Q^2} = \frac{\alpha_s(Q^2)}{2\pi} \int_x^1 \frac{dy}{y} \left(\sum_i g(y, Q^2) P_{gg}\left(\frac{x}{y}\right) + q_i(y, Q^2) P_{gq}\left(\frac{x}{y}\right) \right) \quad (2.18)$$

where now the full splitting functions with its perturbative expansion in α_s (Eqn. 2.13) is included. These are the DGLAP equations [11, 12, 13, 14] which give the evolution of the parton density functions. The parton density functions given in Eqn. 2.16 cannot be calculated from first principles. In order to determine the PDF's, an initial distribution at a given x and Q^2 is extracted from measurements of the proton structure function. The x -dependence of the PDF is parameterized at the initial scale Q_0^2 and then evolved in Q^2 using the DGLAP equations.

The DGLAP equations cannot be solved analytically to all orders in α_s . Therefore, certain approximations are made in summing the terms included in the expressions of the splitting functions. These approximations result in limited kinematic applicability of DGLAP Evolution. The Leading-Log and Double Leading-Log approximations are outlined in the next sections, along with the assumptions made in their summation. BFKL, an alternative parton evolution scheme, has a different set of approximations, and therefore has a different region of applicability. The applicability

regions for all three schemes are shown in Fig. 2.9.

2.4.4 Solution to the DGLAP Evolution Equations and the Leading-Log Approximation

The DGLAP equations can be solved either by direct numerical integration step-by-step in $\log Q^2$ or by performing a moment analysis in the variable x [9]. We will outline how the latter calculation is performed when considering only the non-singlet distributions, defined as the difference between quark distributions (e.g. $u - \bar{u}$), which decouples from the evolution of the gluon distribution. The leading order DGLAP equation is

$$\begin{aligned} \frac{dq(x, Q^2)}{d \log Q^2} &= \frac{\alpha_s(Q^2)}{2\pi} \int_x^1 \frac{dy}{y} P_{qq}\left(\frac{x}{y}\right) q(y, Q^2) \\ &= \frac{\alpha_s(Q^2)}{2\pi} \int_0^1 dy \int_0^1 dz \delta(x - yz) P_{qq}(z) q(y, Q^2) \end{aligned} \quad (2.19)$$

Taking the moments of Eqn. 2.19, the equation factorizes and the resulting differential equation can be solved to give the Q^2 evolution of the moments. From Eqn. 2.19, the expression for the n^{th} moment is:

$$\begin{aligned} \int_0^1 \frac{dx}{x} x^n \frac{dq(x, Q^2)}{d \log Q^2} &= \frac{\alpha_s(Q^2)}{2\pi} \int_0^1 dy \int_0^1 dz \int_0^1 \frac{dx}{x} x^n \delta(x - yz) P_{qq}(z) q(y, Q^2) \\ &= \frac{\alpha_s(Q^2)}{2\pi} \int_0^1 \frac{dz}{z} z^n P_{qq}(z) \int_0^1 \frac{dy}{y} y^n q(y, Q^2) \end{aligned} \quad (2.20)$$

which when written more compactly is

$$\frac{dM_n(Q^2)}{d \log Q^2} = \frac{\alpha_s(Q^2)}{2\pi} A_n M_n(Q^2) = \frac{1}{b \log(Q^2/\Lambda^2)} A_n M_n(Q^2) \quad (2.21)$$

where $M_n(Q^2) = \int_0^1 \frac{dx}{x} x^n q(x, Q^2)$, $A_n = \int_0^1 \frac{dx}{x} x^n P_{qq}$ and $b = \beta_0$ of Eqn. 2.2. Λ is the fundamental QCD parameter which marks the boundary where asymptotic freedom is valid. Equation 2.21 can be readily solved giving

$$\begin{aligned} M_n(Q^2) &= c_n \left(\log \frac{Q^2}{\Lambda^2} \right)^{A_n/b} = c_n \exp\left(\frac{A_n}{b} \log\left(\log \frac{Q^2}{\Lambda^2}\right) \right) \\ &= c_n \sum_r \frac{1}{r!} \left(\frac{A_n}{b} \log\left(\log \frac{Q^2}{\Lambda^2}\right) \right)^r \end{aligned} \quad (2.22)$$

where c_n cannot be calculated from perturbation theory and so its value, via $M_n(Q_0^2)$ must be determined by experiment. Therefore, we know only the evolution of the moments and not their

absolute value. The r^{th} term of equation 2.22 can be shown to be equivalent to a ladder diagram with r rungs, when working in the axial gauge in which the gluon has only two physical polarization states. A ladder diagram, shown in Fig. 2.7, illustrates the process in which a quark or gluon in the proton interacts with a virtual photon after the emission of one or more gluons. A cascade

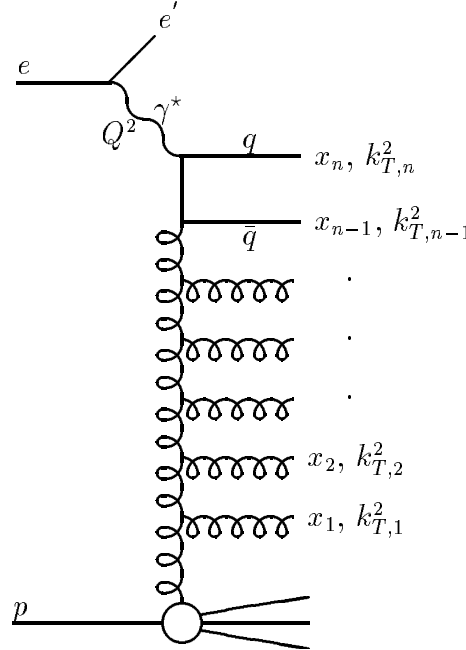


Figure 2.7: Gluon ladder diagram illustrating the parton cascade that culminates in the hard interaction with the photon probe. In the DGLAP approximation, the k_T of the partons are strongly ordered upwards along the ladder, while the longitudinal momenta are weakly ordered downwards along the ladder.

of gluonic radiation can take place, where each gluon is termed a “rung” in the ladder. The exact determination of the parton distributions requires the sum over a large number of Feynman diagrams, the sum of which can be thought of as the ladder diagram. This involves integrations over the transverse momenta k_T of the emitted partons along the ladder. This integration is difficult to perform without imposing a kinematic constraint on the partons. By requiring the parton emissions be strongly ordered in k_T ,

$$Q^2 \gg k_{T,n}^2 \gg \dots \gg k_{T,2}^2 \gg k_{T,1}^2, \quad (2.23)$$

one can order the integrals in a nested fashion, and perform the k_T integration over the n rungs of the gluon ladder in the following way:

$$\int^{Q^2} \frac{dk_{T,n}^2}{k_{T,n}^2} \frac{\alpha_s(k_{T,n}^2)}{2\pi} \int^{k_{T,n}^2} \frac{dk_{T,n-1}^2}{k_{T,n-1}^2} \frac{\alpha_s(k_{T,n-1}^2)}{2\pi} \dots \int^{k_{T,2}^2} \frac{dk_{T,1}^2}{k_{T,1}^2} \frac{\alpha_s(k_{T,1}^2)}{2\pi} \quad (2.24)$$

Each of these integrals gives rise to a term $\log(\log(Q^2/\Lambda^2))$. The form of these integral solutions is exactly the form of the terms obtained by the moment analysis (Eqn.2.22). Therefore, we infer that the DGLAP equations are equivalent to summing ladder diagrams with each additional rung contributing a term $\log(\log Q^2)$, thus earning the name Leading-Log Approximation. In this approximation, each parton evolves independently of the others in increasing virtuality and transverse energy, and decreasing momentum fraction. This thesis examines whether these approximations hold in the kinematic region covered by HERA.

2.4.5 Double Leading-Log Approximation

In the small x regime, one must consider terms that appear as $\log(1/x)$ in the perturbative expansion of the parton densities. At small x , the gluon density dominates, and so we treat only the gluon distribution that appears in Eqn 2.18. The DGLAP equation that sums the double leading log terms $(\alpha_s \log \frac{1}{x} \log \frac{Q^2}{Q_0^2})^n$ is

$$\frac{dg(x, Q^2)}{d \log Q^2} = \frac{\alpha_s}{2\pi} \int_x^1 \frac{dy}{y} g(y, Q^2) P_{gg} \quad (2.25)$$

In the small x limit, the splitting function P_{gg} has the limiting behavior $P_{gg} \rightarrow 6/x$ (see Eqn 2.13).

Then Eqn. 2.25 becomes

$$\frac{xdg(x, Q^2)}{d \log Q^2} = \frac{3\alpha_s}{\pi} \int_x^1 \frac{dy}{y} g(y, Q^2) \quad (2.26)$$

which can be solved to give the asymptotic behavior:

$$xg(x, Q^2) \sim \exp\left(2\left[\frac{3\alpha_s}{\pi} \log \frac{1}{x} \log \frac{Q^2}{Q_0^2}\right]^{\frac{1}{2}}\right) \quad (2.27)$$

As with the Leading-Log Approximation, we can identify the Double Leading-Log behavior exhibited in Eqn 2.27 with the sum of ladder diagrams. The strong k_T ordering is retained here, and a new ordering is imposed in the longitudinal momenta of the partons

$$x_n \ll x_{n-1} \dots \ll x_2 \ll x_1 \quad (2.28)$$

Again we have nested integrations, now in the longitudinal momenta of the partons,

$$\int_x^1 \frac{dx_{n-1}}{x_{n-1}} \dots \int_{x_2}^1 \frac{dx_1}{x_1} \int_{x_1}^1 \frac{dy}{y} yg(y, Q_0^2) = \frac{1}{n!} \left(\log \frac{1}{x}\right)^n G_0 \quad (2.29)$$

where G_0 is the small x limit of $xg(x, Q_0^2)$. When including the integrals in transverse energy of the partons, one obtains an expression for the gluon distribution that is equivalent to that found in Eqn. 2.27 [9].

2.4.6 BFKL Evolution

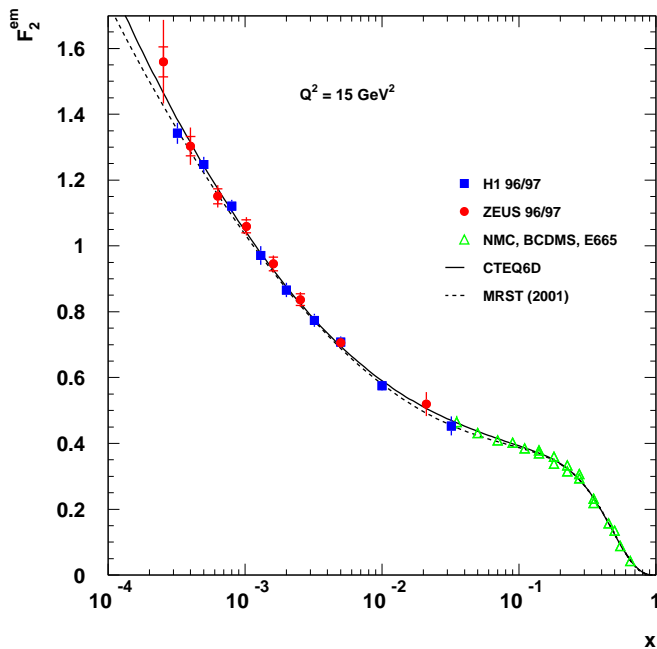


Figure 2.8: The structure function F_2 versus x for a fixed value of Q^2 . Shown are the data from ZEUS, H1 and the CTEQ and MRST PDF fits.

In the context of DIS at HERA, measurements can be made at quite low x values, but the kinematics constrain the value of Q^2 at low x . Although the DGLAP approximations given in the previous sections, $LL(Q^2)$ and $NLL(Q^2, 1/x)$ have been seen to agree with data, they are limited due to the fact that they apply perturbative calculations in a region where non-perturbative effects can be large. The splitting functions can be written as a perturbative expansion which include terms

$\log(1/x)$, but the DGLAP approximations do not include these terms.

Alternatively to the evolution in Q^2 in DGLAP, we would like to predict the evolution in x , starting from a given gluon distribution $g(x_0, Q^2)$. For moderate Q^2 we must sum the LL($1/x$) terms but keep the full Q^2 dependence, and not just the $LL(Q^2)$ terms. This means the approximation of the ordering in transverse energy of the partons on the ladder diagram can not be made, in order to integrate over the full k_T space. We can still picture the LL($1/x$) behavior as the sum of ladder diagrams, but in the Balitsky-Fadin-Kuraev-Lipatov (BFKL) [15, 16] resummation technique the ladder diagrams are actually an effective representation for a whole set of Feynman diagrams, most of which are a non-ladder type.

Due to the non-ordering of the partons, we must introduce the unintegrated gluon distribution, $f(x, k_T^2)$, which is written in terms of our original integrated gluon distribution $g(x, Q^2)$

$$xg(x, Q^2) = \int^{Q^2} \frac{dk_T^2}{k_T^2} f(x, k_T^2) \quad (2.30)$$

In the BFKL approach, the unintegrated gluon distribution may be written in the form of a recursion relation which relates the n -rung contribution f_n to the $(n-1)$ -rung contribution f_{n-1}

$$f_n(x, k_T^2) = \int_x^1 \frac{dx'}{x'} \int dk_T'^2 K(k_T, k_T') f_{n-1}(x', k_T'^2). \quad (2.31)$$

The BFKL equation is:

$$\frac{\partial f(x, k_T^2)}{\partial \log(1/x)} = \int dk_t'^2 K(k_T, k_T') f(x', k_T'^2) \quad (2.32)$$

where $K(k_T, k_T')$ is the BFKL kernel

$$K(k_T, k_T') = \frac{3\alpha_s}{\pi} k_T^2 \left[\frac{1}{k_T'^2 |k_T^2 - k_T'^2|} - \beta(k_T^2) \delta(k_T^2 - k_T'^2) \right] \quad (2.33)$$

with

$$\beta(k_T^2) = \int \frac{dk_T'^2}{k_T'^2} \left[\frac{1}{|k_T^2 - k_T'^2|} - \frac{1}{(4k_T'^4 + k_T^4)^{\frac{1}{2}}} \right] \quad (2.34)$$

The two terms in the bracket of 2.33 correspond to real gluon emission and virtual corrections respectively; the apparent singularity at $k_T^2 = k_T'^2$ cancels between these two contributions. For fixed α_s , the BFKL equation can be solved analytically, and its result has the form:

$$f(x, Q^2) = F(x, Q^2) \left(\frac{x}{x_0} \right)^{-\lambda} \quad (2.35)$$

where $\lambda = \frac{3\alpha_s}{\pi} 4 \log 2$. The form for the solution is particularly revealing, as it displays the same functional form as the measurements of the F_2 structure function, as seen in Fig. 2.8. For typical values of α_s , the power $\lambda \simeq 0.5$, which is a steeper rise of the structure function than what the experimental data reveal. Certain corrections, like including the running of α_s and the next-to-leading order (NLO) corrections to the BFKL equation are expected to reduce the value of λ [17].

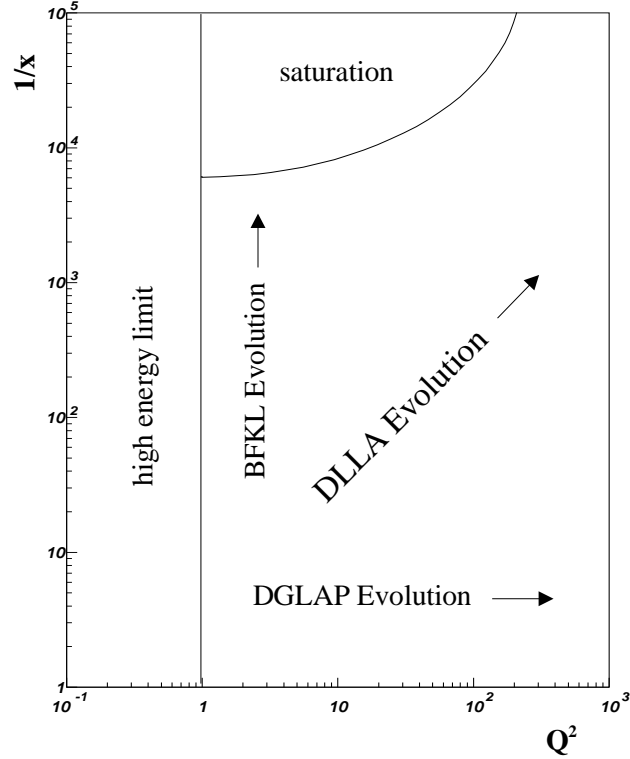


Figure 2.9: Parton Evolution Schemes using summation techniques in the LLA(Q^2) (DGLAP), DLLA and LLA($1/x$) (BFKL). The arrows indicate the regions of validity in the kinematic plane for each scheme. The saturation region is where the gluon density gets large such that the quanta of energy spatially overlap. In this region and in the high energy limit, perturbation techniques are not expected to be valid.

The full derivation of the BFKL summation and evolution equation involves the fundamentals of Regge Theory and is beyond the scope of this thesis. For a complete treatment, the reader is directed to [18]. However, Fig. 2.9 illustrates the important qualitative features of each evolution scheme discussed thus far. The LL(Q^2) approximation using DGLAP evolution in Q^2 occurs at fixed x and is valid where $\alpha_s \log Q^2 \sim 1$ but $\alpha_s \log(1/x)$ is small. The DLL($Q^2, 1/x$) approximation evolves in x and Q^2 but its validity is limited to the region $\alpha_s \log Q^2 \log(1/x) \sim 1$ but $\alpha_s \log Q^2$ and

$\alpha_s \log(1/x)$ are both small. Finally, BFKL evolution is used in the LL(1/x) approximation where $\alpha_s \log(1/x) \sim 1$ but $\alpha_s \log Q^2$ is small [9].

2.5 From Theory to Experiment

One way in which DGLAP and BFKL evolution might be distinguished from each other in the laboratory is by considering the strong ordering in transverse energy required of the partons along the gluon ladder, as shown in Fig. 2.7. Working under the assumption that, on average, each parton on the ladder hadronizes into a stream of particles, called a jet, and each resulting jet is isolated from its neighboring jet (also created by the hadronization of a neighboring parton), one can study the transverse energy distribution of the partons on the ladder by measuring the corresponding transverse energy distribution of the jets. In the DGLAP approach, the partons are strongly ordered in transverse energy, with the highest k_T parton existing at the top of the ladder. In the laboratory, this high k_T parton is more likely to appear with a large polar separation between it and the proton remnant. On the lower end of the ladder, the partons are expected to have quite low transverse energies and appear in the hadronic final state near the proton remnant. In the BFKL approach, this ordering in the gluon ladder is broken, and the partons are emitted democratically in transverse energy along the ladder. Therefore, an excess of high transverse energy partons at the bottom of the ladder, near the proton remnant, above the DGLAP prediction could be an indication of BFKL dynamics becoming important.

This technique, first proposed by Mueller and Navalet [19, 20], is implemented in this analysis by measuring the rate of jets in the forward region of the detector, near the proton remnant.

Chapter 3

Experimental Setup

The Deutsches Elektronen-Synkrotron (DESY) laboratory located in Hamburg, Germany was founded in 1959. It is the first high-energy physics laboratory to collide electrons and protons together, although it had a very successful high-energy program before the HERA ep-collider was built. The discovery of the gluon was made at the e^+e^- Petra collider, and many experiments using synchrotron radiation have been conducted using the Doris and Petra rings. The lab is funded and run by the German government, but many international universities and laboratories contribute to the experiments conducted, both in detector development and manpower. DESY's laudable relationship with the surrounding city is evidenced by the over 15,000 people who participate in DESY's "Tag der offenen Tuer," a so-called open-door day when the lab shuts down its operations and the public are invited to look through the facilities and learn about the experiments taking place. HERA is scheduled for decommissioning in early 2007, and DESY is proposing to construct a 500 GeV center-of-mass energy e^+e^- linear collider, TESLA.

3.1 HERA Collider

The Hadron Elektron Ring Anlage (HERA) saw first collisions in 1991 and had a successful luminosity program until 2000, when it was upgraded for high luminosity running. It collides 27.5 GeV electrons or positrons with 820 GeV (1992-1997 running)/920 GeV (1998-2000 running) protons to produce a center-of-mass energy of $300/318 \text{ GeV}^2$. The electron beam is generated by accelerating electrons in the Linac, then transferring the beam to the DESY and PETRA rings for further acceleration before injection into HERA. This staged injection process is necessary for controlling the

synchrotron radiation of the beam. The protons are generated by accelerating H^- ions in the Linac up to 50 MeV. These ions are then transferred to the DESY ring and further accelerated before the electrons are stripped and the protons are injected into PETRA. Once the protons reach 40 GeV in energy, they are injected into HERA.

The beams are organized into bunches of electrons and protons. Each electron bunch is designed to collide with a unique proton bunch. There are, in principle, 210 bunches distributed over the entire 6km. circumference of the ring, yielding a bunch spacing of about 96 ns. The particles enter the HERA ring after the injection process. Once in HERA, they are accelerated further using superconducting dipole magnets (for protons) and conventional dipole magnets (for electrons), and are focused with quadrupole magnets.

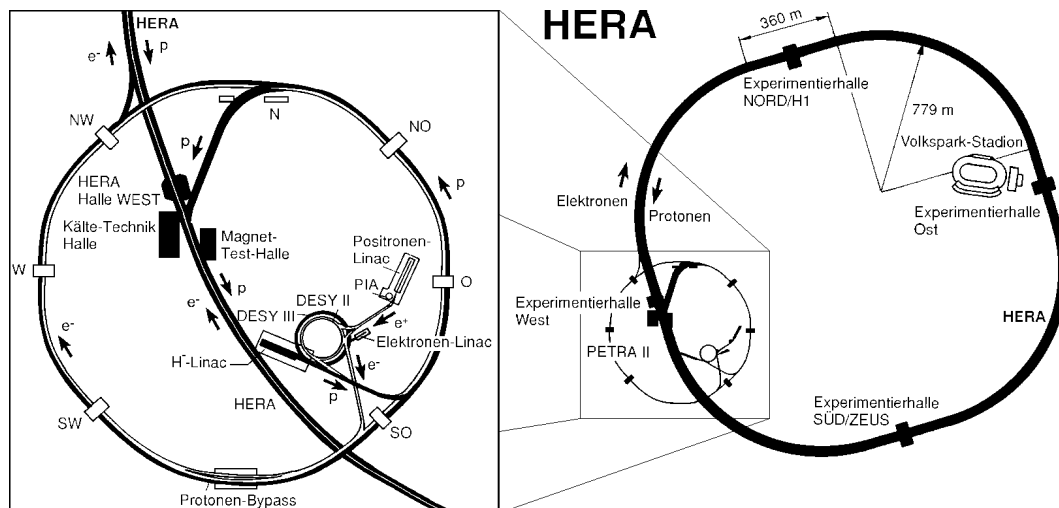


Figure 3.1: The HERA ring with associated experiments and injection facilities. The Linac injects particles into the DESY ring. DESY accelerates them and fills them into PETRA. The particles are further accelerated and injected into HERA.

The accelerator ring consists of 4 straight sections, connected by 90 degree arcs. An experiment is located on each of the straight sections. There are two general purpose experiments, ZEUS and H1, that collide the electron and proton beams together and two fixed target experiments. The HERMES experiment, located in the East Hall aims the electron beam onto a polarized gas target in order to investigate the nucleon spin structure. HERA-B, located in the West Hall uses the proton beam to

make collisions with a wire target in order to study CP violation in the $B^0\overline{B}^0$ system.

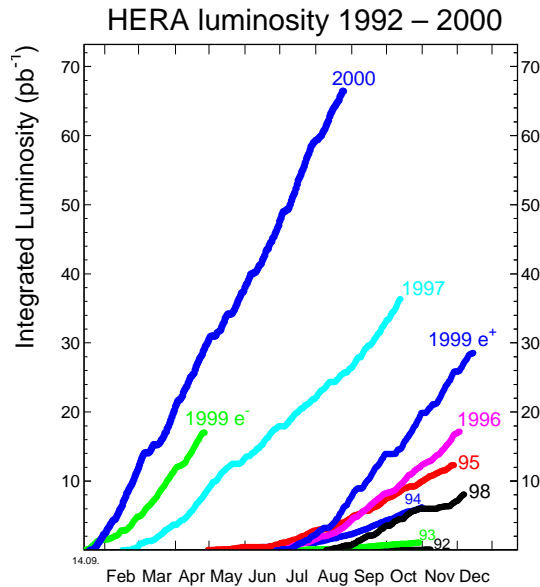


Figure 3.2: Luminosity delivered by HERA to the collider experiments for each year of running.

The luminosity delivered by HERA to the collider experiments improved steadily over the years of operation of Run I, as shown in Fig. 3.2. HERA was run with positrons all years except for a period in 1998 and 1999, in which the lepton beam was switched to electrons.

3.2 ZEUS Experiment

The ZEUS experiment is a collaborative effort of more than 450 physicists, students, technicians and staff from 52 institutes in 12 different countries. HERA being the first machine in which deep inelastic scattering could be performed at such high center-of-mass energy, ZEUS was originally envisioned as an experiment to make precise measurements of the proton structure, as well as for searches of rare and/or Beyond the Standard Model processes, such as the creation of leptoquarks.

The ZEUS detector is one of two general purpose detectors at HERA (H1 is the sister detector) designed to make a wide array of measurements. It is located in the South Hall of the HERA ring, has a size $12 \times 11 \times 20 \text{ m}^3$ and weighs 3600 tons. A schematic picture of the detector is given in Fig. 3.3. ZEUS uses a right-handed coordinate system with the nominal interaction point at the origin. The incoming protons move along the positive z -axis, the y -axis points upwards, away from

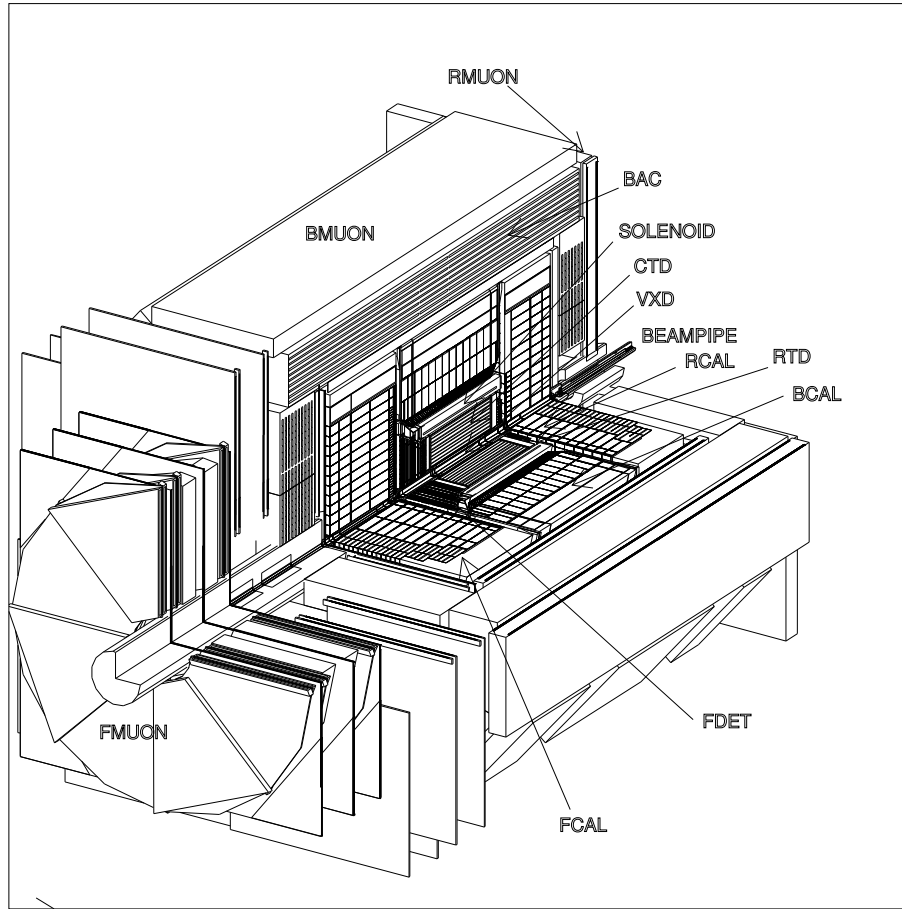


Figure 3.3: The ZEUS Detector

the earth, and the x-axis points toward the center of the ring. The polar angle, θ is defined with respect to the positive z-axis. Reference to the polar angle is often made with its relativistically invariant counterpart, η , defined as $\eta = -\ln \tan(\theta/2)$. After the interaction, the final state proton moves toward the forward part of the detector (positive z), while the final state electron approaches the rear (negative z). Because of the asymmetry of the incoming particles' energies, the forward direction of the detector is deeper than the rear in order to contain the hadronic final state.

There are many sub-detectors that make up the entire ZEUS detector, but all components can be classified as either tracking chambers which can measure particle trajectories and momenta, and calorimeters, which measure energies. ZEUS has a concentric design, as seen in Fig. 3.3, with the Central Tracking Detector (CTD) the most centrally located component. The vertex detector

(VXD) was removed from ZEUS in 1996 due to performance issues. The CTD operates inside a 1.4T magnetic field, which is created by a surrounding solenoid. The magnetic field induces the particle trajectories to bend, thus providing a method for extracting the particle's momentum. The CTD is supported in the forward and rear regions by the FTD and RTD (forward and rear tracking detectors).

The central calorimeter has a sandwich design of scintillator and absorber, and is constructed in such a way to make the response to hadronic particles equal to that of electromagnetic particles (compensating calorimeter). It has 3 sections: a forward calorimeter, a barrel calorimeter that encloses the CTD and a rear calorimeter. An external low-resolution calorimeter called the Backing Calorimeter (BAC) surrounds the main calorimeter in order to measure energy not absorbed by the main calorimeter. The BAC also serves as a return yoke for the magnetic flux of the solenoid. Outside the BAC are located the muon chambers. There are several other components, all of which are documented in the ZEUS Blue Book [21], but only those components which are used for the measurements described in this thesis will be explained in detail.

3.2.1 Uranium-Scintillator Calorimeter

The ZEUS calorimeter [22, 23, 24, 25] measures the energy of the particles that pass through it through a number of different processes. Particles with high enough energy (over about 1keV or so) interact with the material they are passing through via nuclear reactions, in/elastic scattering off nuclei, inelastic collisions with the atomic electrons of the material (ionization), bremsstrahlung and Cherenkov radiation. Which of these processes dominates depends on the type of particle and its energy. Hadronic particles typically lose their energies through nuclear processes and ionization; electrons through ionization and bremsstrahlung. At high energies, photons will pair produce, yielding an electron/positron pair that continues to lose energy through ionization.

An added complexity in measuring a particle's energy with the calorimeter comes from the fact that the signal response of hadrons and leptons is different. The response from hadronic particles is typically less than that from electromagnetic particles because they lose some of their energy in nuclear processes that don't result in a measureable signal. As a result, the hadronic calibration is much more difficult to make because the hadronic shower usually has an electromagnetic component

as well (e.g. $\pi^0 \rightarrow \gamma\gamma$). Since it is not known a priori what fraction of the shower is hadronic or electromagnetic, it is very difficult to get an accurate measure of the true energy that was deposited in the calorimeter. One can develop complex correction schemes to deal with this problem or make the calorimeter compensating. The ZEUS uranium-scintillator calorimeter achieves equal response to electrons and hadrons by using U^{238} as an absorber (one gets additional signal from fission of slow neutrons) and tuning the ratio of absorber to scintillator width (3.3 mm of absorber plate for every 2.6 mm of scintillator).

It is not usually possible to directly measure what kind of particle passed through the calorimeter. However, hadrons and electrons showers have different profiles in the calorimeter. Hadronic showers tend to extend deep into the calorimeter, while electromagnetic showers are shorter and narrower. To help differentiate between the two kinds of showers, the calorimeter was built with three longitudinal sections, EMC, HAC1 and HAC2. Showers originating from electrons are typically confined to the EMC section of the calorimeter, while hadronic showers extend into the HAC1 and HAC2 regions.

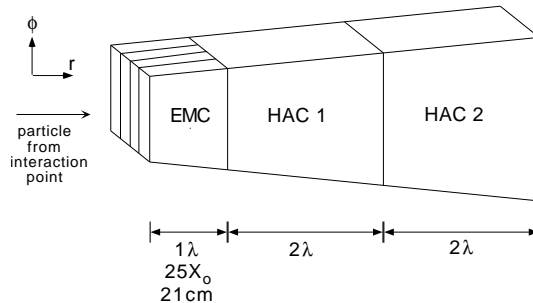


Figure 3.4: The structure of a BCAL tower. The electromagnetic section closest to the interaction point is deep enough to contain a typical 25 GeV electron shower. The HAC1 and HAC2 sections are longer in order to contain deeper hadronic showers.

In the ZEUS coordinate system, the FCAL sits at $222 < z < 452$ cm., the RCAL at $-309 < z < -148$ cm., and the BCAL covers the radial region between the RCAL and FCAL, $123 < r < 291$ cm. It has 99.7% solid angle coverage, the energy resolution for single hadrons is $\sigma(E)/E = 35\%/\sqrt{(E)}$, for single electrons $\sigma(E)/E = 18\%/\sqrt{(E)}$, and the absolute energy scale is known to within 1%.

A detailed description of how the calorimeter processes the signals it measures can be found

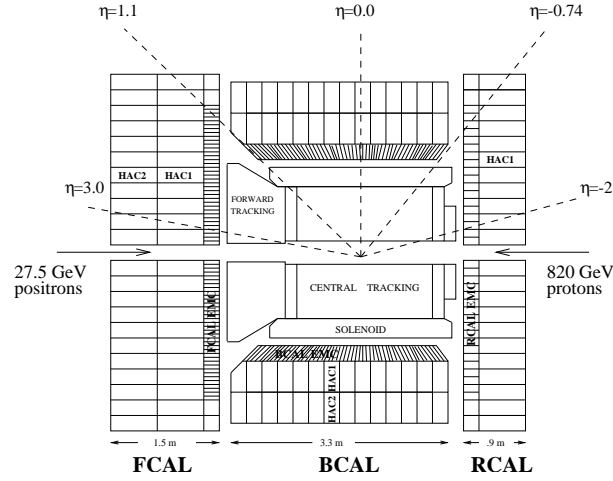


Figure 3.5: A schematic x-z view of the ZEUS Calorimeter

elsewhere [26]. In general, the shower produced by particles traversing the calorimeter creates UV light in the scintillator. This light is collected and passed to wavelength shifters and then on to photomultiplier tubes. The light’s wavelength is shifted in order to ensure optimal performance of the phototubes and light collection. The photomultiplier tubes convert the light signal to an electric signal which is then amplified and measured by read-out electronics.

3.2.2 Central Tracking Detector

The Central Tracking Detector (CTD) [27, 28, 29] is a 241 cm. cylindrical drift chamber surrounding the beampipe. It consists of 9 superlayers with 8 sense-wire layers in each superlayer. The odd-numbered superlayers have wires parallel to the beam axis (axial wires), while the even-numbered superlayer wires are set at a slight angle (stereo wires) in order to determine the z-coordinate of a hit. The CTD is important for determining the position of the event vertex, and has a vertex measurement resolution of 4mm in the z-direction. The CTD is also used to identify the scattered electron in DIS events. It is operated within a 1.4T magnetic field and its chambers hold a gas mixture of argon, carbon dioxide and ethane. When charged particles enter the CTD, they ionize this gas; the ions drift to the sense wires where they are collected. The trail of ions produced by the traversing particle create a series of hits which are then reconstructed as tracks. “Good tracks” are ones in which 3 superlayers can be used to reconstruct the trajectory of the particle.

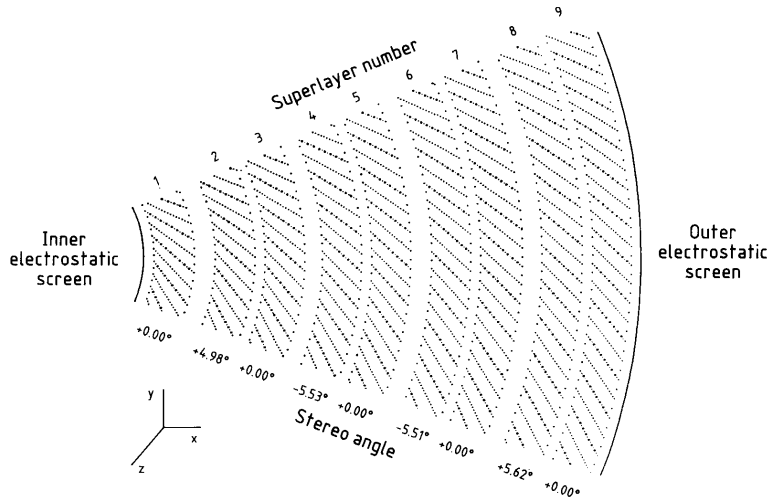


Figure 3.6: Diagram of one octant of the CTD

For triggering purposes, the three inner superlayers are equipped with a z-by-timing system which uses the axial wires to make a fast determination of the event vertex z-position [27]. This is used for background rejection at the Second Level Trigger (see Sec. 7.1.2).

3.2.3 Trigger System

Because of the 96 ns. crossing rate of the HERA accelerator, it is impossible to trigger on every bunch crossing. Indeed, that isn't even desirable since the background rate, assuming reasonable values for vacuum pressure and surrounding material upstream of the proton beam, is on the order of 50 kHz, while the rate of ep physics events, assuming a luminosity of $2 \cdot 10^{-5} pb^{-1}s^{-1}$, is less than 500 Hz. The main sources of background are proton beam-gas interactions, proton beam halo events and cosmic induced events. In order to handle the speed at which the events are processed through the ZEUS data acquisition system, a three-tiered trigger has been built, as seen in Fig. 3.7.

At the first level, the trigger is designed to make a fast decision on whether the event is an ep physics event or not. Most detector components have dedicated hardware to make a trigger decision, but the ones relied on most heavily are the Calorimeter First Level Trigger (CFLT) [30] and the CTD First Level Trigger (CTD FLT) [31]. The CFLT takes 5% of the Calorimeter signal from every PMT, shapes the analog signal, digitizes the signal and computes global calorimeter sums such as total transverse energy and missing p_T ; it also performs some primitive electron finding. Taken in

combination with tracking triggers, the Global First Level Trigger (GFLT) can reduce the rate of events down to 500 Hz for processing by the second level. The First Level Trigger makes a decision to keep or discard each bunch crossing by storing all data in a pipeline for $\sim 5\mu s$. while the first level trigger calculations are being performed and the first level trigger signal is propagating back to the component. It is a completely deadtimeless process, accepting data from a new crossing every 96 ns, and issuing an accept or reject $4.4\mu s$. after the event occurred.

The Second Level Trigger (SLT) is software-based and data from other detector components are used to make a more detailed selection. The calorimeter SLT computes global timing, a more accurate transverse energy, and $E - p_z$. The tracking SLT uses the z-by-timing system to make an estimate of the event vertex. The SLT reduces the event rate further to approximately 100 Hz.

If the event is accepted by the GFLT, all detector components send their data to the event builder for reconstruction. The event is then passed to the Third Level Trigger, which performs a variety of calculations, very similar to offline data analysis in order to make a final decision on whether the events are rejected or kept and written to tape.

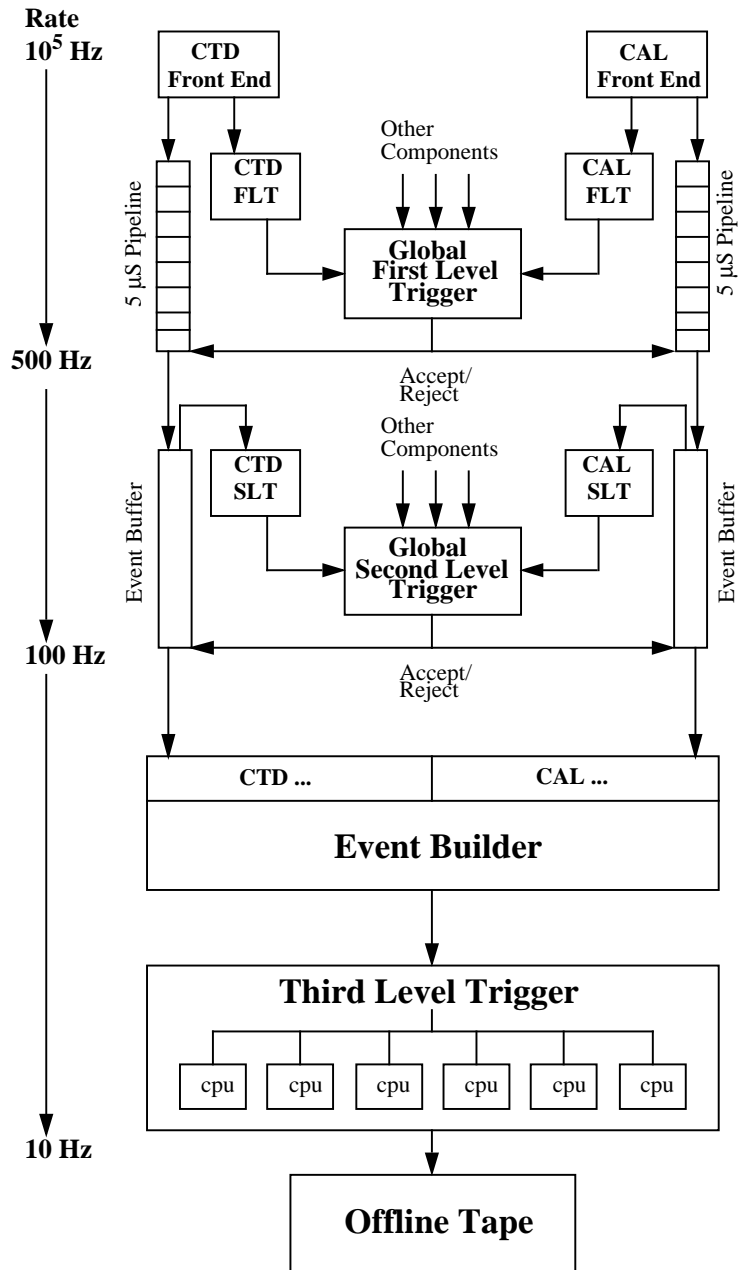


Figure 3.7: ZEUS Trigger and Data Acquisition System

3.2.4 Luminosity Measurement

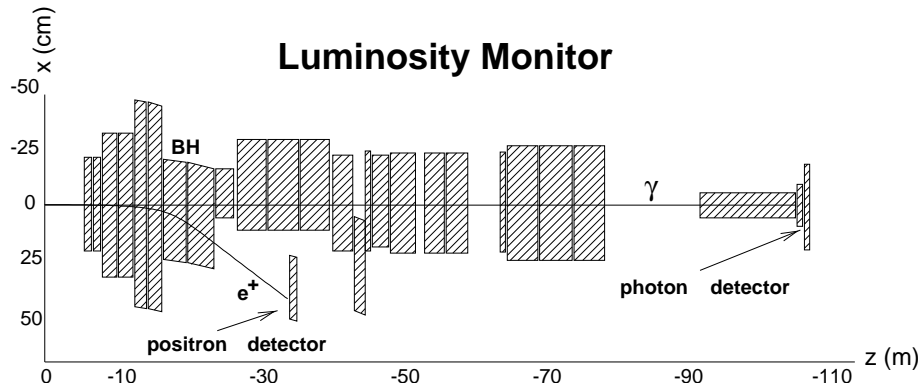


Figure 3.8: The ZEUS Luminosity Monitor System

In order to measure any cross section at ZEUS, one must know the ep interaction luminosity. The luminosity measurement is used to normalize the event rate measured as per the formula

$$\sigma = N_{events}/\mathcal{L}. \quad (3.1)$$

One can get a very precise measure of the luminosity by counting the rate at which a well-understood process takes place and inverting Eqn. 3.1 to extract the luminosity \mathcal{L} . At HERA, the ep-bremsstrahlung process

$$e + p \rightarrow e' + \gamma + p \quad (3.2)$$

is used for the luminosity measurement. The cross section for this process is given by the Bethe-Heitler Equation and is known to very high accuracy. The detector system used for measuring this process is shown in Fig. 3.8.

The final state electron and photon emerge from the interaction point through the rear calorimeter. Downstream, a set of dipole magnets bend the electron, selecting out shallow-angle electrons with energies $0.35E_e < E_{e'} < 0.65E_e$. An electron calorimeter measures the electron's energy with 70% acceptance for electron energies in the previously stated range. The photon continues through the magnetized region undeflected and is measured by a lead-scintillator calorimeter, called the Lumi-gamma detector [32], 107 m. from the nominal interaction point. A carbon filter is placed

in front of the calorimeter to shield it from synchrotron photons. A coincidence of a photon and electron in their respective calorimeters constitutes the signal for the luminosity measurement.

3.2.5 Detectors for Correcting Electron Measurements

Measuring the scattered DIS electron accurately is one of the most fundamental and necessary pieces of any NC DIS analysis. Considerable efforts are taken to get an accurate measure of the electron's position and energy using detectors in addition to the main calorimeter and tracking detector. The Hadron-Electron Separator (HES) is used to make a precise position measurement, while the pre-shower detectors Presampler (PRES) [33] and Small Rear Tracking Detector (SRTD) [34] are used to correct for showering in front of the calorimeter.

3.2.5.1 Hadron-Electron Separator

The HES [35] is an array of 3x3 cm. silicon diodes located at a depth of three radiation lengths into the EMC section of the Forward and Rear calorimeters. It was originally designed to distinguish between electromagnetic and hadronic showers. The $3X_0$ depth was chosen to coincide with the peak width of a 27.5 GeV electron shower, but, due to an underestimation of the dead material effect, it is located deeper than the true peak, degrading its ability to distinguish the shower types. However, due to its much finer granularity than the main calorimeter and fixed depth, its measurement is used to correct the position of the electron measured by the main calorimeter.

3.2.5.2 Preshower Detectors - Presampler and SRTD

As electrons pass through inactive material in the detector (material in which the energy created through interaction is not captured), energy from the showering is lost and results in a reduced calorimeter measurement of the electron. In order to correct for this loss, two calorimeters were placed in front of the RCAL to measure the number of minimum ionizing particles (MIPS) incident on the face of the RCAL. The layout of both the Rear Presampler and the SRTD relative to the RCAL are shown in Fig. 3.9. The number of MIPS is the number of particles created in the shower and is proportional to the energy lost in the shower. The energy measured by the calorimeter can be scaled up by a factor proportional to the number of MIPS measured in either the SRTD or Presampler (but not both).

The Rear Presampler consists of 20x20 cm. scintillator tiles placed directly in front of almost the entire RCAL face. The SRTD consists of 4 orthogonal quadrants oriented around the RCAL beampipe. The SRTD is particularly useful for correcting low- Q^2 DIS electrons, where the electron scatters at shallow angles. Each quadrant has two planes of 1.0 cm. scintillator strips, one plane with strips oriented along the x-axis, the other with strips oriented along the y-axis. This checkered pattern allows a position measurement to be made as well.

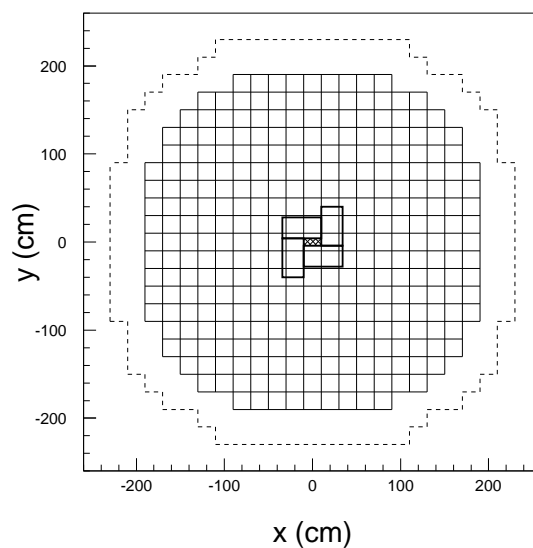


Figure 3.9: The front face of the RCAL, viewed from the interaction point. The dotted line represents the RCAL boundary, the checkered region the area of the RCAL covered by the Rear Presampler, and the bold sections in the middle represent the SRTD coverage.

Chapter 4

Event Generators and Detector Simulation

4.1 The Monte Carlo Approach

This analysis relies on Monte Carlo techniques to unfold the measured cross sections in selected kinematic regions of interest, to determine the event and jet finding efficiencies, to check the accuracy of event and jet kinematic reconstruction and to generate correction factors needed to compare the measured cross sections to the NLO calculations discussed in the next chapter. Monte Carlos simulate the data of interest (in our case, neutral current deep-inelastic electron-proton scattering) by randomly generating events according to the rules of QCD and phenomenological models. Specifically, all the possible Born level Feynman diagrams for the hard interaction between an electron and a proton are generated according to their probabilities, where the probabilities are taken from the integral of the relevant Born level matrix element. In the Monte Carlos used for this analysis, there are three event types of interest, the Quark-Parton Model event, the QCD-Compton event and the Boson-Gluon Fusion event. The parameters that define the kinematics and types of particles participating in a given event are assigned according to a random sampling of known probability distributions. In this way, the kinematic behavior of the accumulated events is consistent with that of the probability distribution. Once a reasonable level of statistical precision is achieved in the event generation process, the MC events can be compared to real data.

There are four stages of evolution a MC event must pass through before it is used for comparison with real data. The hard subprocess is calculated according to the Feynman rules, the final state partons emitted from the hard scatter produce a QCD shower, the proton remnant evolves according

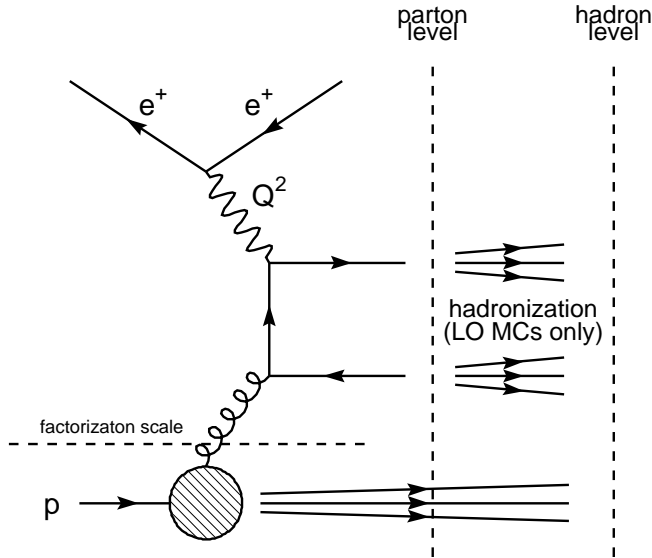


Figure 4.1: Diagram showing the delineation between the hard subprocess, parton showering and hadronization phase of a Monte Carlo Event. The factorization scale is the scale at which the parton density functions are evaluated.

to phenomenological models, and particles resulting from the parton shower are grouped into stable hadrons. The stages of development are shown in Fig. 4.1 for a Boson-Gluon Fusion event. For the purposes of this analysis, the “parton level” will be considered to be after the parton showering described below, and the “hadron level” is defined at the stage where all particles present are stable hadrons. The output of the Monte Carlo simulation is a list of all particles that participated in the event during one or more of its phases, from the initial colliding particles and exchange boson, to the final hadrons. The list of hadrons is then propagated through a GEANT-based¹ detector simulation which produces detector signal which are passed through the same reconstruction as the data.

4.2 Parton Density Functions (PDF's)

As discussed in Sec. 2.4.3, the amplitude for an ep scattering process can be factorized into a calculable matrix element piece and a non-perturbative parton density function that gives the quark and gluon content of the proton at a particular value of x and Q^2 . These PDF's are an input to the

¹GEANT is a simulation program which models the passage of particles through matter. Various geometries and interaction materials are included in the program to simulate the detector components.

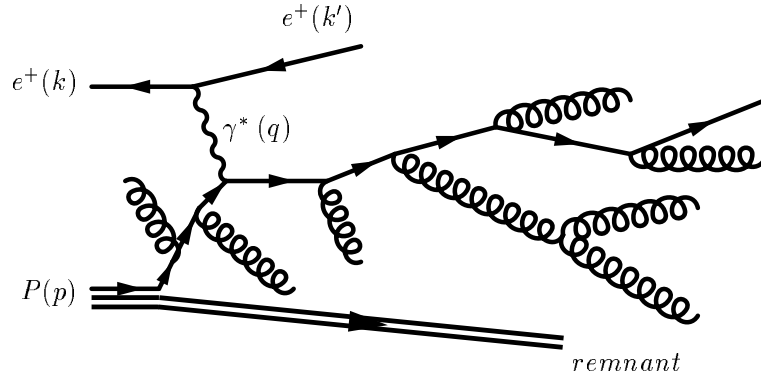


Figure 4.2: Matrix-Element/Parton Shower (MEPS) approach to parton showers as implemented in LEPTO. The parton cascade is treated as successive branchings of partons with decreasing virtuality.

Monte Carlo simulations. They are generated from fits to fixed target and inclusive ep deep inelastic scattering data, as well as Drell-Yan production, W-asymmetry and inclusive jets in $p\bar{p}$ and prompt photon production in pN scattering [36]. The fits are parameterized by DGLAP evolution, using various schemes for renormalization. In this analysis, the CTEQ4M PDF is used as an input to the Monte Carlo programs.

4.3 Parton Shower Evolution

The parton shower phenomenology is not only important as a connection between the analytically calculable hard subprocess and the observable hadrons, but it also as a model (albeit not using a strict perturbative QCD approach) for higher-order QCD effects, which are very difficult and time-consuming to calculate. These higher order effects are particularly important in describing multi-jet events which arise from multiple parton emissions. At the time of this thesis, the highest-order complete matrix element calculations available are $\mathcal{O}(\alpha_s^2)$, one order above the LO matrix elements used by the Monte Carlos.

4.3.1 Matrix-Element and Parton Shower Models (MEPS)

In Deep Inelastic Scattering, QCD radiation can occur both before and after the hard interaction, as shown in Fig. 4.2. In the DIS process, a parton close to or on mass-shell in the proton can initiate a parton cascade where in each branching one parton becomes increasingly off-shell with

a space-like virtuality and the other is on-shell or has a time-like virtuality. From this space-like shower, a space-like quark is generated which participates in the hard interaction with the exchange boson. The interaction with the boson turns the outgoing quark into one with either a time-like virtuality or one that is on-shell. In the former case, the shower continues, which each branching producing decreasingly off-shell masses until all the partons are on-shell.

In the MEPS scheme [37], these two showers (before and after the hard interaction) are treated differently, although they are both based on splitting functions as described by the DGLAP equations (see Sec. 2.4.3). The final state radiation is analogous to parton radiation in $e^+e^- \rightarrow q\bar{q}$, which has been tested extensively against data. The evolution is based on the Sudakov form factor, which expresses the probability that a parton does not branch between some initial maximum virtuality and some minimum value. The branching process is iterated until all parton virtualities are below some cutoff, around 1 GeV^2 [38].

The initial state radiation is reconstructed from the hard interaction backwards, with decreasing virtuality at each splitting, to the on-shell parton from the incoming nucleon. This is a more complicated process since the parton density function must be taken into account, which reduces the amount of radiation. The initial and final state radiation are combined with the matrix element calculation, but interference terms between initial and final state radiation are not included. The parton shower approach is, as a result, gauge dependent. This approach also does not treat QCD emissions from the proton remnant.

4.3.2 Color Dipole Model

In the Color Dipole [39, 40, 41, 42] prescription, instead of modeling an initial and final state radiation process independently, all radiation is assumed to occur between the color dipole formed between the struck quark and the proton remnant. The radiation process can be thought of as modified e^+e^- scattering, with one of the quarks from the hard interaction substituted with the proton remnant (see Fig. 4.3). In the simplified e^+e^- scenario, a color dipole forms between the $q\bar{q}$ from the hard interaction, which induces a gluon emission. At “second order”, softer gluon emission can be treated as radiation from two independent dipoles, one between the quark and gluon, the other between the gluon and antiquark. The emission probability is given, as in MEPS, by the Sudakov

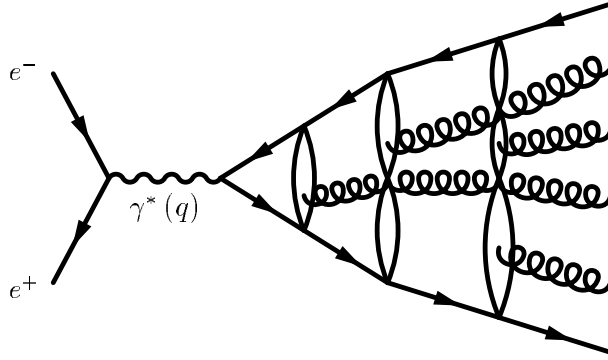


Figure 4.3: Color Dipole Model approach to parton showers as implemented in ARIADNE. The parton cascade is treated as a formation of color dipoles, each of which may produce one or more softer emissions.

form factor. This approximation would be adequate if in DIS, as with e^+e^- , the initial color dipole had point-like constituents. The proton remnant, however, is an extended object, and modifications are made to allow only a fraction of the proton remnant’s light-cone momentum to take part in an emission, thus reducing the available phase space as compared with e^+e^- . As each dipole radiates independently, no ordering is induced in the transverse energy of the partons.

Because BGF processes do not occur in e^+e^- scattering, they are not explicitly included in this model, and a matching procedure needs to be included in the first emission to take into account this matrix-element for the DIS case. In this procedure, the initial dipole between the struck quark and the hadron remnant can either emit a gluon according to the $\mathcal{O}(\alpha_s)$ matrix element (as usual) or “emit” the antipartner of the struck quark according to the BGF matrix element. In the latter case, two color dipoles are created which continue to radiate independently according to the model. These two dipoles are meant to mimic the color connection between each of the final state quarks with the proton remnant of a BGF process.

4.4 Hadronisation Models

At the end of the parton showering process, we are left with groups of colored partons which are not observable as free particles. A further phenomenological process has to be introduced to group these partons into color-singlet bound states of confined quarks and gluons called hadrons. Many hadronization models exist, but two are commonly used by the MC generators for DIS. The

Lund String Model is used by the programs LEPTO [38] and ARIADNE [43, 44], while the Cluster Model is used by HERWIG.

4.4.1 Lund String Model

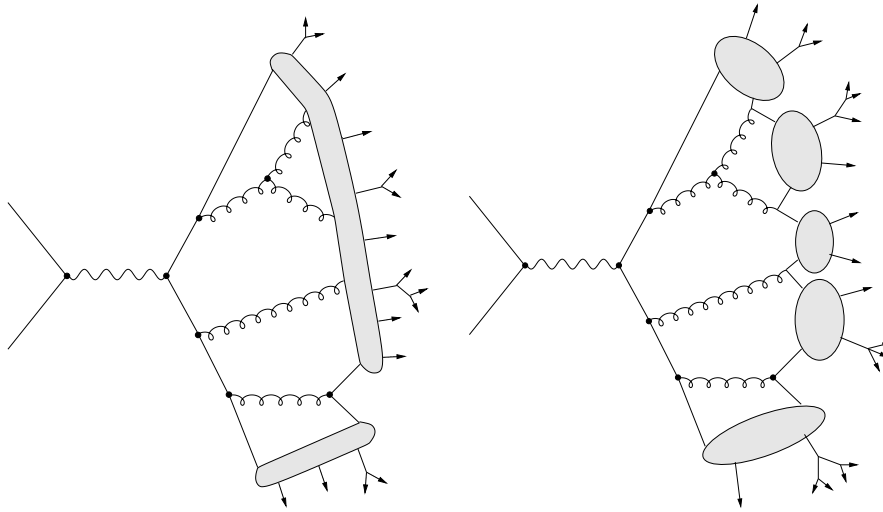


Figure 4.4: Hadronization scheme according to the Lund String Model (left) and Cluster Fragmentation Model (right). The strings and clusters are represented in the shaded regions of each drawing, and the outgoing arrows represent hadrons [18].

In the Lund String Model [45], the hadronization process occurs through the formation of color strings and the fragmentation of those strings into hadrons. A given pair of quarks $q\bar{q}$ move away from each other effectively stretching out the “string” that represents the force of the color connection. The amount of energy stored in the string per unit length is given by hadron spectroscopy, and is typically on the order of $\sim 1 \text{ GeV}/fm$. The farther away the two partons move from each other, the greater potential energy stored in the string, until the string breaks due to the creation of a new $q\bar{q}$ pair in the color field. The two strings formed in the process continue to evolve independently, and the process continues until the invariant mass of a given string is below a threshold value. Hadrons are formed from the colorless, stable objects spanned by the string below the mass threshold. The string structure gets more complicated as gluons and sea quarks are introduced to the model, those details can be found in [45].

The Lund String Model is an infrared safe one, due to the smooth transition between events

with soft, collinear partons and those without. Such emissions in the parton shower phase can change the shape of the observable objects (hadrons or jets), but not the presence of them. The Lund String Model is used by both the LEPTO and ARIADNE MC generators.

4.4.2 Cluster Fragmentation

The cluster model begins by splitting gluons non-perturbatively into quark-antiquark or diquark-antidiquark pairs. Neighboring quarks and antiquarks are then grouped into color-singlet objects or clusters. These clusters are then split into hadrons, according to their mass. A cluster too light to form two hadrons becomes the lightest hadron of the appropriate flavor, by shifting its mass by exchanging momentum with neighboring clusters. The flavor of the hadrons is determined by the density of states available.

The HERWIG MC generator uses Cluster Fragmentation. The strength of this simulation is its emphasis on the perturbatively calculable parts of the program, minimizing the number of model dependencies used to generate predictions. It assumes any observable quantity will be dominated by the perturbative part of the calculation. It therefore has very few tunable parameters and very high predictive power. However, it gives a poorer description of the hadronic final state in DIS, so isn't the preferred Monte Carlo for modeling the detector effects.

4.5 QED Effects

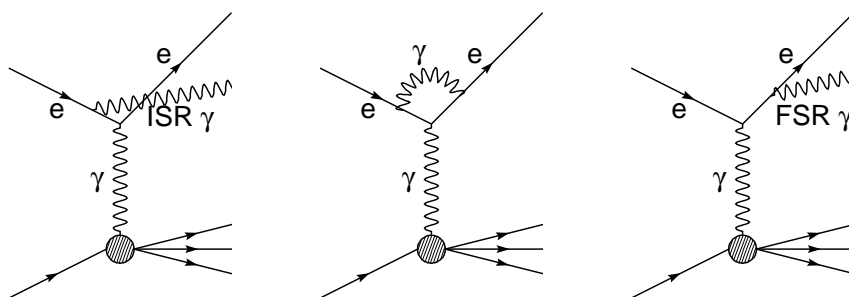


Figure 4.5: Diagrams illustrating QED radiation in the initial state, as a virtual loop, and in the final state.

The standalone MC generators by default do not include the effects of QED radiation. However, these effects are significant and present in the data. Fig. 4.5 shows the first order photon

radiation diagrams. In order to take these effects into account, the MC programs are interfaced with HERACLES [46] using the DJANGO [47, 48] program. HERACLES modifies the generated cross sections and includes the photon in the event where appropriate.

4.6 Detector Simulation

Once the full event is simulated according to the phases described thus far, a table called FMCKIN is generated with a list of particles which participated at some stage in the event. The final state hadrons in the list are then sent through a shower simulation in the detector using the GEANT program. The detector quantities are then reconstructed just as in real data. The results are also passed through the trigger simulation, ZGANA. At this point, a “detector level” comparison between data and MC events can be made, which is shown for this analysis in Chapter 8. The quality of this comparison affects how accurately the data can be unfolded to the hadron level. At the hadron level, the cross sections are seen as the true values, independent of any detector bias.

Chapter 5

NLO QCD Predictions

There exist another class of programs, also implemented as event generators, which calculate partonic cross sections of DIS processes up to $\mathcal{O}(\alpha_s^2)$, according to the mechanisms of perturbative QCD, the so-called NLO Calculations. They are, therefore, free of the phenomenological, QCD-inspired approximations that are present in the MC Models discussed in the previous chapter. They are fixed-order calculations, that is they predict a cross section at second order in α_s , which involve summing over Feynman diagrams of the Born process, diagrams with one additional gluon emission, the splitting of a gluon into a $q\bar{q}$ pair and diagrams with a virtual gluon loop.

As was introduced in Sec. 2.4.3, the NC DIS cross section can be factorized into a partonic cross section and a non-perturbative parameterization of the proton PDF. The partonic cross section, $d\hat{\sigma}$, can be written as a sum of the Born cross section and the contribution to the cross section due to $\mathcal{O}(\alpha_s)$ corrections.

$$d\hat{\sigma} = d\hat{\sigma}^{LO} + d\hat{\sigma}^{NLO} \quad (5.1)$$

where

$$d\hat{\sigma}^{LO} = \int_m d\hat{\sigma}^{Born} = \int_m d\Phi^m |\mathcal{M}_m|^2 F_J^m \quad (5.2)$$

is the familiar Born-level cross section. m represents the number of partons in the final state, $d\Phi$ denotes the phase space over which the final-state partons are integrated over, and \mathcal{M}_m are the tree-level QCD matrix elements. F is the physical observable one would like to compute, e.g. the functional representation of the jet algorithm in terms of the parton 4-momenta. It is important that the function F be infrared safe. That is, the removal of soft partons or replacement of the

four-momentum of two collinear particles by their sum does not change F .

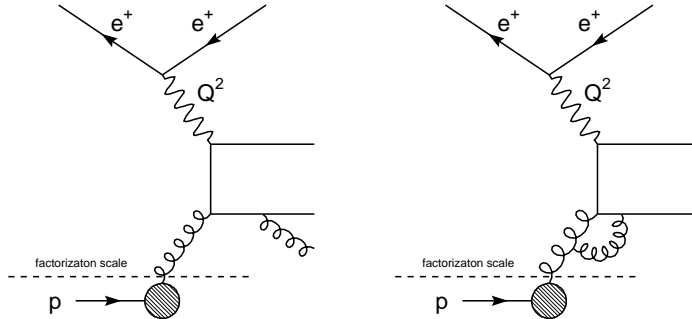


Figure 5.1: Boson Gluon Fusion Diagrams with real (left) and virtual (right) gluon emission.

To compute the NLO contribution to the full cross section, the contributions involving single gluon exchange need to be accounted for. This gluon exchange is manifested either as a hard or soft real emission, or as a virtual gluon loop, as shown in Fig. 5.1. The contributions to the NLO cross section from real and virtual emissions need to be treated separately, and an additional contribution from a collinear-subtraction counterterm needs to be introduced due to the presence of the proton and its associated renormalized parton density function.

$$d\hat{\sigma}^{NLO} = \int_{m+1} d\hat{\sigma}^{real} + \int_m d\hat{\sigma}^{virtual} + \int_m d\hat{\sigma}^{counterterm} \quad (5.3)$$

The ultraviolet divergencies appearing in the integral over the virtual contributions to the cross section have been eliminated through renormalization. The real ($m+1$ parton) and virtual (m partons) cross sections take the same structure as the Born-level cross section given in Eqn. 5.2. In the calculation of these real and virtual contribution to the NLO cross section, infrared divergencies appear when the gluon emission becomes very soft or collinear with a hard final-state parton. In the case of e^+e^- scattering (where there is no need for the counterterm), the divergencies from the real and virtual emissions cancel exactly, according to the Kinoshita-Lee-Nauenberg [49, 50] theorem. However, due to the presence of a proton in the initial state in deep inelastic scattering, additional singularities can appear from initial-state parton emission. The counterterm is introduced to provide full cancellation of all soft and collinear singularities. The form the counterterm takes is dependent on

what factorization scheme is used in the evaluation of the parton density function, and it is explicitly dependent on the factorization scale.

5.1 DISENT Program

Recently, a number of programs have been written to implement the calculation of the NLO cross section for jet observables in a generator format. The program used in this analysis is DISENT [51], although the results obtained for this analysis were checked using the program DISASTER [52], which yielded agreement at the 1-2% level. In order to calculate the contributions to the NLO cross section from real and virtual gluon emissions, these programs must find a method for dealing with infrared divergencies that arise from the integration of the two terms on the right side of Eqn. 5.3. Two common methods employ the phase-space splicing and subtraction techniques. The DISENT and DISASTER programs use the subtraction method.

5.1.1 Subtraction Method for Singularity Cancellations

The subtraction method adds and subtracts a local counterterm, $d\hat{\sigma}^{local}$, whose role is to make the real and virtual cross sections separately integrable. This counterterm is included in the full NLO cross section as follows:

$$d\hat{\sigma}^{NLO} = \int_{m+1} [d\hat{\sigma}^{real} - d\hat{\sigma}^{local}] + \int_m d\hat{\sigma}^{virtual} + \int_{m+1} d\hat{\sigma}^{local} + \int_m d\hat{\sigma}^{counterterm} \quad (5.4)$$

where $d\hat{\sigma}^{local}$ is a proper approximation of $d\hat{\sigma}^{real}$ such as to have the same singular behavior as $d\hat{\sigma}^{real}$ itself. This allows the first integral on the right side of Eqn. 5.4 to be integrated numerically in four dimensions. Additionally, $d\hat{\sigma}^{local}$ must be analytically integrable over the one-parton subspace leading to the soft and collinear divergencies. The poles associated with this integration can then be combined with those in the virtual term and counterterm, yielding a finite sum for the three remaining terms in Eqn. 5.4. Combining all pieces one can then determine a result for the NLO partonic cross section which can then be easily implemented in a Monte Carlo program which generates appropriately weighted partonic events with m and $m+1$ final state partons.

5.1.2 Implementation

To generate the full cross section for a given process, the LO and NLO contributions in Eqn. 5.1 are calculated separately. The LO piece is constructed by considering each m-parton event that is generated within the phase space $d\Phi^m$. For each event, a weight is assigned according to $|\mathcal{M}_m|^2$. The event is then analyzed by a user routine which selects events that fall inside the phase space function F_J^m and stored. The NLO contribution to the cross section is obtained by adding events represented by the two contributions in Eqn 5.4, with m-parton and (m+1)-parton final states. The events are weighted by a modified matrix element that takes the integration including the counterterms into account [51]. It should be noted that some events can have negative weights which, if the phase space function F_J^m is chosen properly, should cancel with positive weighted events, reflecting the exact cancellation between real and virtual gluon emissions.

5.2 Theoretical Predictions and Uncertainties

In this analysis, the partons generated by DISENT are fed into the k_T -cluster algorithm for jet finding (see Sec. 6.2). The CTEQ6 [36] parameterization of the parton density function is used for the incoming proton. The selection cuts on the jets are made in the same way as they are on the Monte Carlo and data. In order to generate the theoretical prediction that is comparable to the data, a number of other effects need to be taken into account.

5.2.1 Renormalization Scale Dependence and Uncertainty

As was described in Sec. 2.3, a renormalization scale needs to be introduced to eliminate ultraviolet divergencies in the NLO calculation. It is the scale at which the running coupling constant $\alpha_s(\mu_R^2)$ is evaluated. The renormalization scale chosen for the cross sections presented in this analysis is $\mu_R = \sqrt{Q^2}$, the scale which characterizes the hard pQCD process.

The uncertainty associated with the choice of renormalization scale is the largest contribution to the theoretical error for jet analyses in DIS. The error results from the fact that the NLO calculation is limited to second order in the perturbative expansion of α_s . By imposing a cutoff, a dependence of the NLO cross sections on the renormalization scale is introduced. The uncertainty on that dependence is estimated by varying the renormalization scale choice up and down by a factor of two,

and measuring the change of the resulting cross section. The choice of scaling by two is a convention within HERA analyses. The magnitude of the variation in the cross section gives an idea of how large the contributions from higher order processes are. Depending on the kinematic region, the renormalization scale uncertainty for inclusive jet cross sections in the forward region of the detector are between 5% and 50% as shown in the cross section measurements of Chapter 9.

5.2.2 Parton Density Functions and Uncertainties

The parton density functions that are convoluted with the partonic final state to produce DIS predictions by DISENT are generated by fits to data using DGLAP parameterization. In the CTEQ6 extraction of the PDF's [36], the fundamental parameters of QCD, the strong coupling constant α_s and the quark masses, are taken as input to the fit. A starting scale, Q_0 , for the fit is chosen and the input data measurements are then fitted according to NLO DGLAP evolution using the functional form:

$$xf(x, Q_0) = A_0 x^{A_1} (1-x)^{A_2} e^{A_3 x} (1 + e^{A_4 x})^{A_5} \quad (5.5)$$

A χ^2 minimization is performed and the PDF's are extracted from the parameters of the fit.

Uncertainties are introduced from the experimental data used to extract the PDF, from theoretical assumptions and uncertainties, and from approximations made in the fit procedure. To estimate the full uncertainty on the PDF's, the CTEQ group have formulated two methods using Hessian and Lagrange techniques, to characterize the behavior of the χ^2 function in the neighborhood of the global minimum in a reliable way. All input parameters, e.g. the quark masses, are varied and the resulting PDF's are extracted using these techniques, resulting in $2N_P + 1$ PDF sets, where N_P is the number of input parameters. The total uncertainty is then computed for any physical observable from the variation in these sets. It was found for the cross sections measured in this analysis that the uncertainty arising from the PDF was much smaller than the renormalization scale uncertainty, and never larger than 5%.

5.3 Hadronisation Corrections

The DISENT program produces parton level cross sections, where the parton level is illustrated schematically in Fig. 4.1. The hadronization phase that the final state partons must undergo is

not modelled by the program. The only possibility to quantify the change in the jet rate due to hadronization is to use the LO Monte Carlo models. To that end, the jet finding is performed on hadrons and partons from the Monte Carlo events, and a correction factor is calculated according to the ratio of hadron level cross section and parton level cross section. This ratio is then applied to the partonic jet rates generated by DISENT in order to have a next-to-leading order “hadron level” prediction of the cross section. The hadronization uncertainty is estimated by difference in the correction factor between two different Monte Carlos. Shown in Fig. 5.2 are the magnitude and uncertainty in the hadronization corrections as computed with Lepto and Ariadne for single inclusive cross sections in η_{jet} , $E_{T,jet}$, Q^2 and x_{Bj} . The correction factor is generally smaller than 20% and the largest uncertainty in the hadronization correction is $\sim 7\%$. The hadronization corrections applied to all NLO parton level predictions are shown alongside their corresponding cross section measurements in Chapter 9.

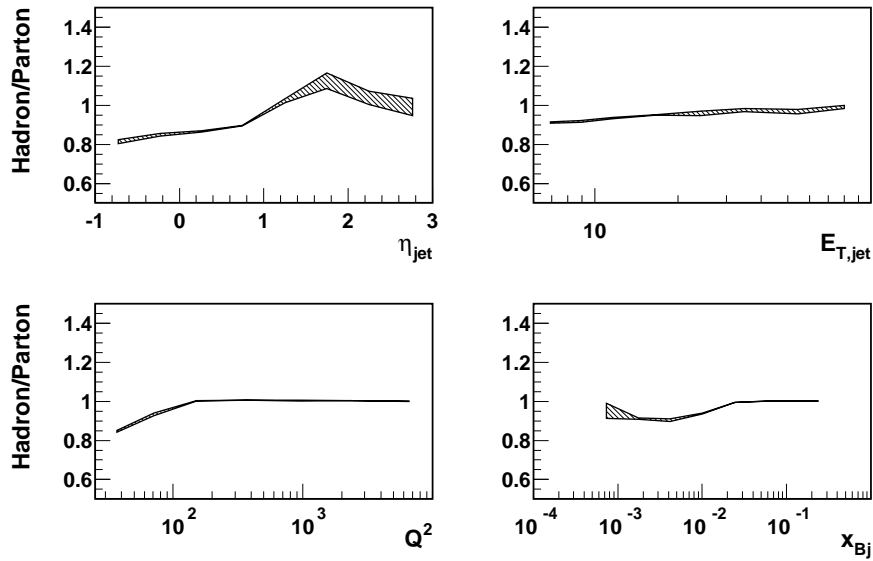


Figure 5.2: Hadronization correction uncertainty for η_{jet} , $E_{T,jet}$, Q^2 and x_{Bj} for inclusive jet cross sections. The shaded band is the difference between the hadronization correction computed with Ariadne and Lepto.

Chapter 6

Jet Physics in DIS at HERA

The predictions outlined in the previous chapters need to be compared to experimentally observable quantities. The final state partons in the calculation of any Feynman diagram are not observable particles, due to color confinement in QCD. These partons undergo showering and hadronization as was described in Chapter 3. The observable quantities are groups of hadrons that originate from partons emitted in the hard interaction. The comparison of data to theoretical predictions requires tools to relate hard partons to groups of hadrons and the energy distributions observed in the detector for each event. Jet algorithms have been developed to do just that. They are tools for grouping clusters of energy into objects called jets. The most reliable jet algorithms are ones that can be applied to the final state partons, hadrons, and detector cells in the same way. In other words, jet finding on an event's partons, hadrons and detector cells produces jets of comparable energy and position. In a manner similar to the infrared divergencies discussed in Chapter 4, jet algorithms face the problem of infrared safety. Emission of soft or collinear particles can change the jet's energy when an infrared-unsafe algorithm is run on partons or hadrons.

6.1 Reconstruction of the Kinematic Variables

Kinematic reconstruction is necessary to identify the type of event that took place. The DIS variables described in Sec 2.4 apply exactly to the experimental quantities observed. Reconstructing those variables as precisely as possible is another experimental challenge. There are 7 independent components that characterize ep interactions when the incoming beam energies are known. These are the 3-momentum of the scattered lepton, $p_{x,el}$, $p_{y,el}$ and $p_{z,el}$, and the four-momentum of the

remaining particles which make up the hadronic system: $p_{x,had}, p_{y,had}, p_{z,had}$ and E_{had} . Certain constraints on the system reduce the number of independent variables to 2. Four constraints are derived from the fixed center-of-mass energy, and conservation of energy and momentum in the three spatial directions. The final constraint comes from the azimuthal symmetry of the interaction. The incoming beams lie on one axis, and there is no azimuthal dependence on rotations about that axis. The quantities measured in the detector are the final state lepton's energy and polar angle and the energy and polar angle of the hadronic final state. Because only 2 of these variables are needed to fully constrain the kinematics, we have a choice of which variables to use. Three common choices are detailed in the following sections.

6.1.1 Double-Angle Method

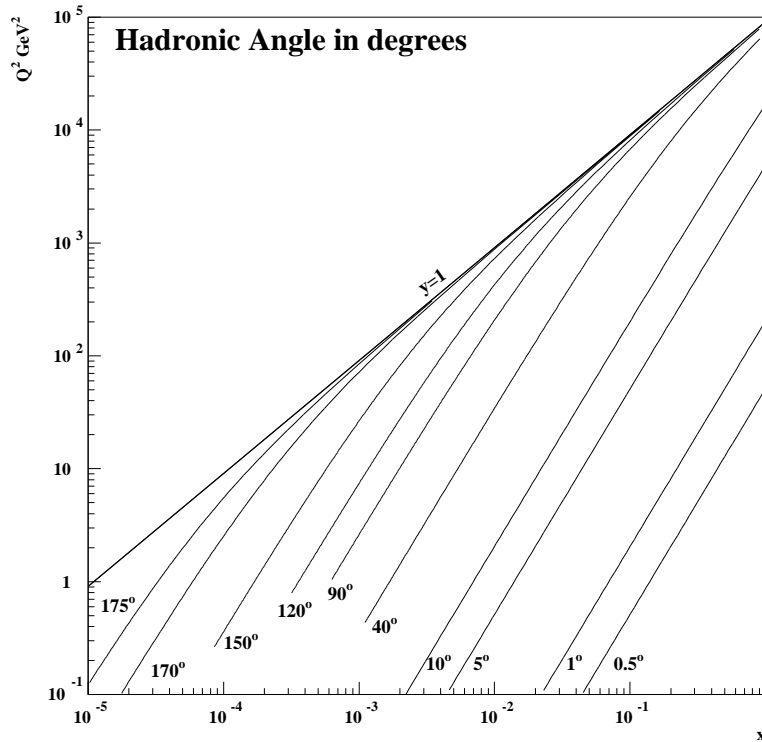


Figure 6.1: Lines of constant hadronic angle in $x - Q^2$ plane. The isolines correspond roughly to lines of constant y .

The double-angle method [53] uses the polar angle of the electron and the angle of the hadronic system. For quark-parton model events, the latter is aligned with the polar angle of the scattered

quark. Because the hadronic system is a diffuse object, its angle cannot be measured directly. However, using the hadronic $E - p_z$ and p_T , one can reconstruct the angle of the hadronic system, γ_h . Assuming that the $E - p_z$ and p_T of the hadronic system are directly resolved from the 4-momenta of the struck parton, one can write the geometric relations:

$$\begin{aligned}(E - p_z)_{hadronic} &= E_q(1 - \cos\gamma_h); \\ p_{T,hadronic} &= E_q \sin\gamma_h\end{aligned}\tag{6.1}$$

The angle γ_h can then be solved for and is:

$$\cos\gamma_h = \frac{(\sum p_T)^2 - (\sum E - p_z)^2}{(\sum p_T)^2 + (\sum E - p_z)^2}\tag{6.2}$$

where the sum runs over all particles or cells excluding the electron or its associated cells. The double-angle method is preferred when the electron is well within the detector acceptance because it relies on position measurements, which are generally more precise than energy measurements. The resolution of the double-angle method deteriorates as the hadronic angle gets large which, at low y , corresponds to low x and Q^2 , as shown in Fig. 6.1. In this measurement, medium values of Q^2 are probed, and the double-angle method gives the best resolution over the majority of the kinematic region. The hadronic angle calculation is based on energy measurements from the calorimeter, but because it has the same energy dependence in the numerator and denominator of Eqn. 6.2, the energy scale uncertainty cancels. The following equations define the Lorentz-invariant DIS variables using the double-angle method:

$$\begin{aligned}Q_{DA}^2 &= 4E_{el}^2 \frac{\sin\gamma_h(1 + \cos\theta_{el})}{\sin\gamma_h + \sin\theta_{el} - \sin(\gamma_h + \theta_{el})}; \\ y_{DA} &= \frac{\sin\theta_{el}(1 - \cos\gamma_h)}{\sin\gamma_h + \sin\theta_{el} - \sin(\gamma_h + \theta_{el})}; \\ x_{DA} &= \frac{Q_{DA}^2}{s y_{DA}}\end{aligned}\tag{6.3}$$

6.1.2 Electron Method

The electron method uses the electron's energy and polar angle to define the event kinematics using the following equations:

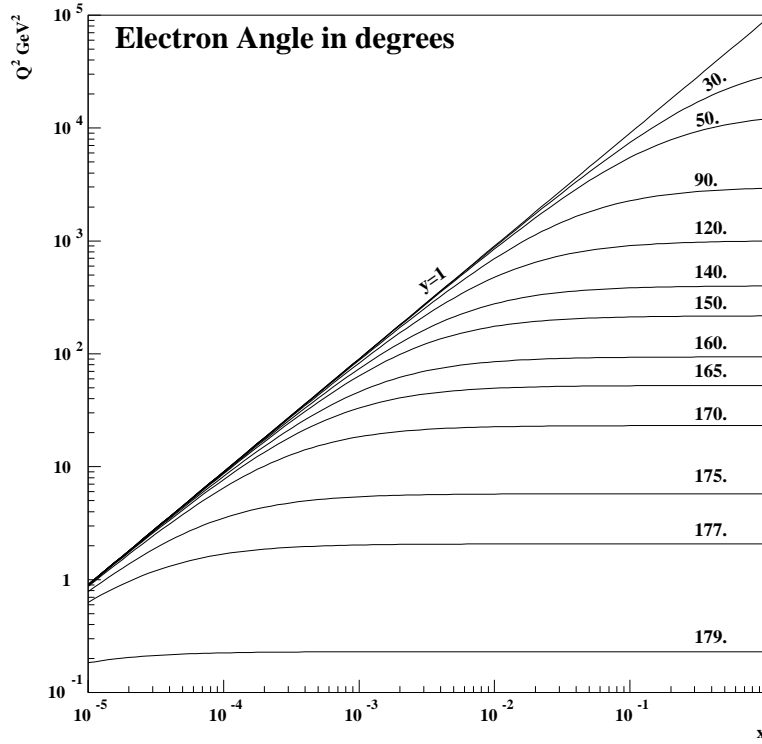


Figure 6.2: Lines of constant electron angle in $x-Q^2$ plane. At lower y -values, the isolines correspond roughly to lines of constant Q^2

$$\begin{aligned}
 Q_{el}^2 &= 2E_{el}E'_{el}(1 + \cos\theta_{el}); \\
 y_{el} &= 1 - \frac{E'_{el}}{2EE_{el}}(1 - \cos\theta_{el}); \\
 x_{el} &= \frac{Q_{el}^2}{s y_{el}}
 \end{aligned} \tag{6.4}$$

The accuracy of this method depends mainly on how well the corrected energy measurement compares with the true energy. The pre-shower detectors described in Sec. 3.2.5.2 are used to refine the measurement of the electron energy. The kinematic isolines for constant electron angle are shown in Fig. 6.2

6.1.3 Jacquet-Blondel Method

This method employs only information from the hadronic system in the event. The following kinematic formulas for the Jaquet-Blondel method can be derived from the DIS variable definitions

given in Sec. 2.4 and the hadronic four-vector.

$$\begin{aligned}
 y_{JB} &= \frac{1}{2E_{el}} \sum_i (E_i - p_{z,i}); \\
 Q_{JB}^2 &= \frac{1}{1 - y_{JB}} [(\sum_i p_{x,i})^2 + (\sum_i p_{y,i})^2]; \\
 x_{JB} &= \frac{Q_{JB}^2}{s y_{JB}}
 \end{aligned} \tag{6.5}$$

This method can be used for neutral and charged current kinematic reconstruction and gives an accurate determination of y at low values.

6.2 Jet algorithms

There are two classes of jet algorithms commonly used, the cone-type and the clustering-type. The cone-type algorithms use geometrical objects to search for where the energy flow through that object is a maximum; the cluster algorithms group nearby particles or energy deposits according to their relative transverse momentum and distance.

The Cone Algorithm

The most commonly used cone algorithms follow the Snowmass Convention. All the particles in the event (where particles can be the partons, hadrons or calorimeter cells) which lie above a minimum transverse energy threshold are taken as the seeds, or initial positions, of the jets for the event. A cone of fixed radius R is defined around a seed in the $\eta - \phi$ plane, and all particles found within this radius are grouped together:

$$\sqrt{(\eta_{seed} - \eta_i)^2 + (\phi_{seed} - \phi_i)^2} < R \tag{6.6}$$

where i indexes all the particles within the cone. This grouping defines the “first-order” jet. The jet variables, E_T , η , and ϕ (azimuthal angle) are then calculated using the particles’ positions inside the

cone, weighted according to their transverse energy.

$$\begin{aligned}
 E_{T,jet} &= \sum_i E_{T,i}; \\
 \eta_{jet} &= \frac{1}{E_{T,jet}} \sum_i E_{T,i} \eta_i; \\
 \phi_{jet} &= \frac{1}{E_{T,jet}} \sum_i E_{T,i} \phi_i
 \end{aligned} \tag{6.7}$$

If the new jet-axis is in a different position than the initial seed position, a cone is again drawn around the position of the jet and the jet properties are recalculated. This process is repeated until the energy flow through the cone is maximal. Once all the jets of the event are defined, a minimum transverse energy threshold is applied to select hard jets.

The cone algorithm allows the possibility to leave some particles ungrouped, that is, not part of any jet in the event. For this reason, it is often used in hadronic collisions where significant energy remains in the detector that does not originate from the hard interaction. The algorithm's drawbacks are its inability to handle overlapping jets without applying some other conditions to the jets, and its dependence on a seed to start the jet finding, which can lead to problems of infrared safety.

The k_T cluster algorithm

The k_T -cluster [54] process begins by defining the quantity

$$d_i = E_{T,i}^2 * R^2 \tag{6.8}$$

for each particle in the event. R is a parameter of the algorithm which represents an upper bound on the jet radius, and is usually set to 1. All the particles are then grouped into pairs and the relative position of the particles is calculated, weighted by the smaller transverse energy of the two.

$$d_{i,j} = \min(E_{T,i}^2, E_{T,j}^2) [(\eta_i - \eta_j)^2 + (\phi_i - \phi_j)^2] \tag{6.9}$$

The minimum value of the set of all $d_{i,j}$, d_i is then considered and if this value is the transverse energy

from a pair, the two particles are grouped together according to the following rules:

$$\begin{aligned}
 E_T &= E_{T,i} + E_{T,j}; \\
 \eta &= \frac{E_{T,i}\eta_i + E_{T,j}\eta_j}{E_T}; \\
 \phi &= \frac{E_{T,i}\phi_i + E_{T,j}\phi_j}{E_T}
 \end{aligned}
 \tag{6.10}$$

If, on the other hand, the minimum value is a single particle, the particle is considered a jet, it is removed and not considered for further clustering. The process of calculating all d_i and $d_{i,j}$ and clustering based on the transverse energies is repeated, and iterated until only jets remain. Finally, a minimum transverse energy threshold is applied to distinguish hard and soft jets, as with the cone algorithm.

The k_T -algorithm is well-suited to finding forward jets and is used exclusively in this analysis. Because it has no fixed radius for jets, it is not as sensitive to soft energy in the vicinity of the jet, whereas the cone algorithm attributes all the energy in a fixed cone radius to the jet. In the forward region and for fixed transverse energy, the jets are highly energetic, and much more collimated or pencil-shaped than jets in the central regions of the detector. The variability of the jet radius is essential for distinguishing between hard jets in the forward region and particles from the proton remnant, which makes the k_T -algorithm preferable to the cone algorithm.

6.3 Breit Frame

Jet finding can be performed in the laboratory frame or in a boosted frame that can sometimes make jet identification easier. Two common boosts in DIS are to the Breit Frame and the hadronic center-of-mass frame. The Breit Frame is defined for ep collisions by the expression: $\vec{q} + 2x\vec{P} = 0$ where \vec{q} and \vec{P} are the 3-momenta of the colliding boson and proton, respectively. In the Breit frame, the boson and a parton in the proton collide on a common axis, as seen for the leading order QPM and QCD-Compton processes in Fig. 6.3. In QPM events, the recoiling quark returns along the common axis with opposite momentum, producing zero transverse momentum. In QCD-Compton and BGF events, the two final state partons are produced with equal transverse energy in the Breit Frame. In this way, the Breit Frame in DIS mimics the final state topology of e^+e^- collisions. This feature of the Breit Frame is convenient for selecting dijet events. By requiring a minimal transverse energy

for the jets in the Breit Frame, QPM events are rejected and events with at least two jets are kept.

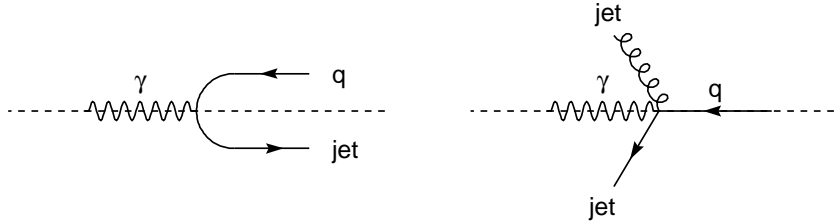


Figure 6.3: The QPM and QCD-Compton diagrams in the Breit Frame. The collision between the quark and the virtual photon occurs on a single axis. In reactions like QPM events, in which there is only one parton in the final state, that final state parton is emitted along the collision axis. In reactions with two partons in the final state, the two partons are emitted off-axis, but balanced in transverse energy.

There are several drawbacks to the Breit Frame. In the NLO calculations discussed in the previous chapter, an exact cancellation of the divergencies due to real and virtual infrared QCD emissions is achieved, provided one integrates over the entire phase space available to the partons. A cut on the transverse energy of the two final-state partons is necessary to use the Breit Frame, and by imposing symmetric cuts on the transverse energy of these partons, the cancellation procedure is disrupted. The problem arises from the reduction in transverse energy of one of the final state partons due to soft gluon emission. When that occurs, the parton does not pass the transverse energy requirement, and the cancellation between these events and events with an ultraviolet divergence does not occur properly. For details see [55]. An explicit selection of dijets is also not ideal for this analysis. In order to retain the region of phase space where there are two jets, one with high- E_T and one with low- E_T , the jet finding needs to be performed in the laboratory frame.

The Breit frame has poorer access than the laboratory frame to low- x , where BFKL dynamics are more likely to be found. Shown in Fig. 6.4 are two histograms in the variable x which illustrate the Bjorken x distribution for Monte Carlo BGF and QCDC events in which a jet is selected in the laboratory frame or the Breit frame. The events are selected in the kinematic region chosen for the analysis, i.e. with Q^2 , y and electron energy cuts given in Sec. 7.2.5. The solid histogram shows the distribution in x for events with a jet with 6 GeV of transverse energy selected in the laboratory frame, while the dotted histogram shows the distribution for events with a jet with 6 GeV

of transverse energy selected in the Breit frame. The plot indicates that more events are selected over the entire x range when jets are selected in the laboratory frame. In the lowest x bins where the statistics are limited, the significant increase in the number of events in the laboratory frame selection above the Breit frame selection makes it the preferred frame.

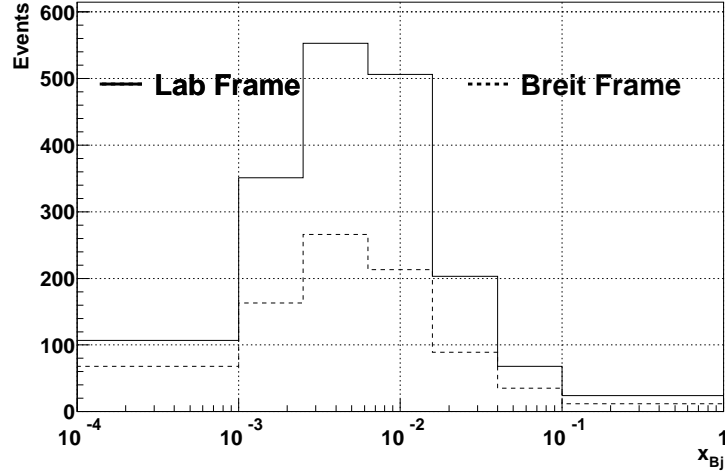


Figure 6.4: Distribution in x_{Bj} for events with jets selected in the lab frame versus the Breit frame.

Another difficulty with the Breit Frame arises from the granularity of the cells in the boosted frame. The cell boundaries in $\eta - \phi$ space are shown for the laboratory frame and a particular boost to the Breit Frame in Fig. 6.5. The Breit Frame stretches out the $\eta - \phi$ space in the forward region, particularly for large values of γ_h , while contracting the geometry in the rear region. This causes the cell boundaries to enlarge with respect to the laboratory frame, which causes the resolution of the jet position measurement to deteriorate.

Finally, the Breit Frame reconstruction introduces an additional uncertainty in the measurement due to its reliance on the electron measurements for the boost. For all these reasons, we have chosen the laboratory frame for this analysis.

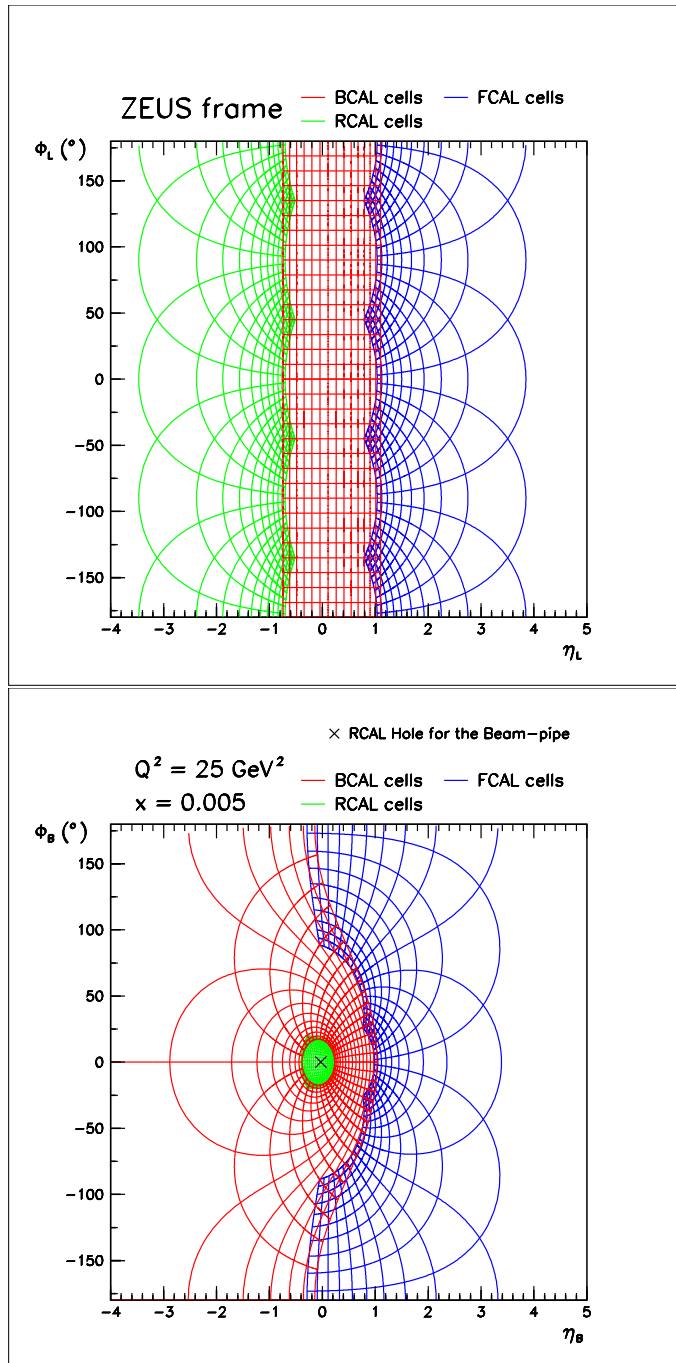


Figure 6.5: Lines defining the cell boundaries in $\eta - \phi$ space for the laboratory frame (top) and a boost to the Breit frame (bottom). The boost is made for $Q^2 = 25 \text{ GeV}^2$ and $x_{Bj} = .005$, which are typical values for the event sample under investigation.

Chapter 7

Event Selection

Selecting the events that will be used for the measurements described in this thesis is a multi-step process. Neutral current DIS events must be triggered, various corrections applied to the raw data in order to ensure the measured energies and tracks are well reconstructed, cuts need to be applied to reject background, and the selection of the kinematic region pertinent to the analysis must be chosen. This analysis of forward jets is done with three separate measurements in three different phase space regions. The first measurement is the most inclusive and the basic trigger and background rejection requirements are developed for that analysis. Modifications to the kinematic region selected are made for the second and third measurement, as detailed in Sec. 7.2.5.

7.1 Triggering on DIS Events

The most reliable signature for a deep inelastic scattering event is a reconstructed scattered electron. At the most basic level, the electron is identified as an isolated electromagnetic deposit in the calorimeter with the Calorimeter First Level Trigger (see Sec. 3.2.3). At higher levels of triggering, the calculations for electron identification need not be as fast, allowing more sophisticated algorithms. An electron can be identified through its shower shape. Electrons emit photons through the process of Bremsstrahlung when they are accelerating or decelerating. The shower that is produced deposits all its energy in the electromagnetic portion of the calorimeter, and has, therefore, a very short and narrow profile.

7.1.1 GFLT

At the first stage of triggering, global information is taken from the CFLT and the CTD FLT to make loose selections on possible DIS event candidates. Global sums such as total energy in the calorimeter or total transverse energy are used in combination with loose tracking requirements to distinguish classes of real physics events. In order to be included in the event sample used for the measurements described here, one of the following combinations of requirements on the calorimeter energy sums and CTD tracks must have been met. In order for a track in the CTD to be considered a “good track” it must have a z position in the first superlayer between -50 cm. and 80 cm and point to the reconstructed vertex. Other CTD tracks are considered for triggering if they pass some minimal quality cuts. The trigger requirements are equivalent to a selection of one of the GFLT slots 40-43.

- $E^{CAL} > 15\text{GeV}$ with a good track
- $E_T^{CAL} > 30\text{GeV}$ or $E_T^{CAL} > 11.6\text{GeV}$ with a good track
- $E^{EMC} > 15\text{GeV}$ or $E^{EMC} > 10\text{GeV}$ with a good track
- $E^{BEMC} > 3.4\text{GeV}$ with a good track or $E^{BEMC} > 4.8\text{GeV}$ with any track
- $E^{REMC} > 3.4\text{GeV}$ or $E^{REMC} > 2\text{GeV}$ with a good track

7.1.2 GSLT

At the second level, information from most detector components is available for triggering, and basic quantities such as $E - p_z$ of the calorimeter energies is used to reject background events which contain no electron. Events in which the particles emitted from the hard scattering are completely contained in the detector will have an $E - p_z$ of 55 GeV. Since the $+z$ axis is defined to be along the proton beam direction, the $E - p_z$ of the incoming proton is 0, while the $E - p_z$ of the incoming electron is $27.5 - (-27.5) = 55\text{GeV}$. By conservation of energy and momentum, the total outgoing $E - p_z$ must also sum to 55 GeV, provided all the outgoing energy is correctly measured. In DIS events with initial state radiation, the photon escapes down the rear beampipe and lowers the $E - p_z$ measurement. To compensate for this effect, the energy of the photon as measured by the lumi

gamma detector is included. A measurement of the event vertex is made using only the axial wires of the CTD (z-by-timing), but with rather poor resolution. Further cuts can be applied to the timing of the calorimeter energies in order to reject beamgas background, sparks and cosmic ray events.

This analysis requires SFEW SLT trigger slot 6 to fire. The requirements of this slot are the following:

- $E^{REMC} > 2.5GeV$ or $E^{BEMC} > 2.5GeV$ or $E^{FHAC} > 10GeV$ or $E^{FEMC} > 10GeV$
- $E - p_z + 2 \times E_\gamma^{lumi} > 29GeV$. The lumi gamma measurement is included for ISR events (see Sec. 4.5) in which the emitted photon escapes down the RCAL beampipe. This loss of energy makes the calorimeter measurement of $E - p_z$ alone insufficient.

7.1.3 TLT

Once the second level trigger decision is made, the measurements made by all components of the detector are sent to the event builder for full reconstruction by the TLT.

At the third stage of triggering, the full tracking reconstruction is run and jet finding using two different algorithms is performed. Four different electron finders are run in order to select electron candidates as efficiently as possible [56]. A much improved vertex-finding algorithm is run at the TLT. This improves the $E - p_z$ measurement with respect to the SLT, and a tighter cut $E - p_z + 2 \times E_\gamma^{lumi} > 30GeV$ is applied to further reduce background.

The events for this analysis are selected with the SFEW TLT filters DIS03 or DIS04. DIS03 is the medium Q^2 filter that requires either an electron to be found with at least 4 GeV of energy and outside a radius of 25cm. on the face of the RCAL. For an event vertex at the nominal $z=0$ position, this radius cut corresponds to a Q^2 cut $Q^2 > 20GeV$. DIS04 is the high- Q^2 trigger that requires one of the four electron finders to find an electron with energy $E_{el} > 7GeV$ outside a box cut of 30x30 cm on the face of the RCAL.

Once the TLT has made its selection, a further software selection is made which groups events according to DST bits. This analysis requires DST bits 9,11, or 13 to fire. Once this final selection is made, the events are written to tape.

7.2 Offline Event Reconstruction

Once the events are triggered and written to tape, a more precise reconstruction of the event quantities can be performed. The data are also corrected to ensure the fundamental measurements (i.e. cell energies) are accurate and reliable. Before any quantity that relies on the calorimeter measurement is calculated, noisy calorimeter cells are removed by the NOISE96 [57] routine. This noise typically comes from electrostatic discharge between the high voltage bases of the photomultiplier tubes.

An additional correction is made to the cells, using the routine RCALCORR [58]. This routine recalibrates the calorimeter cells so that the energy response in data and Monte Carlo are the same. This correction makes up for deficiencies in the Monte Carlo's ability to reproduce the data, which is necessary for the extraction of any cross section. The calibration factors are determined by two different methods, depending on whether the factor is to be applied to the RCAL or the BCAL cells (no alteration of the FCAL cells is made). For high Q^2 events where the electron is scattered at an angle inside the CTD acceptance region, the calorimeter measurement of the electron energy can be compared to the electron energy calculated using the double-angle method (see Sec. 6.1). The double angle method is more reliable because the position resolution of tracks in the CTD is very good, and the difference between the two measurements is taken as the calibration factor. For recalibration in RCAL, kinematic peak events are used. Events are selected with a scattered electron very close to the RCAL beampipe and at low y , in order to select a sample whose distribution of electron energies peak at 27.5 GeV, the incoming beam energy. The difference between the observed peak and 27.5 GeV is taken as the calibration factor for RCAL.

A neural network is used to identify the scattered electron, and the subdetectors SRTD, Rear Presampler and HES are used to correct the electron's energy and position (see next section). The angle of the hadronic system is corrected using the CorandCut routine. This routine is an iterative algorithm for removing energy deposits that are far from the initial calculation of the hadronic angle and have a timing measurement inconsistent with the ep collision. A jet finder is run on the cell energies included in the hadronic final state. However, both electromagnetic and hadronic deposits in the calorimeter that are well-reconstructed are not necessarily equal in energy to the electron and

groups of particles that make up a jet. This is because the particles emitted from the hard scattering must travel a long distance before reaching the calorimeter, and travel through other uninstrumented parts, so-called dead material, of the detector. The particles lose some of their energy while traversing the detector, and this loss in energy needs to be corrected for in the offline event reconstruction.

7.2.1 Positron Reconstruction

Positron candidates are identified using the neural network program Sinistra [59]. This program takes the transverse and longitudinal energy profiles of electromagnetic cells (grouped into islands) from the entire calorimeter as input and calculates the probability (between 0 and 1) that each electromagnetic island resulted from a real scattered electron. The program is trained on neutral current DIS Monte Carlo, and is 80% efficient at finding electrons if the energy of the electromagnetic deposit is larger than 10 GeV and the probability given by Sinistra is larger than 0.9.

Sinistra delivers a list of candidates along with their properties and orders them according to their probability. An electron has high probability, close to 1, if it is well-isolated, its shower profile is short and wide, and it has high enough energy. If 2 or more candidates have the same probability, the one with the highest energy is considered the leading candidate (Findis Option 1). To estimate how much energy the electron lost due to showering in the dead material, the SRTD or RCAL Presampler measurements are used (see Sec. 3.2.5.2). The electron position is corrected by either the SRTD, HES or by a matching track. This prescription for correcting the electron was developed for the 96/97 F_2 analysis [60] and more detail can be found in [55].

7.2.2 Jet Reconstruction

The jet finding is performed on all cells associated with the hadronic final state of the event. That is, the cells associated with the most probable Sinistra electron candidate are removed and the jet finder is run on all remaining energy deposits in the calorimeter.

7.2.3 Jet Energy Correction

Correcting for the energy lost by a jet in the dead material of the detector is more complicated than for the electron. Because jets are sprays of various particles, all which interact with matter differently, measuring the energy loss with a pre-shower detector is not possible. Instead, we rely on

the Monte Carlo simulation of the dead material. The length of the dead material the jet must pass through is dependent on its polar angle. Therefore, the full pseudorapidity region which is measured is divided into 20 slices, each covering 0.2 units in η . In each region, a profile plot is made of the detector jet's transverse energy in bins of the hadron level jet's transverse energy. Two linear fits of the dependence is made, one with $E_{T,jet}^{HAD} < 40GeV$, the other with $E_{T,jet}^{HAD} > 40GeV$. An example of one such profile plot is shown in Figure 7.1. The parameters of the fit are extracted and applied as corrections to the data.

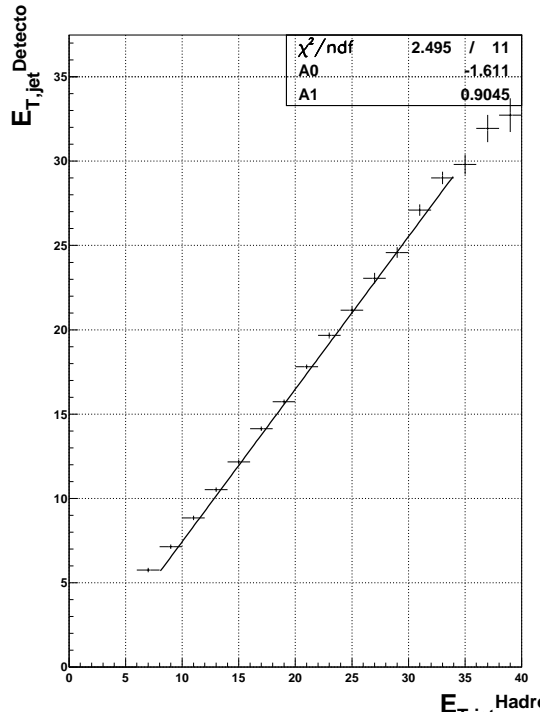


Figure 7.1: Profile plot of detector level jet transverse energy in bins of hadron level jet transverse energy for NC DIS Monte Carlo. The jet transverse energy in the data is scaled by the parameters of this fit.

7.2.4 Cuts to Reject Background

To further ensure that DIS events are selected and to clean the sample of questionable DIS signatures, the following requirements are made of the data and detector level Monte Carlo.

- $|Z_{vtx}| < 50cm$. A found vertex by the CTD in this range ensures that the event is well contained

within the acceptance of the detector and that the angles of the electron and hadronic system are well-reconstructed.

- $38 < E - p_z < 65$ This cut removes photoproduction events and events in which a significant portion of the energy escapes down the RCAL beampipe.
- $y_{el} < 0.95$ There is a small class of events in which a photon or neutral pion fakes the signature of an electron in the forward region of the detector, resulting in very high values of y_{el} . This cut removes those events.
- $p_T^{CAL} / \sqrt{E_T^{CAL}} < 3$. This cut removes cosmic ray events. DIS events should have total transverse momentum $p_T^{CAL} \sim 0$. Most cosmic ray events are cut by the timing requirements at the GSLT, but this requirement removes the small class of cosmic events in which the muon travels through the center of the BCAL at the same time as the beam bunches cross inside the detector and has, therefore, an acceptable timing.
- $|X_{el}| > 14$ || $|Y_{el}| > 14$ where X_{el} and Y_{el} are the raw (uncorrected) positions of the electron on the face of the calorimeter. This “boxcut” removes events in which the electron impacts the detector close to the beampipe where the reconstruction of the electron is not very good.
- $E^{NotInCone} / E_{el} < 0.1$ where $E^{NotInCone}$ is the energy inside a cone of radius 0.8 around the electron not associated with the electron itself. This isolation requirement rejects events in which the electron is not well-separated from the jet and cannot be properly reconstructed.

7.2.5 Phase Space Selection

The phase space selection is made where BFKL dynamics might be present given the acceptance limitations of the detector. To reach a kinematic region where BFKL effects might be visible, it is necessary to measure as low in Q^2 and $E_{T,jet}$ as possible. Because BFKL dynamics are expected to be a small effect and because no NLO BFKL calculation was available at the time of this analysis, we attempt here to look for a breakdown of the NLO QCD prediction using DGLAP evolution. The measurement is initially made as inclusively as possible, where NLO QCD is expected to reproduce the data well. This cross section is dominated by Quark-Parton Model events. An example of such

a QPM event is shown in Fig. 7.2. The measurement is made a second time in a more restrictive phase space in order to exclude quark-parton model (QPM) events. This second phase space region will henceforth be referred to as “QPM Suppressed Phase Space.” The events making up this phase space selection are typically dijet events with the current jet in pseudorapidity regions corresponding to the central and rear parts of the detector, and target jets in the forward region of the detector. Two examples of such events are shown in Figs. 7.3 and 7.4. The measurement is made a third time in a more restrictive phase space suggested by Mueller for BFKL searches. This third phase space region will henceforth be referred to as “BFKL Phase Space.”

Listed below are the common cuts made on data and detector level Monte Carlo for all three measurements. They are exactly the phase space requirements put on the inclusive measurement.

- $Q^2 > 25 \text{ GeV}^2$ This cut is made to select events above the Q^2 limit imposed by the trigger.
- $y_{jb} > 0.04$. This cut ensures good reconstruction of the hadronic system, which is necessary for the double-angle reconstruction of the kinematics.
- $E_{el} > 10 \text{ GeV}$ of the Sinistra95 most probable candidate. This is the region where Sinistra can select positrons with an efficiency greater than 80%.
- $E_{T,jet} > 6 \text{ GeV}$ and $-1 < \eta_{jet} < 3$. Jet cuts are selected to ensure the jets are well measured. At low transverse energies and high pseudorapidity, the jet finding efficiency and purity is low because either the jets lose a large fraction of their energies in dead material or a portion of their energy escapes down the FCAL beampipe.

For the QPM suppressed measurement, the following additional requirements are made:

- $\cos\gamma_h < 0$. This requirement ensures that the hadronic angle is found in the rear half of the detector. This cut, in combination with the following one, effectively removes QPM events where the jet axis is aligned with the hadronic angle
- $\eta_{jet} > 0$.

For the BFKL measurement, the following additional requirement is made:

- $0.5 < E_{T,jet}^2/Q^2 < 2$. This requirement limits the Q^2 evolution of the particles on the gluon ladder.

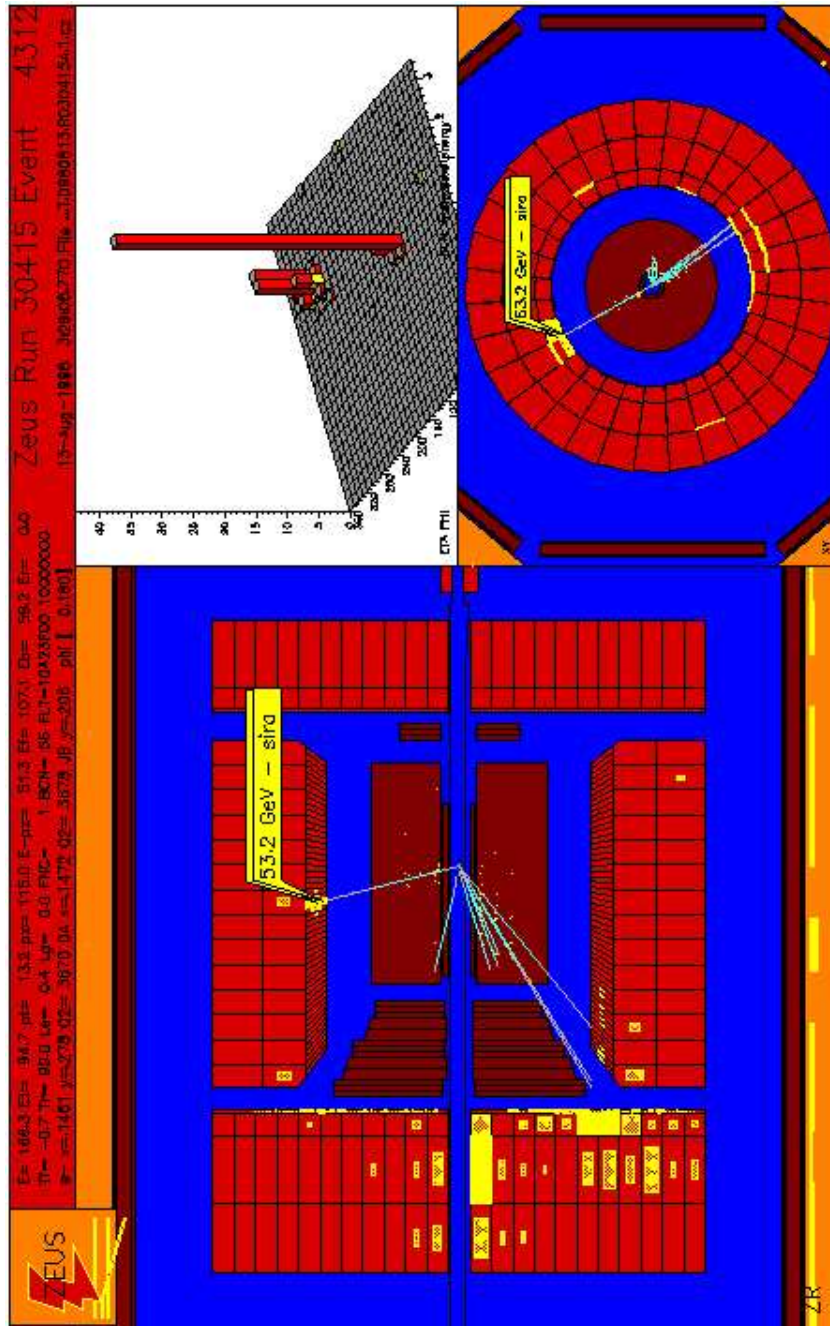


Figure 7.2: Event picture from Inclusive Phase Space sample. On the left, a cross sectional slice of the calorimeter is seen with the DIS electron located in the central region of the Barrel Calorimeter. The energetic jet is located in the lower part of the Forward Calorimeter (left). The remaining energy is due to the proton remnant. On the top right side a lego plot illustrates the transverse energy measured in the event in the $\eta - \phi$ plane. The electron's energy is very localized in the taller peak, while the jet energy is distributed among more cells. On the lower right a view of the calorimeter from the perspective of the beampipe shows the balance of transverse energy between the jet and electron in single jet events.

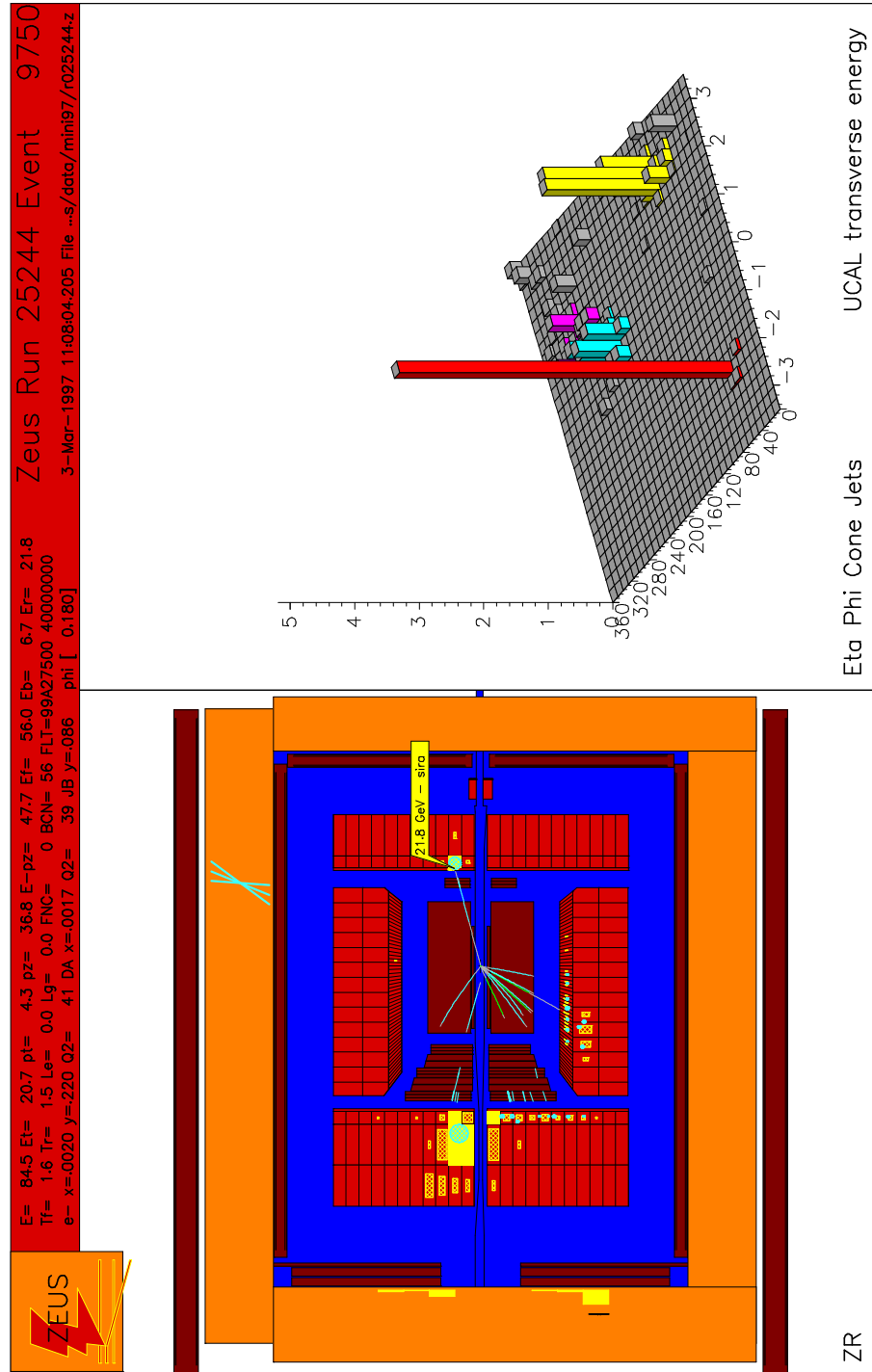


Figure 7.3: Event picture from QPM Suppressed Phase Space sample. The event contains a significant energy deposit in the barrel calorimeter, and a hard forward jet in the forward calorimeter. The separation distance between the electron, the forward jet and the central ($\eta \sim 0$) energy deposit is shown as a lego plot in $\eta - \phi$ space on the right.

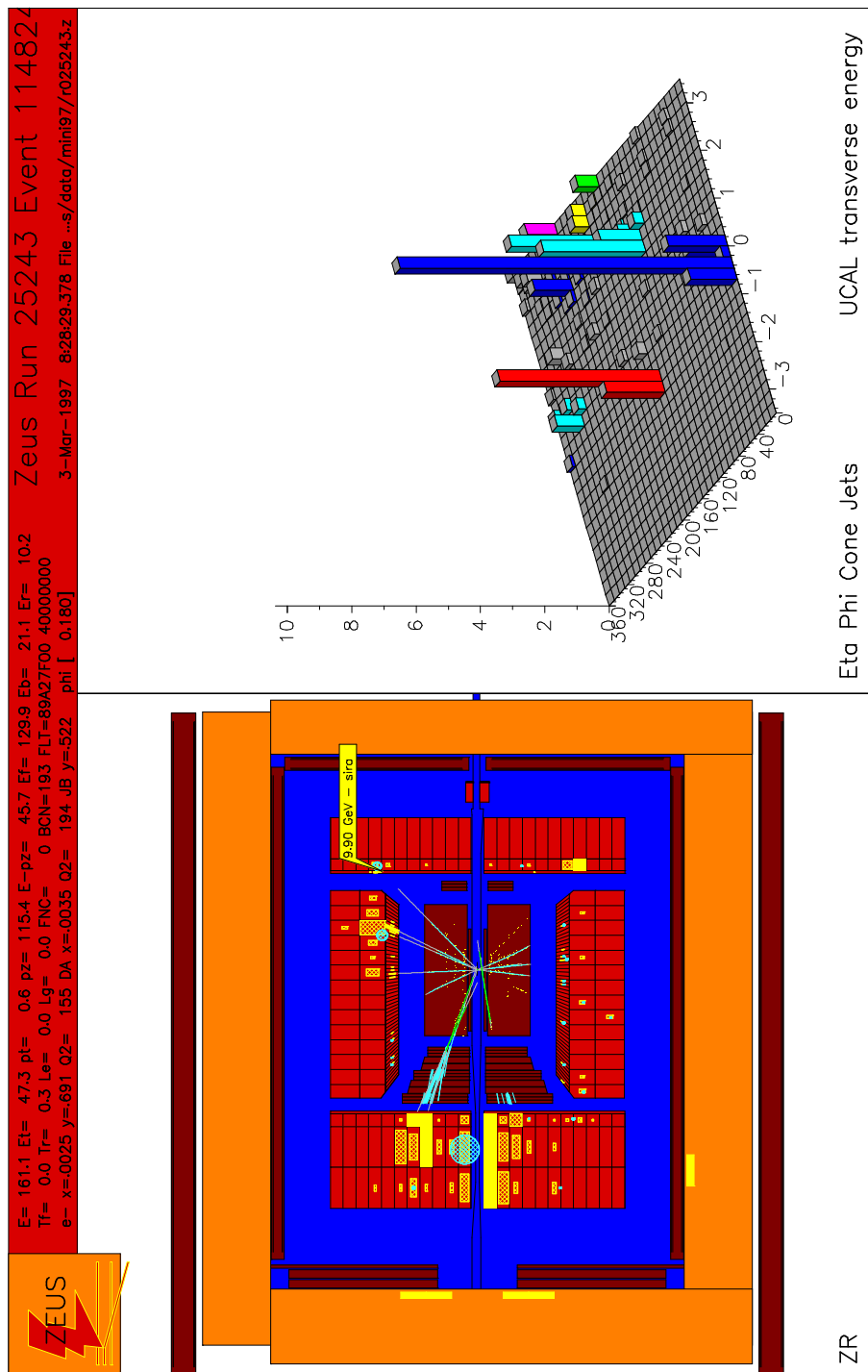


Figure 7.4: Event picture from QPM Suppressed Phase Space sample. The event contains a significant energy deposit in the barrel calorimeter, and a hard forward jet in the forward calorimeter.

Chapter 8

Description of the analysis

The aim of this analysis is to measure hard forward jets¹ originating from events initiated by a gluon in the proton (i.e. Boson-Gluon Fusion Events). An excess in the rate of such events over QCD predictions using DGLAP evolution of the parton densities might indicate the presence of BFKL dynamics. Such an effect is expected to be small since it has not been observed yet in other low- Q^2 analyses at HERA. We also expect the error from the renormalization scale uncertainty to be much larger than the experimental errors, as has been seen in the dijet analysis at low- Q^2 from ZEUS [61], where Boson-Gluon Fusion events dominate the sample. Such large theoretical error makes the extraction of a possible BFKL signal more difficult. Therefore, the analysis cuts are chosen to minimize the theoretical error.

In the kinematic region covered by HERA collisions, NLO DGLAP has been tested in inclusive measurements (e.g. the measurement of the proton structure function F_2) down to $x_{Bj} \sim 10^{-5}$, and in exclusive jet measurements at higher x_{Bj} with great success. Therefore, the only regions left untested for BFKL dynamics are exclusive jet final states and diffractive final states at low- x_{BJ} . With this analysis, we track the potential transition from DGLAP to BFKL dynamics by initially measuring the inclusive forward jet cross section, and then measure in successively more restrictive regions of phase space in order to narrow the search for BFKL dynamics. We have defined three different phase space regions, ordered in increasing restrictiveness, in which to measure the forward jet cross section. Initially, we measure inclusive jet production in the lab frame with restrictions on

¹Hard forward jets are defined as jets at high pseudorapidity and high transverse energy originating from partons in the gluon ladder.

the jet transverse energy and pseudorapidity. In the second measurement, we restrict the hadronic angle of the event in order to suppress quark-parton-model (QPM) events which are expected to be well-described by DGLAP. In the third and final measurement, forward jet events are selected such that the events favoring DGLAP evolution are removed, according to the prescription by Mueller and Navalet [19, 20].

After defining the kinematic region for each measurement, a series of studies using Monte Carlo data need to be performed in order to demonstrate the reliability of the measurement. A hadron-level cross section is one in which the detector effects are removed, and, therefore, do not create biases in the measurement. It is defined as follows:

$$\sigma_i = \frac{N_i^{data}}{\mathcal{L}} C_i = \frac{N_i}{\mathcal{L}} \frac{N_i^{hadMC}}{N_i^{detMC}} \quad (8.1)$$

where i indexes the bin, \mathcal{L} is the total luminosity of the data, N_i^{data} is the number of data events measured in the bin and C_i is the correction factor determined from the MC to correct for detector effects in that bin. This factor is the number of events in the MC passing the hadron level cuts in a bin divided by the number of events in the MC passing the detector level cuts in the same bin. The process of correcting for detector effects in order to obtain the true cross section as described here is ideal provided that the MC can exactly reproduce the data distributions in all variables. When the Monte Carlo distributions do not mirror the data distributions, the differences are accounted for in the systematic error of the measurements (see Sec. 9.4).

The correction factor C_i can be written as the quotient of two quantities, the event finding efficiency and purity, $C_i = \text{purity}/\text{efficiency}$. The efficiency is a measure of what percentage of events generated in the MC sample for a particular bin are reconstructed at the detector in the same bin. An event would not be reconstructed if it lost too much of its energy in dead material or the event occurred outside the detector's acceptance. The efficiency is defined to be:

$$\text{efficiency} = \frac{\text{generated at the hadron level AND reconstructed in the detector}}{\text{generated at the hadron level}} \quad (8.2)$$

The purity is a measure of how many events found in the detector in a particular bin can be derived from an event generated in the same bin, and not from background processes. The purity is defined

to be:

$$purity = \frac{\textit{generated at the hadron level AND reconstructed in the detector}}{\textit{reconstructed in the detector}} \quad (8.3)$$

The largest contamination of the forward jet measurement comes from counting events in which energy associated with the proton remnant contributes to the jet energy measurement. The remnant itself escapes down the forward beam pipe, but the color connection between the remnant and the forward jet can produce soft particles in the forward direction that can artificially increase the energy of a forward jet, causing it to be assigned to an incorrect bin.

To achieve a precise understanding of the jet finding efficiencies and purities, jets that are generated at the hadron level are matched with their detector level counterpart. If such a matching were not performed, events in which a jet generated in one area of the phase space (i.e. pseudorapidity or transverse energy) with no detector level counterpart could contribute toward the efficiency due to the presence of a second jet in another area of phase space. Such an occurrence would artificially enhance the jet finding efficiency. The matching procedure is carried out by looping over all reconstructed jets passing cuts for each generated jet in the event, starting with the highest $E_{T,jet}$. If the generated and reconstructed jets being compared are within 1-unit of R in eta-phi space, as defined by:

$$R = \sqrt{(\eta_{jet}^{det} - \eta_{jet}^{had})^2 + (\phi_{jet}^{det} - \phi_{jet}^{had})^2} < 1 \quad (8.4)$$

they are matched and the reconstructed jet is not considered in further hadron-detector jet comparisons.

The generated values of event and jet variables can be compared with their reconstructed values to determine approximately how much energy was lost in the dead material, and whether each reconstructed value is close enough to the true value in order to unfold the cross section reliably using the chosen binning. If the binning is too small compared with the resolution in that bin, too many events will smear out into the adjacent bin, thereby distorting the differential cross section. Smearing is a result of uncertainties in the detector measurements. The resolution of a measured value is defined as its variance with the generated value. In order to obtain a numerical estimation of the variance, the difference between the generated and reconstructed values, sometimes scaled by the generated value (e.g. $(Q_{recon}^2 - Q_{true}^2)/Q_{true}^2$), is histogrammed and fit with a Gaussian function,

and the variance extracted from the fit. Smearing is defined to be:

$$\text{smearing} = \frac{\text{generated at the hadron level AND reconstructed in the detector}}{\text{generated at the hadron level AND reconstructed in any bin}} \quad (8.5)$$

As an example, if the resolution in a particular bin is 20% and the bin width is 20% of the average value in the bin, 34% of the reconstructed events will, on average, move into the adjacent bins. As a general rule, the binning is chosen to be larger than 3σ in the resolution.

8.1 Inclusive Jet Measurement

The cross sections measured in this analysis are defined for kinematic regions chosen at the hadron level. It is desirable to measure the data in exactly the same region as defined by the hadron level requirements, in order to maximize the integrity of the measurement. One can make the measurement in a smaller region of phase space and then extrapolate to the hadron level definition through the unfolding of the cross section, but one must then rely on the assumption that the behavior of the cross section is well understood in the extrapolated region. A Monte Carlo data sample for the Inclusive Jet Measurement was created by requiring the following of the events at hadron/parton levels:

- The generated Q^2 is greater than 25 GeV. This value is chosen to make the measurement where the DIS data is well understood and the trigger efficiency and acceptance is high.
- The generated y is greater than 0.04. This value is consistent with the value chosen in the F_2 analysis and selects the region where the hadronic final state is well-reconstructed.
- The generated electron energy is greater than 10 GeV. An extrapolation of the cross-section to smaller values of electron energy was found to create a substantial impurity at low x .
- One jet with transverse energy greater than 6 GeV and pseudorapidity between -1 and 3 is required to be found in the laboratory frame using the longitudinally-invariant inclusive k_T -algorithm. The lower bound on the transverse energy ensures good reconstruction of a hard jet and the pseudorapidity requirements are chosen based on detector acceptance and jet finding efficiency and purity.

The laboratory frame is chosen for the jet finding in order to reach the lowest values of x_{Bj} and to maximize the cell resolution in the forward region, as explained in Sec. 6.3.

8.1.1 Comparison of Data and Monte Carlo

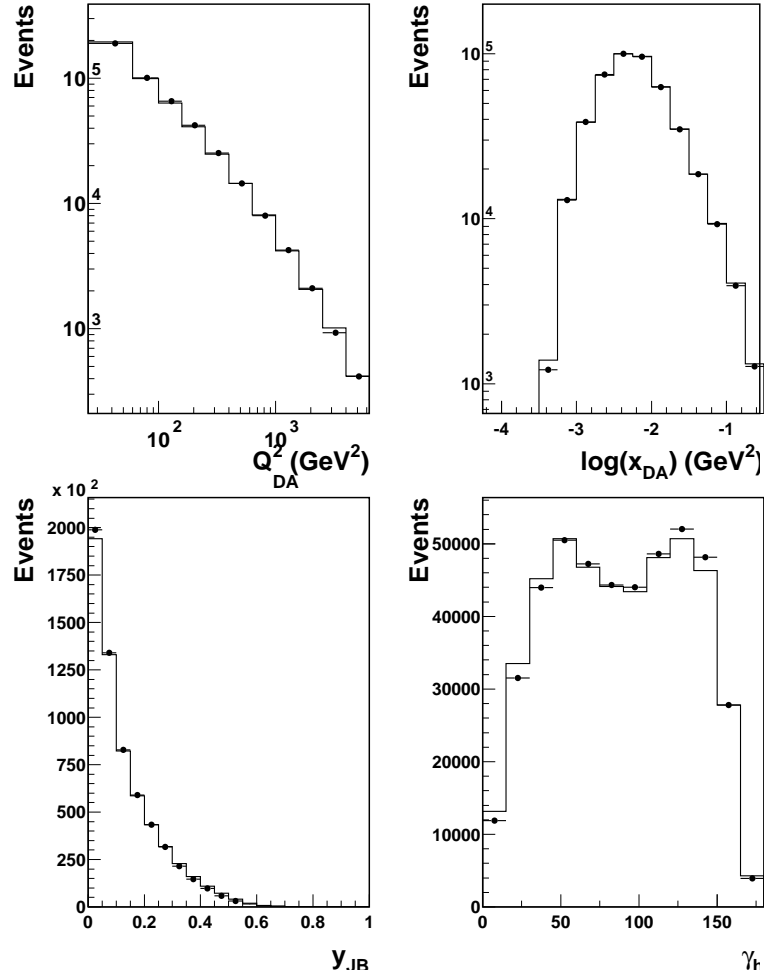


Figure 8.1: Comparison of data and MC for Q^2 , x , y and γ_h in the Inclusive Phase Space. The data are compared to the Color Dipole Model ARIADNE Monte Carlo. The distributions are normalized to the number of events in the data in order to compare their shapes.

In order to reliably unfold a measured cross section to the hadron level, we rely on the detector level Monte Carlo to describe the shape of our data quantities. The ARIADNE Monte Carlo is used for all data and MC shape comparisons. The plots are normalized to the number of events in the data in order to make the comparisons. Shown in Fig. 8.1 are the data and MC distributions for Q^2 ,

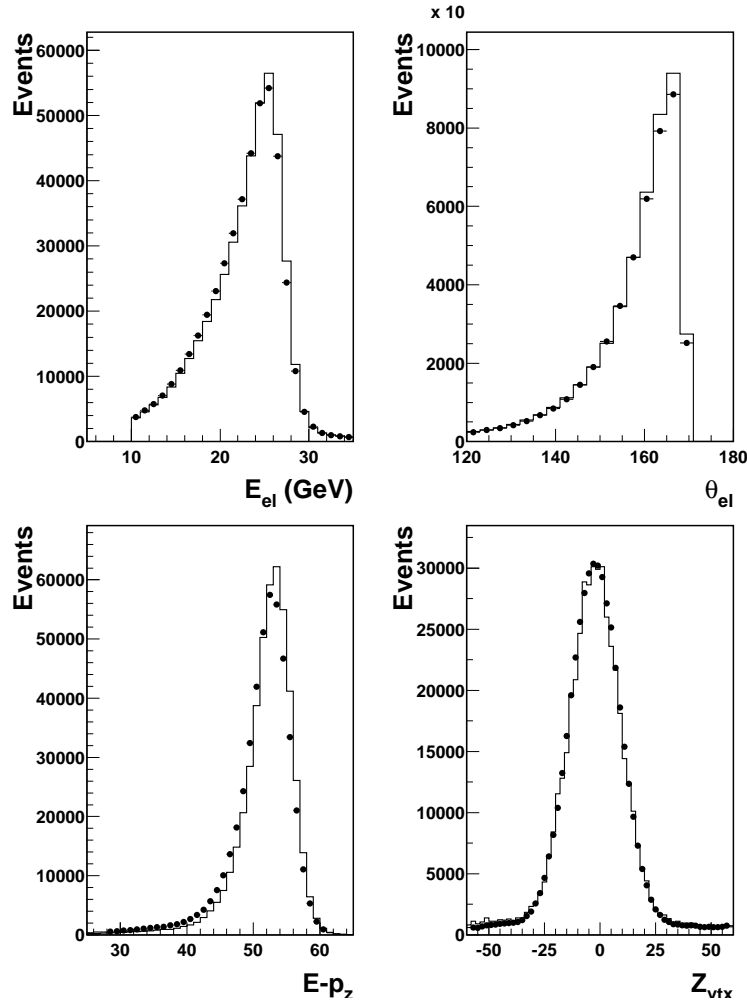


Figure 8.2: Comparison of data and MC for electron energy, electron angle, $E - p_z$ and z-vertex in the Inclusive Phase Space. The data are compared to the Color Dipole Model ARIADNE Monte Carlo. The distributions are normalized to the number of events in the data in order to compare their shapes.

x_{Bj} , y_{JB} and γ_h . The kinematics are reconstructed using the Double-Angle method, as described in Sec. 6.1. The variables are very well described by the Monte Carlo. Shown in Fig. 8.2 are the shape comparisons for reconstructed event quantities. A good description of the electron energy variables is necessary for accurate selection of DIS events. Although the description of the electron energy distribution by the Monte Carlo is not perfect, it is comparable to the level of accuracy obtained by the F_2 analysis [56]. The $E - p_z$ description is not very good due to a weak understanding of the electromagnetic energy scale. The effect on the measurement is quantified by the systematic error induced by changing the $E - p_z$ cuts. The error is found to be small, as described in Sec. 9.4. The z-vertex is an input to the Monte Carlo generator, and its distribution is determined from the full NC DIS data sample. Any disagreement between the data and MC, therefore, is due to the difference in the vertex distribution between the full NC DIS sample and the inclusive jet sample.

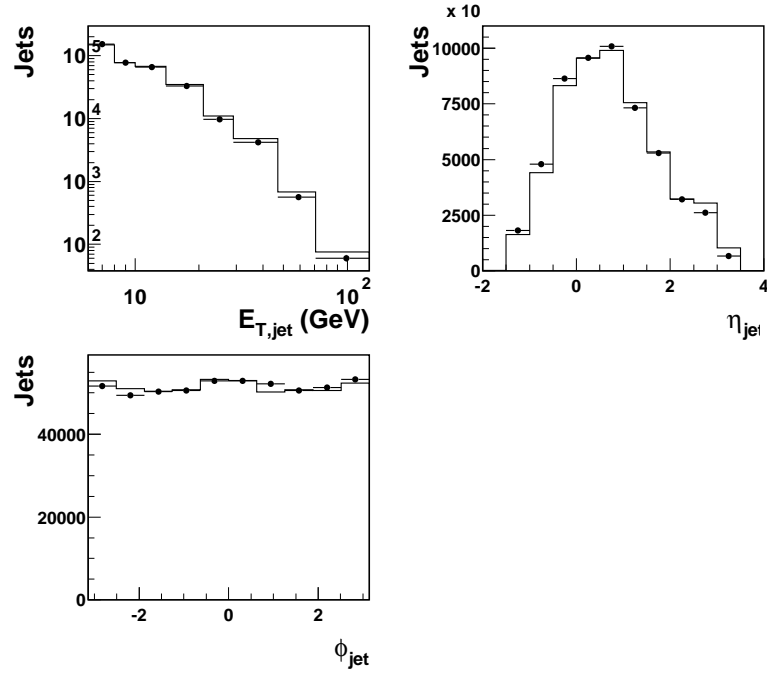


Figure 8.3: Comparison of data and MC for the jet variables transverse energy, pseudorapidity and azimuthal angle in the Inclusive Phase Space. The data are compared to the Color Dipole Model ARIADNE Monte Carlo. Every jet that passes detector cuts contributes to the histogram. The distributions are normalized to the number of entries in order to compare their shapes.

The jet variables $E_{T,jet}$, η_{jet} and ϕ_{jet} are shown in Fig. 8.3. The pseudorapidity is falling in

the forward region due to the restriction on y . The jet distribution in azimuthal angle, ϕ , is flat, as expected. In general, the shapes of the jet distributions are well-described.

8.1.2 Purities, Efficiencies, Correction Factors

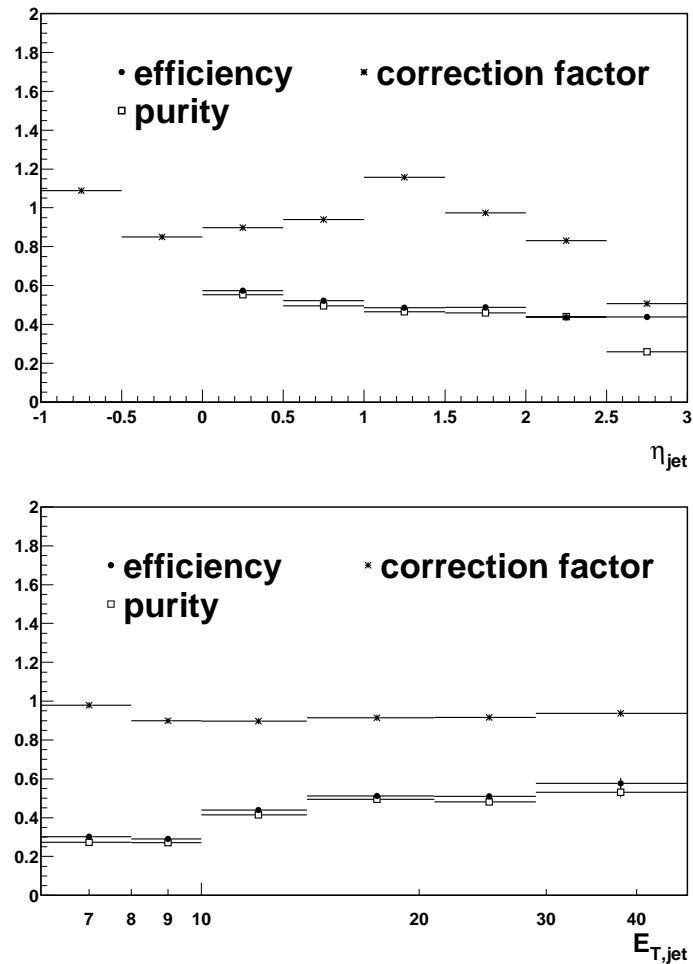


Figure 8.4: Efficiency and purity of the jet finding for jet variables pseudorapidity and transverse energy in the Inclusive Phase Space, with the associated acceptance correction factor.

Shown in Fig. 8.4 are the jet finding efficiencies and purities for the jet variables η_{jet} and $E_{T,jet}$. The efficiencies and purities are generally around 60%, though they drop in the forward region and at low jet transverse energy. The efficiency in the forward region is sensitive to energy losses down the forward beam pipe, while the purity is sensitive to contamination from the color string between the forward jet and the proton remnant. The efficiency drops and the purity rises in

the bin $1 < \eta_{jet} < 1.5$ due to energy losses in the crack between the forward and barrel calorimeters. The correction factor applied to the data for unfolding the cross section is generally around 1, but can be as large as $\pm 40\%$. Every set of matched jets between hadron level and detector level contribute to the plot, to reflect the fact that we are interested in the *inclusive* jet measurement.

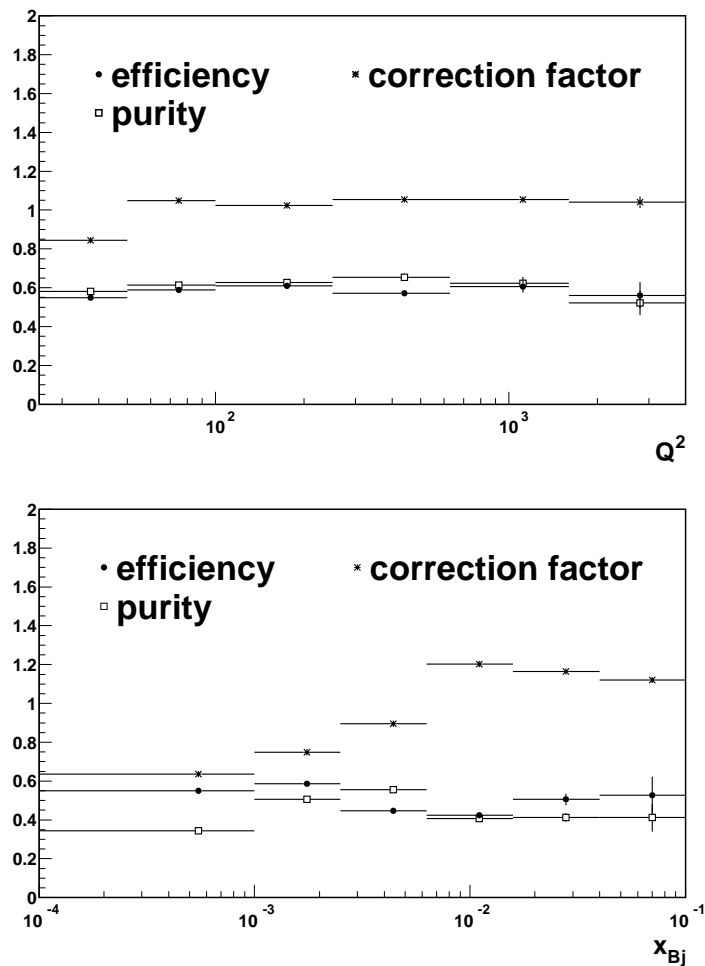


Figure 8.5: Efficiency and purity for events containing a forward jet in the Inclusive Phase Space, with the associated acceptance correction factor.

Fig 8.5 illustrates the efficiency and purity in event variables Q^2 and x_{Bj} . No jet matching between hadron level and detector level jets is required, and each event contributes to the plot only once. The efficiency and purity are near 80% in Q^2 , though they drop in the lowest Q^2 bins. The efficiency and purity in the most populated bins of x_{Bj} are around 60%, though the purity drops in

the low x bins. The smaller the efficiencies and purities, the more reliance is placed on the unfolding of the cross section by the Monte Carlo.

8.1.3 Resolutions

Fig. 8.6 illustrates the resolution of the event variable Q^2 and the jet variables $E_{T,jet}$ and η_{jet} in bins of the reconstructed quantity. In the left column, the resolution in one bin is histogrammed and fit with a Gaussian. The bin chosen for each of the three variables is the one bordering the cut. The fit parameters are shown in the statistics box. In the right-hand column, the resolution is plotted as a function of the variable of interest. The points are placed at the mean of the Gaussian fit, and the error is the 1σ value extracted from the fit. The binning chosen is the one used for the cross section measurement.

In the first bin of Q^2 the resolution is found to be 5%, or 1.25 GeV. Therefore, the bin width of 25 GeV is much wider than a boundary given by 3σ in the resolution. The resolution improves in higher Q^2 bins. In the lowest $E_{T,jet}$ bin, the mean of the resolution plot is shifted by about 6% and there is a tail indicating that the reconstructed transverse energy is larger than the true energy. This is due to the fact that reconstructed jets with less than 6 GeV of transverse energy are not included. In larger bins of transverse energy, the distribution is symmetric and centered on zero. The resolution in η_{jet} is generally between 5 and 10%, and there is a shift toward lower reconstructed values in the most forward bin. This is expected, as the true position of the jet is more forward since it is not constrained by the detector limitations. The shift of $\sim 7.5\%$ is tolerable because it is not larger than the bin width.

8.1.4 ISR/FSR Corrections

The NLO calculations do not include corrections to the cross section due to photon radiation. Therefore, correction factors computed with Ariadne are calculated and applied bin-by-bin to the data and Monte Carlo cross sections in order to make them comparable to the NLO calculation. Shown in Fig. 8.7 are the correction factors applied to the cross sections in the Inclusive Phase Space in jet pseudorapidity, transverse energy, Q^2 and x_{Bj} . The cross section without radiative corrections, N_{Born} , is divided by the cross section with radiation included, N_{rad} , to compute the correction factor.

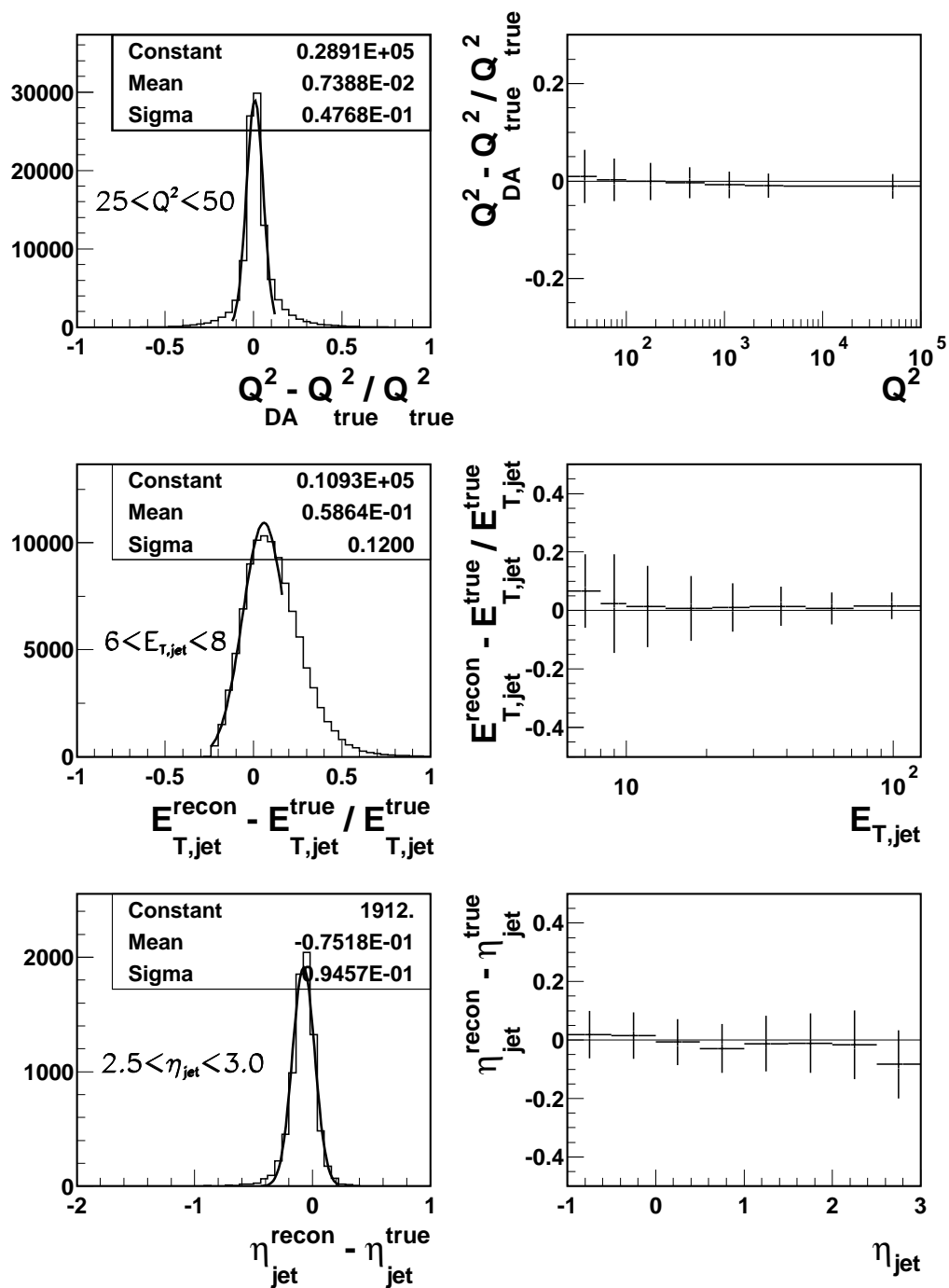


Figure 8.6: Resolutions for the event variable Q^2 and the jet variables $E_{T,jet}$ and η_{jet} . In the left column, a histogram of the resolution for the most critical bin is shown, with its associated Gaussian fit. In the right column, the resolution is plotted as a function of the variable.

The corrections are found to be $\sim 5\%$.

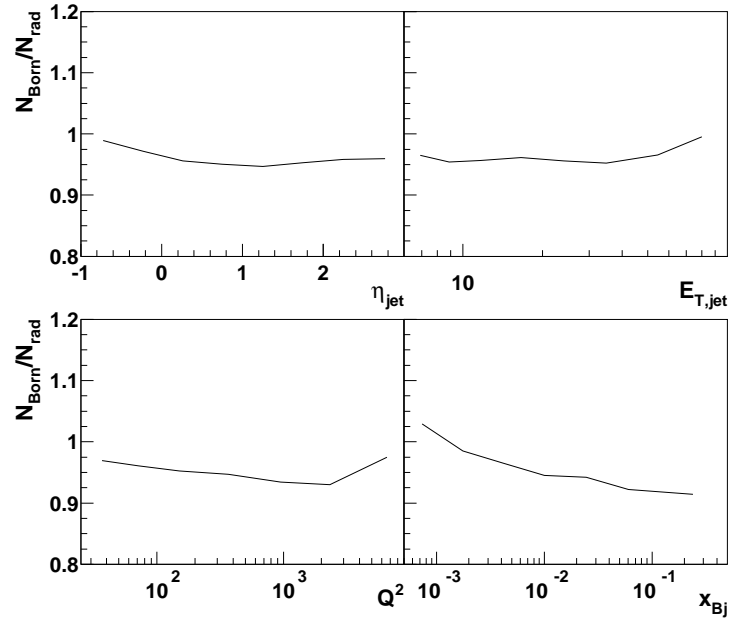


Figure 8.7: QED corrections for cross sections in the Inclusive Phase Space. The correction factor is applied to the data cross sections, and the cross section predictions from Ariadne and Lepto.

8.2 QPM Suppressed Phase Space Measurement

The disadvantage of jet finding in the laboratory frame is that the cross section is dominated by Quark-Parton Model (QPM) events, in which the gluon does not initiate the hard interaction. In order to suppress the contribution from these events, the phase space is restricted with the following conditions:

- The cosine of the hadronic angle must be less than zero.
- The pseudorapidity of the jet must be larger than zero.

In QPM events, there is by definition only one jet. Therefore, the hadronic angle is exactly aligned with the jet angle. By requiring the hadronic angle to be in a region exclusive of the region where the jet is required to be found, the QPM contribution to the sample effectively goes to zero at the true level.

8.2.1 Comparison of Data and Monte Carlo

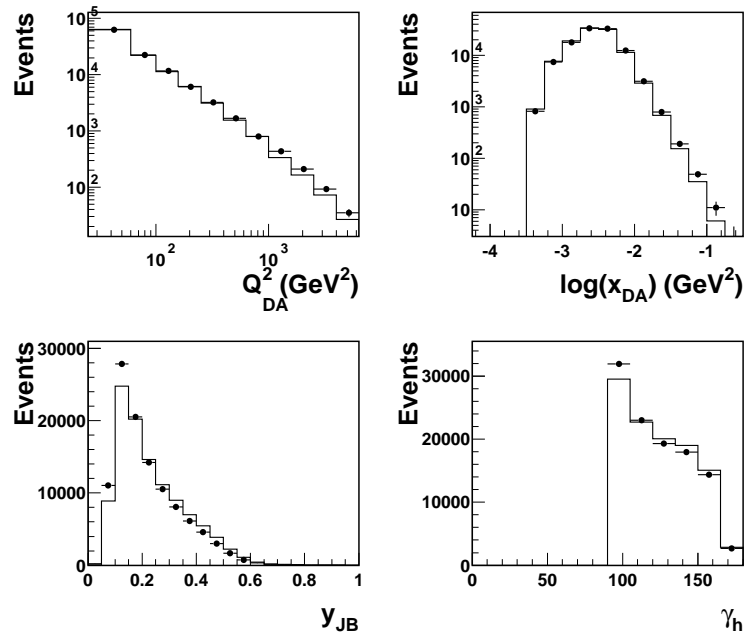


Figure 8.8: Comparison of data and MC for Q^2 , x , y and γ_h in the QPM Suppressed Phase Space

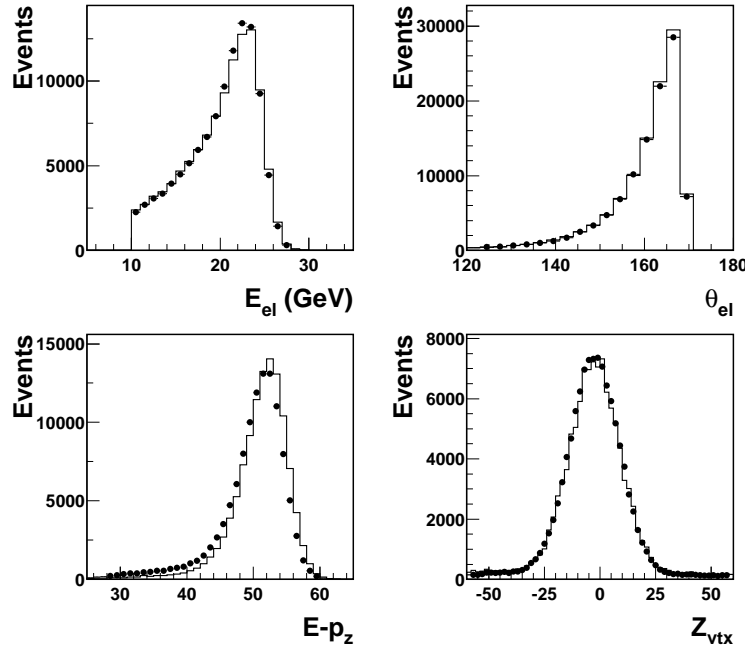


Figure 8.9: Comparison of data and MC for electron energy, electron angle, $E - p_z$ and z -vertex in the QPM Suppressed Phase Space

The comparison of event quantities for the QPM Suppressed phase space are shown in Figs. 8.8 and 8.9. The double-angle Q^2 and x are well-described, although the description in the hadronic variable y_{JB} and γ_h has deteriorated somewhat. All events with hadronic angle less than 90 degrees have been removed, and the shape in the remaining bins has changed as a result of the limited region in η for the jet. An additional systematic check is introduced to account for the variation in the cross section near the new cuts. The electron, $E - p_z$ and vertex distributions are described to the same level of accuracy as events in the inclusive phase space.

The jet description, shown in Fig. 8.10, has deteriorated somewhat at high values of jet transverse energy. The pseudorapidity distribution is now strongly peaked in the central region of the detector. This is due to the fact that the large contribution to forward going jets from QPM events (i.e. single jet events) are now removed and the multijet fraction is substantially enhanced. This indicates the signal BGF events we are interested in measuring are indeed enhanced.

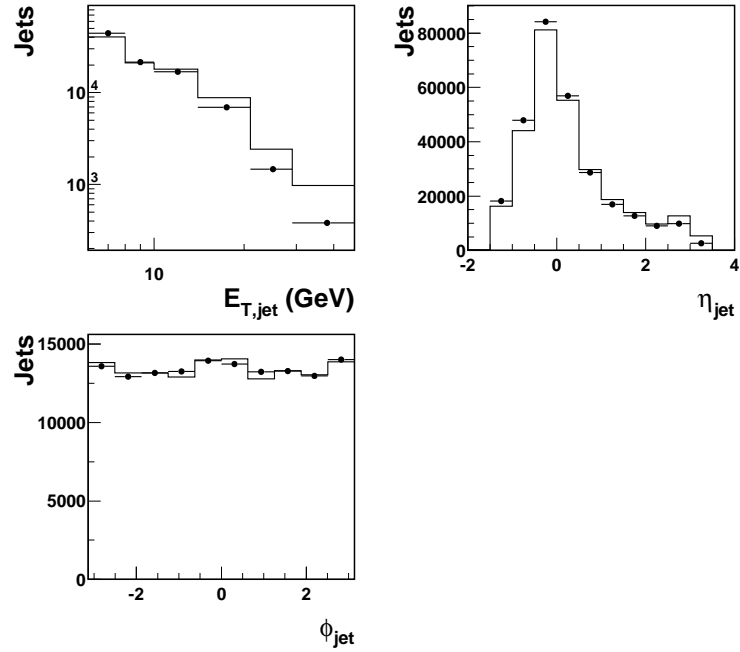


Figure 8.10: Comparison of data and MC for the jet variables transverse energy, pseudorapidity and azimuthal angle in the QPM Suppressed Phase Space

8.2.2 Purities, Efficiencies, Correction Factors

The purities, efficiencies and correction factors in the QPM Suppressed phase space are given in Figs. 8.11 and 8.12. The spectra are as described in the inclusive phase space, although the overall purity and efficiency have decreased slightly.

8.2.3 Resolutions

The resolution in all variables shown in Fig. 8.13 are similar to those found in the inclusive phase space.

8.2.4 ISR/FSR Corrections

The QED corrections applied to the data and MC cross sections in the QPM Suppressed Phase Space are shown in Fig. 8.14. As with the Inclusive Phase Space, the corrections are generally $\sim 5\%$.

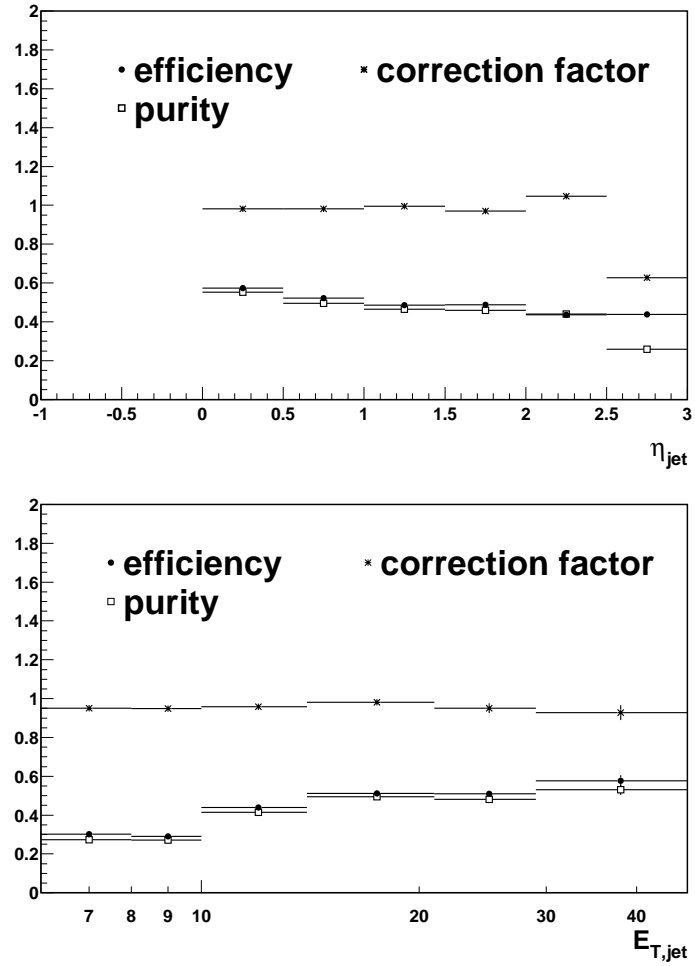


Figure 8.11: Efficiency and purity of the jet finding for jet variables pseudorapidity and transverse energy in the QPM Suppressed Phase Space, with the associated acceptance correction factor.

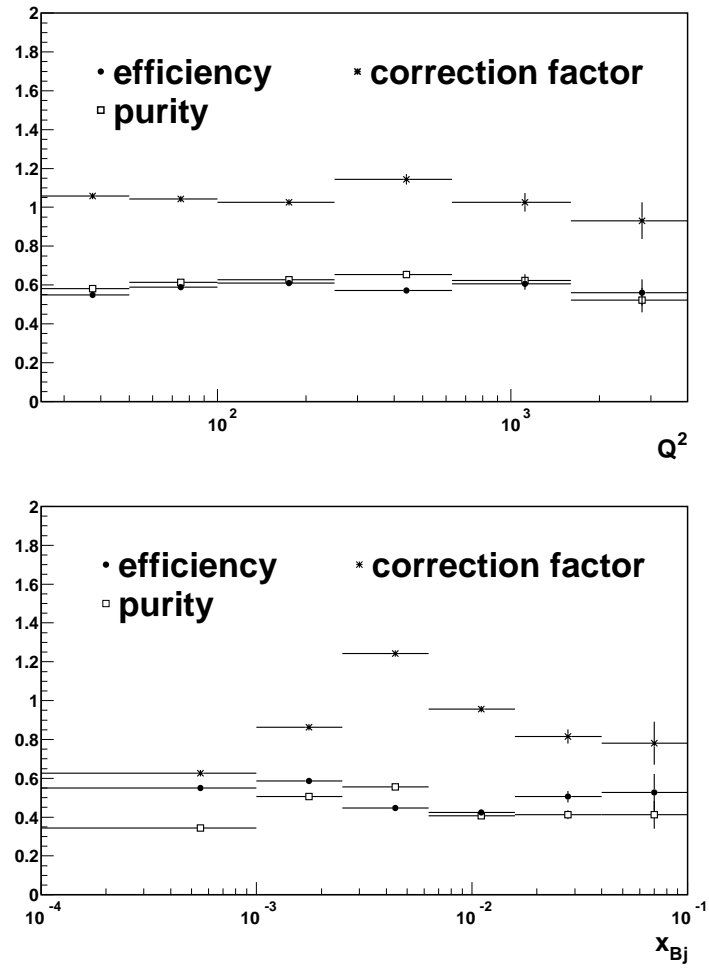
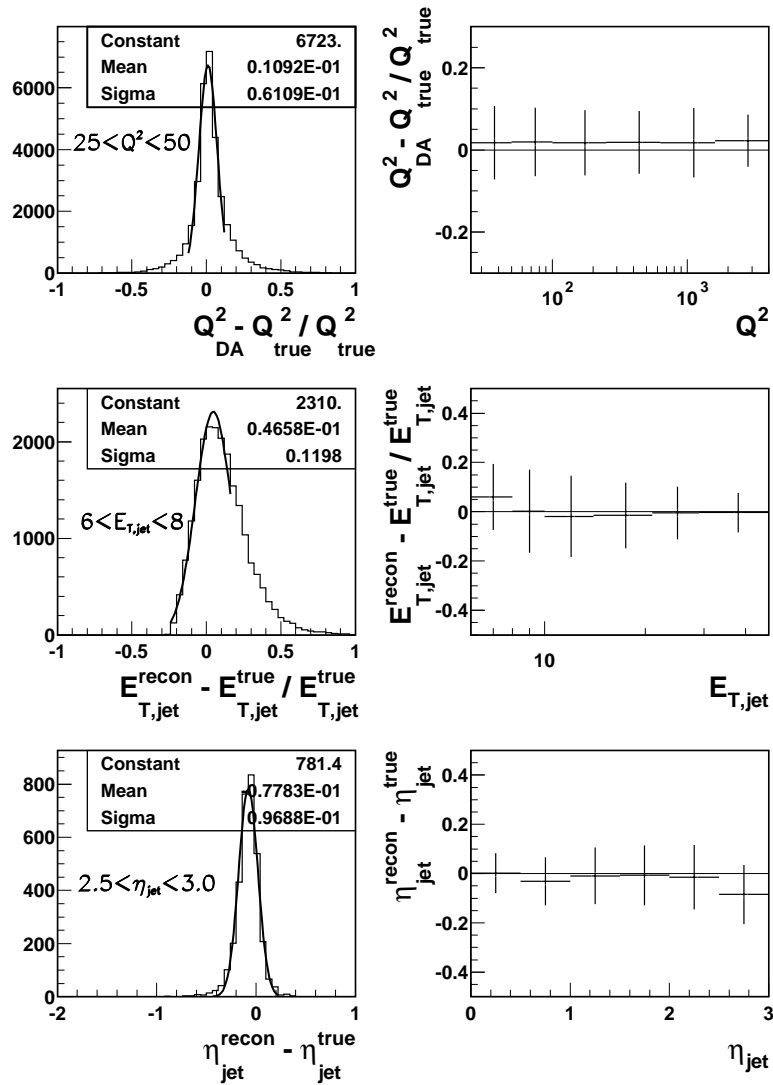


Figure 8.12: Efficiency and purity for events containing a forward jet in the QPM Suppressed Phase Space, with the associated acceptance correction factor.

Figure 8.13: Q^2 , $E_{T,jet}$, η_{jet} resolution for QPM Suppressed Phase Space

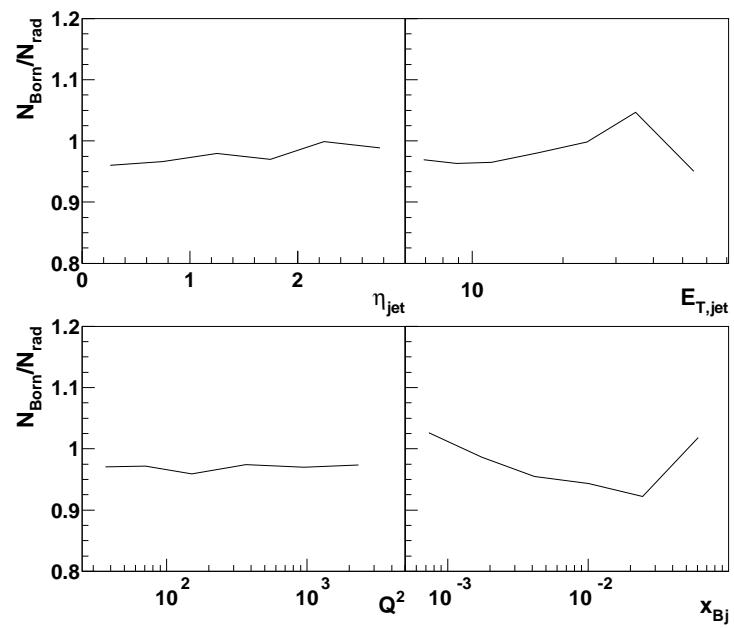


Figure 8.14: QED corrections for cross sections in the QPM Suppressed Phase Space

8.3 BFKL Forward Jet Measurement

The BFKL Forward Jet cross section, as postulated by Mueller and Navalet, attempts to measure events in which DGLAP evolution is suppressed. Because of the k_T ordering along the gluon ladder in DGLAP, it is possible to limit DGLAP evolution by requiring that the partons on the top and bottom of the ladder have comparable transverse energies. To that end, the following additional requirement is made:

- $0.5 < \frac{Q^2}{E_{T,jet}^2} < 2$. Because the transverse energy of the parton at the top of the ladder is determined by the Q^2 of the event, and the forward jet is closest to the proton remnant at the bottom of the ladder (at least as close to the bottom of the ladder as we can measure), this restriction on the ratio selects out events governed by DGLAP evolution.

8.3.1 Comparison of Data and Monte Carlo

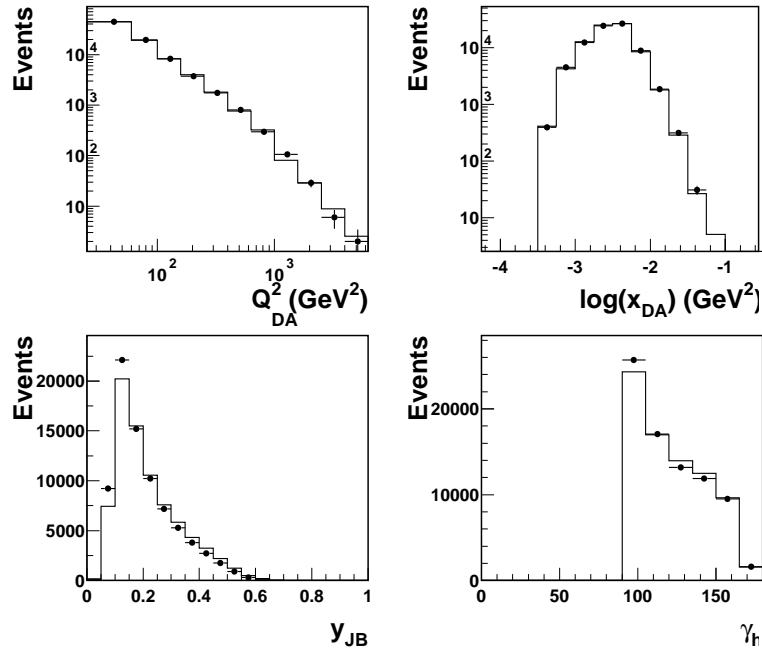


Figure 8.15: Comparison of data and MC for Q^2 , x , y and γ_h in the BFKL Phase Space

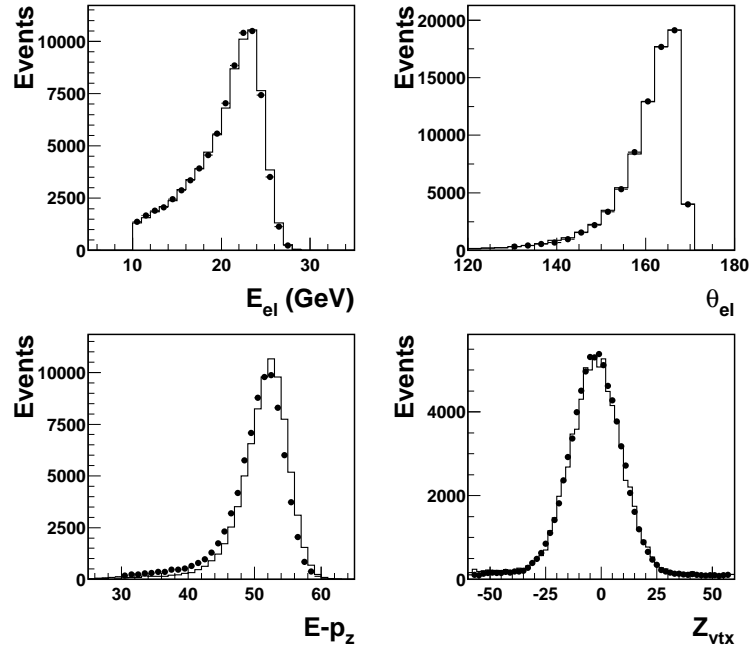


Figure 8.16: Comparison of data and MC for electron energy, electron angle, $E - p_z$ and z-vertex in the BFKL Phase Space

The comparison of data and MC for the BFKL forward jet phase space are given in Figs. 8.15 and 8.16. The kinematics are well-described, and the description of the hadronic variables are reasonable. The electron and event variables are described to the same level of accuracy as has been established in the more inclusive regions.

The description of all the jet variables is quite good. The Monte Carlo is relied upon for unfolding above η_{jet} of 0, but the low η bins are shown in order to see the behavior of the distribution around the cut value.

8.3.2 Purities, Efficiencies, Correction Factors

The efficiencies and purities for jet finding in the BFKL Phase Space is shown in Fig 8.18. They are comparable to the results found in the QPM Suppressed Phase Space. Similar comparability is seen in the event variables Q^2 and x_{Bj} shown in Fig. 8.19.

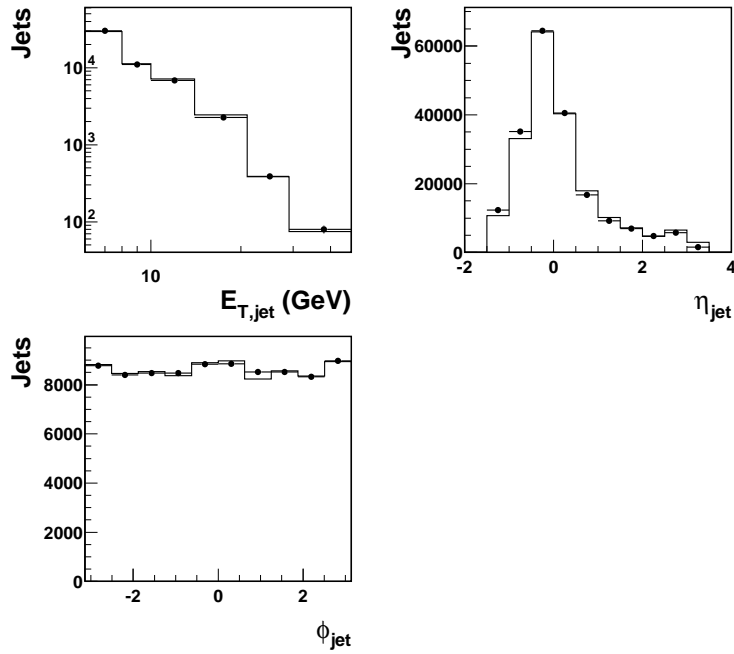


Figure 8.17: Comparison of data and MC for the jet variables transverse energy, pseudorapidity and azimuthal angle in the BFKL Phase Space

8.3.3 Resolutions

The resolutions of the variables Q^2 , $E_{T,jet}$ and η_{jet} are shown in Fig. 8.20. As in the other phase space measurements, the resolutions decrease slightly going from low to high Q^2 and $E_{T,jet}$ and going from high to low η_{jet} . All values are reasonable, which inspires confidence in the extrapolation of the cross sections.

8.3.4 ISR/FSR Corrections

The QED corrections applied to the data and MC cross sections in the BFKL Phase Space are shown in Fig. 8.21. As with the Inclusive and QPM Phase Spaces, the corrections are generally $\sim 5\%$.

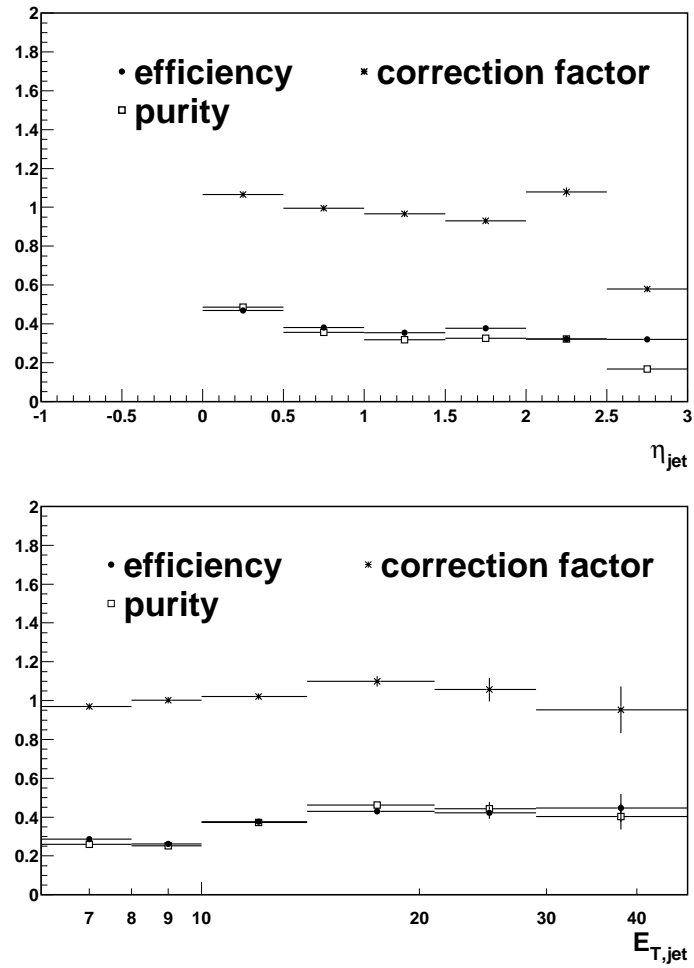


Figure 8.18: Efficiency and purity of the jet finding for jet variables pseudorapidity and transverse energy in the BFKL Phase Space, with the associated acceptance correction factor.

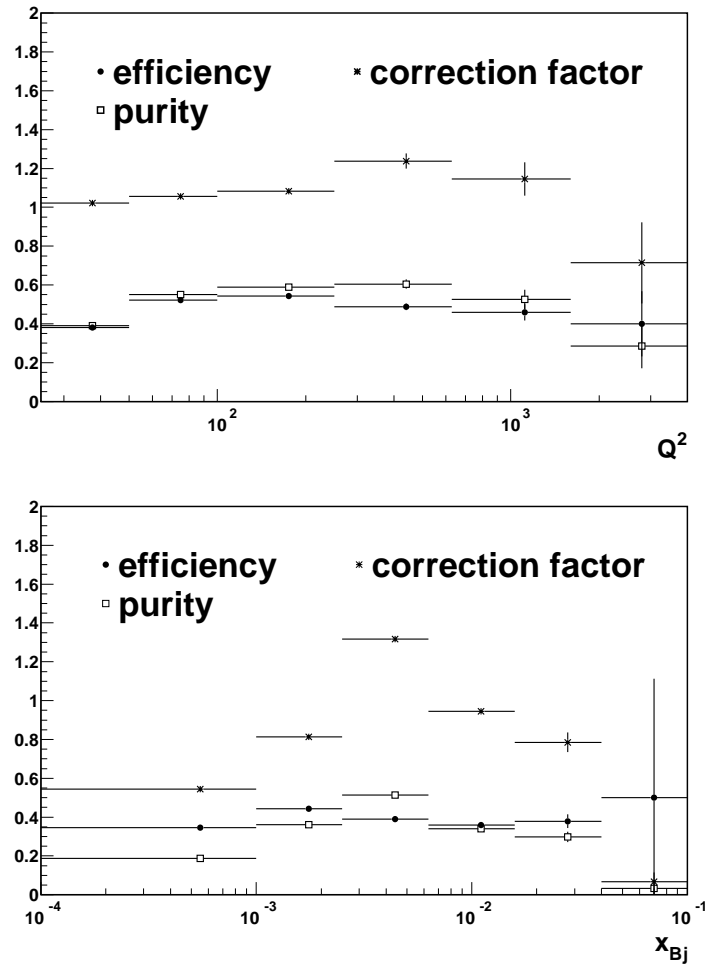
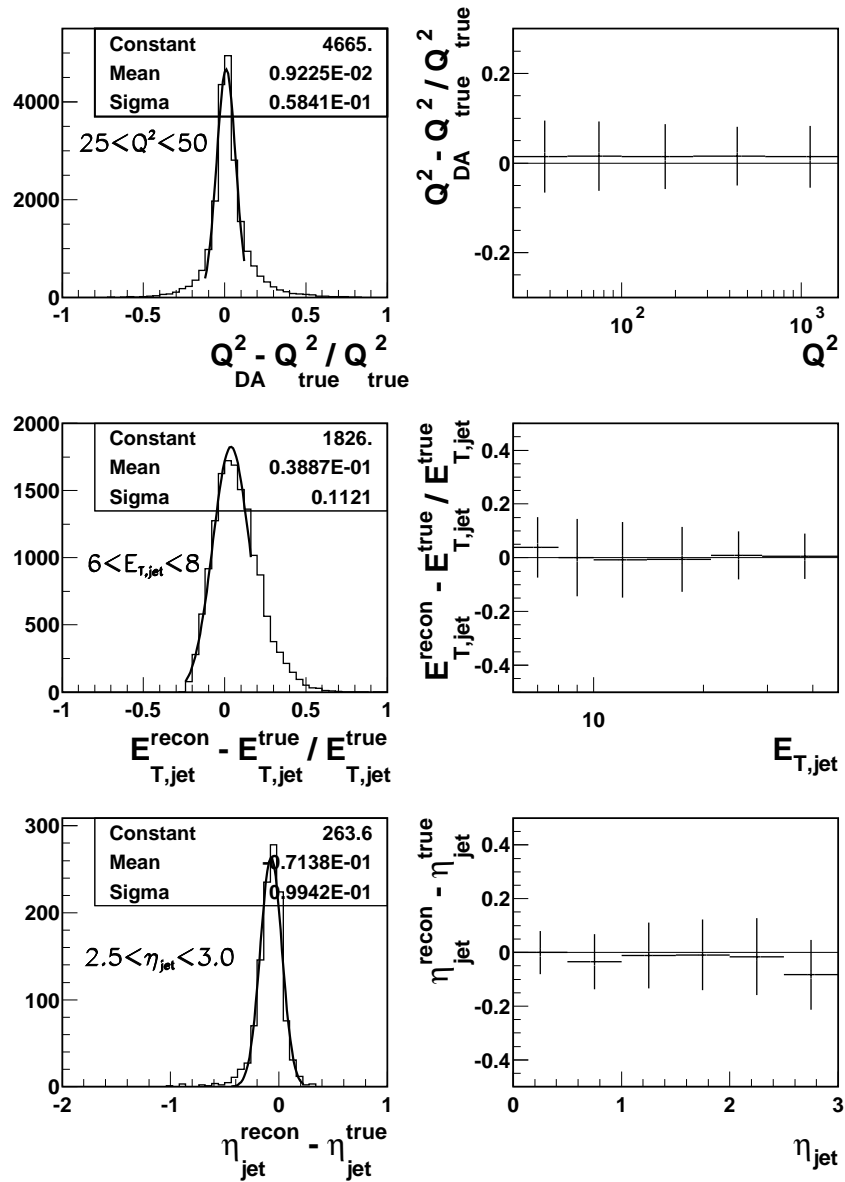


Figure 8.19: Efficiency and purity for events containing a forward jet in the BFKL Phase Space, with the associated acceptance correction factor.

Figure 8.20: $Q^2, E_{T,jet}, \eta_{jet}$ resolution for the BFKL Phase Space

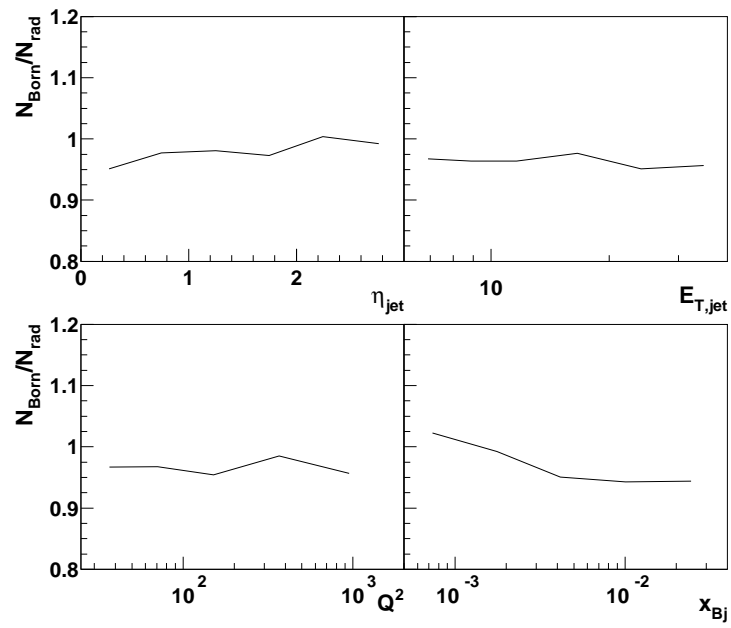


Figure 8.21: QED corrections for cross sections in the BFKL Phase Space

Chapter 9

Results

9.1 Measurement of the Inclusive Jet Cross Section

In this section, the results obtained from the measurement of the inclusive jet cross sections in the *inclusive* phase space are presented. The cross sections presented in jet variables, η_{jet} and $E_{T,jet}$, are measured once per jet, while the cross sections in event variables, Q^2 and x_{Bj} , are measured once per event. The bin boundaries chosen for each cross section are:

- $\eta_{jet} = -1, -0.5, 0, 0.5, 1, 1.5, 2, 2.5, 3$
- $E_{T,jet} = 6, 8, 10, 14, 21, 29, 47, 71, 90$
- $Q^2 = 25, 50, 100, 250, 630, 1600, 4000, 12000$
- $x_{Bj} = .0001, .001, .0025, .0063, .0158, .04, .1, 1$

Shown in Fig. 9.1 is the differential inclusive jet cross section in jet pseudorapidity. The cross section is suppressed in the forward region (high η_{jet}) due to the lower cut on y . The cross section is compared to leading order Monte Carlo predictions from Ariadne (CDM) and Lepto (MEPS) and the next-to-leading order predictions from the DISSENT (NLO) calculation. The data are best described by the Ariadne Monte Carlo. The Lepto Monte Carlo also gives a fair description of the data, although it gives generally a lower prediction. The DISSENT calculation can describe the data in the rear and central regions of the detector, but fails to describe the data in the forward region. This is shown explicitly in the middle plot of Fig. 9.1 where the ratio of the data cross section to

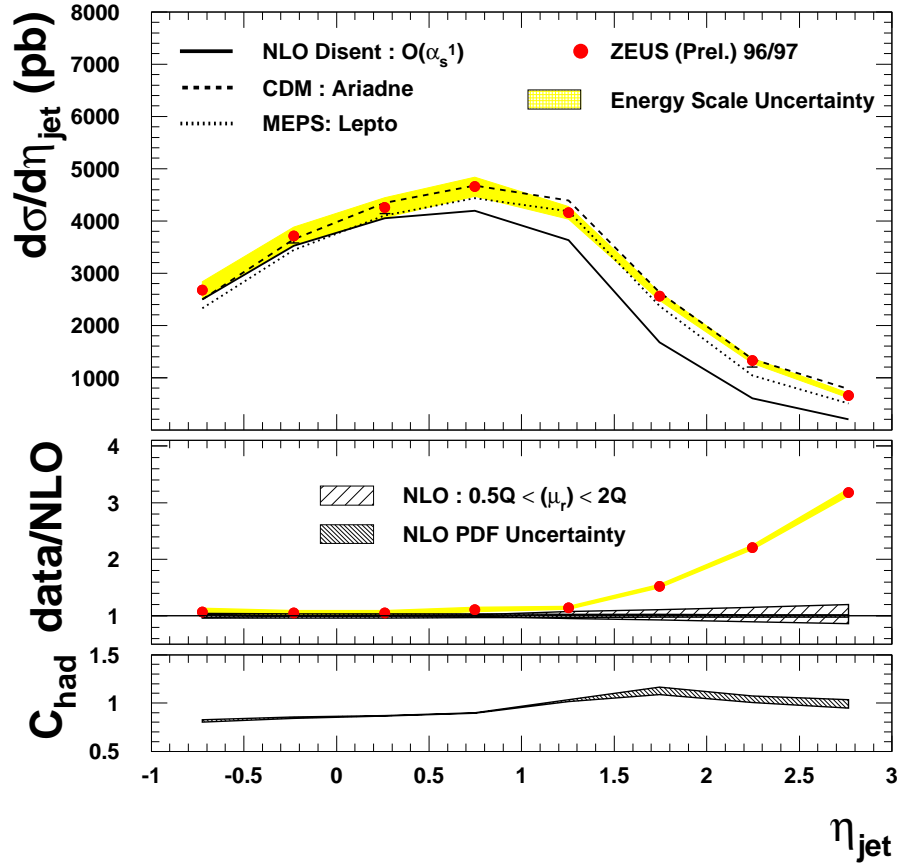


Figure 9.1: Inclusive jet cross section as a function of the jet pseudorapidity. The points represent the measured cross section, the inner bold-faced error bar represents the statistical error and the outer error bar represents the total systematic error. The shaded band represents the uncertainty of the measurement due to the calorimeter energy scale uncertainty for jets. The solid line represents the NLO prediction from DISENT, the dashed line the prediction from the LO CDM Monte Carlo, ARIADNE, and the dotted line the prediction from the LO MEPS Monte Carlo, LEPTO. The middle plot is the cross section divide by the DISENT prediction. The wide-hatched band represents the uncertainty in the theoretical prediction due to the choice of renormalization scale. The narrow-hatched band represents the uncertainty introduced by the PDF. The bottom plot shows the hadronization correction multiplied by the DISENT prediction to correct it for the lacking hadronization effects. The band represents the estimated uncertainty on the correction.

the DISENT prediction is plotted. DISENT underestimates the data by more than a factor of 3 in the highest η bin. This is a somewhat surprising result given that the cross section is dominated by quark-parton model events without QCD effects, and the LO matrix elements plus QED corrections for events of this sort are very well understood.

The uncertainty due to the renormalization scale uncertainty is shown in the middle plot of Fig. 9.1. The renormalization scale is set to Q^2 , which characterizes the hard pQCD scale in DIS. The uncertainty grows in the forward region, but never exceeds 20%. In the lower plot, the hadronization correction calculated with Ariadne is shown, which is applied to the DISENT calculation to make it comparable with the data.

Some feature of the DISENT calculation should be emphasized. Because the cross section is dominated by quark-parton model events which, at leading order, has no gluonic component, the leading order contribution is defined to be $\mathcal{O}(\alpha_s^0)$. This means the DISENT prediction for the cross section is generated considering only Feynman diagrams that are $\mathcal{O}(\alpha_s^1)$. These diagrams are either quark-parton model events with one gluon radiation (equivalent to the QCD-Compton process) or tree-level Boson-Gluon Fusion events. Therefore, gluonic radiation occurring in BGF or QCD-Compton events are not accounted for.

The LO Monte Carlo programs attempt to include the contribution from higher-order gluonic emissions through their parton showering models, by providing a good match to the data. One possible explanation for the discrepancy between the data and DISENT calculation is the lack of extra parton emissions in the calculation. One would expect that the uncertainty due to the renormalization scale would give an estimation of parton emission effects, since the variation in the renormalization scale indicates the sensitivity to higher order effects. However, the NLO calculation at $\mathcal{O}(\alpha_s^1)$ may not cover sufficient terms in the perturbative expansion to characterize the data.

The uncertainty introduced by the parton density functions is shown in Fig. 9.1 as a narrow hatched band. This uncertainty never changes the DISENT prediction by more than 4%.

The differential inclusive jet cross section is shown as a function of $E_{T,jet}$ in Fig. 9.2. Again, the LO Monte Carlo models, and especially Ariadne, can describe the cross section over nearly five orders of magnitude. The DISENT calculation describes the data at high transverse energies, but

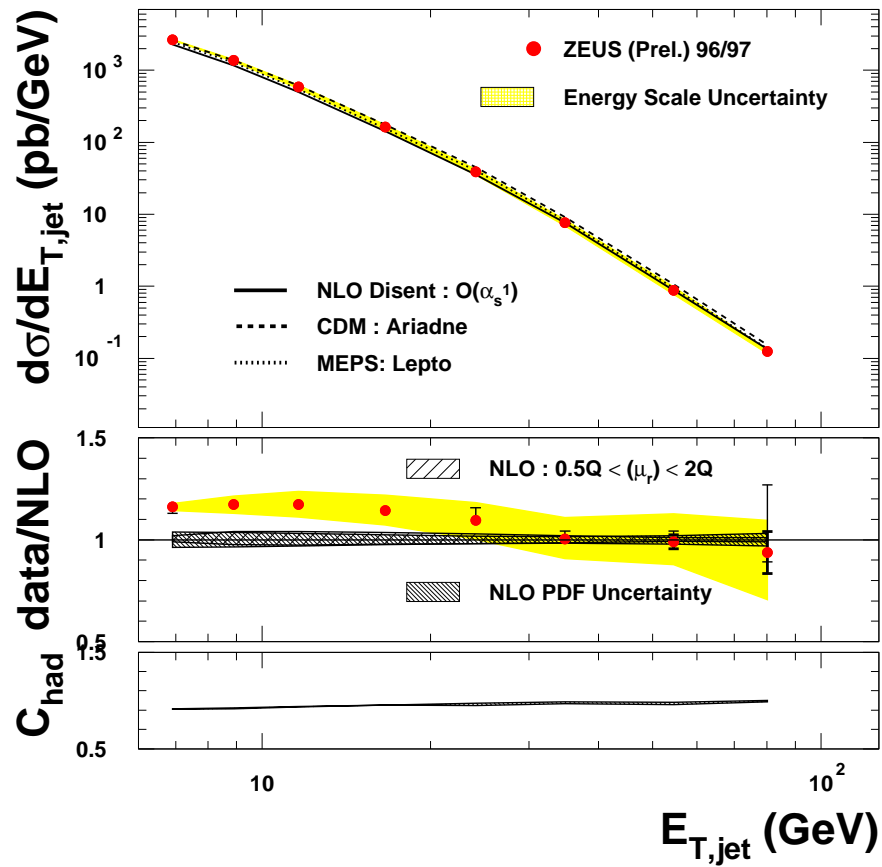


Figure 9.2: Inclusive jet cross section as a function of the jet transverse energy. All other details are as in Fig. 9.1

underestimates the data by about 15% in the low E_T bins. For $E_{T,jet}$, the uncertainties due to the renormalization scale and PDF are around 5%.

The differential cross section in Q^2 and Bjorken x for events containing at least one jet are shown in Figs. 9.3 and 9.4, respectively. The cross section in Q^2 is generally well-described by the DISSENT calculation, although it underestimates the data slightly in the lowest Q^2 bin.

The cross section in Bjorken x turns over at low values of x_{Bj} due to the lower cut on Q^2 and the constraint placed on x_{Bj} by the value of Q^2 in HERA kinematics. A sizeable disagreement is seen between the data and DISSENT in the lowest region of Bjorken x . This is the region in which the DGLAP scheme for parton evolution is not expected to be applicable. However, no such disagreement has been seen in the inclusive (structure function) analyses which have made measurements down to values of $6 \cdot 10^{-5}$ in x_{Bj} (see Fig. 2.5). In order to understand the event overlap between the total neutral current DIS cross section, and that from the subsample which includes a hard jet, the DISSENT predictions for each cross section as a function of the variables Q^2 and x_{Bj} is shown in Fig. 9.5. At high Bjorken x and Q^2 , the inclusive cross section is dominated by events containing a jet, but at low Q^2 and x_{Bj} , the fraction of DIS events containing a jet is small. Therefore, the discrepancy between the data cross sections and DISSENT calculations for the inclusive jet cross sections is not incompatible with agreement in the low x_{Bj} and Q^2 regions between DISSENT predictions and the total inclusive cross section measurements.

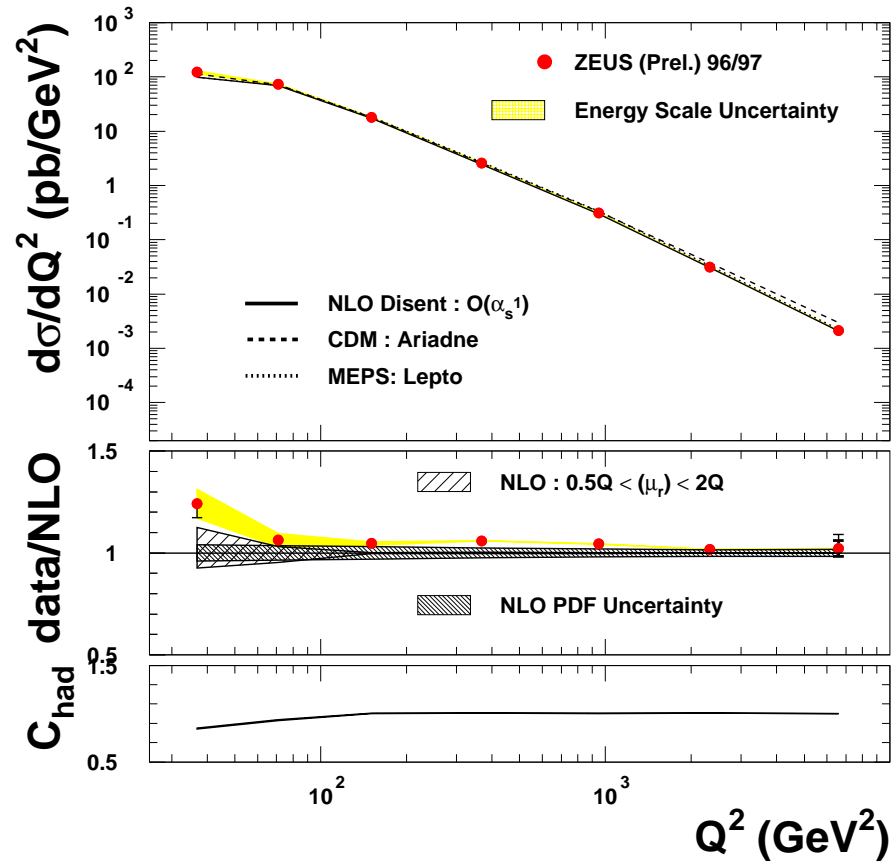


Figure 9.3: Inclusive jet cross section as a function of Q^2 . All other details are as in Fig. 9.1

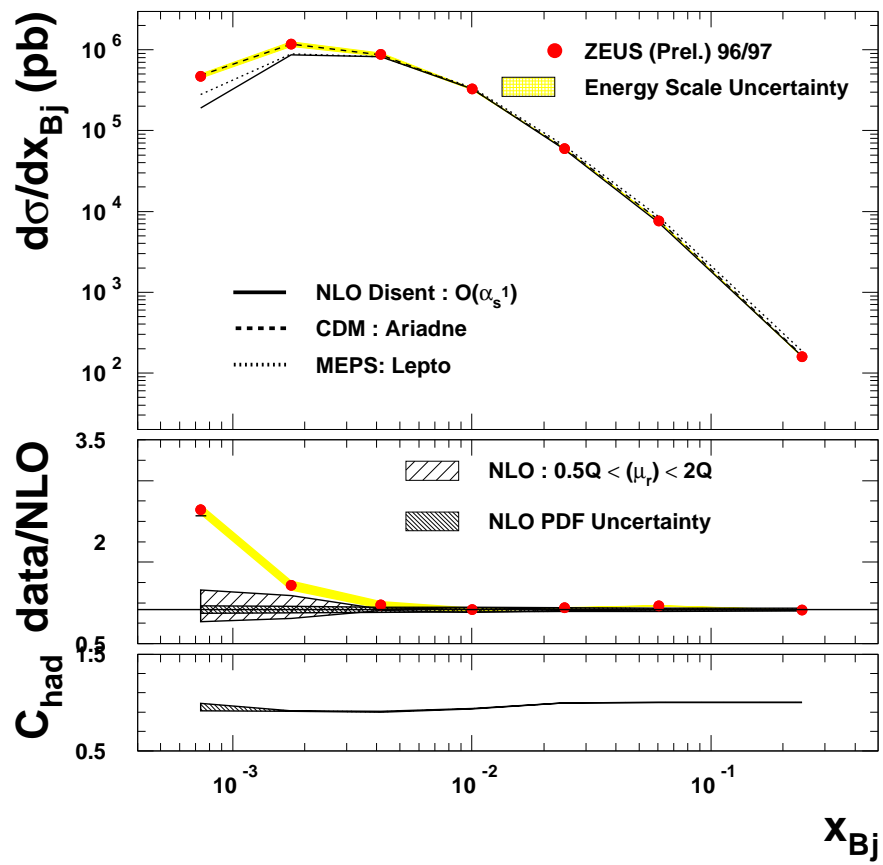


Figure 9.4: Inclusive jet cross section in the variable x_{Bj} . All other details are as in Fig. 9.1

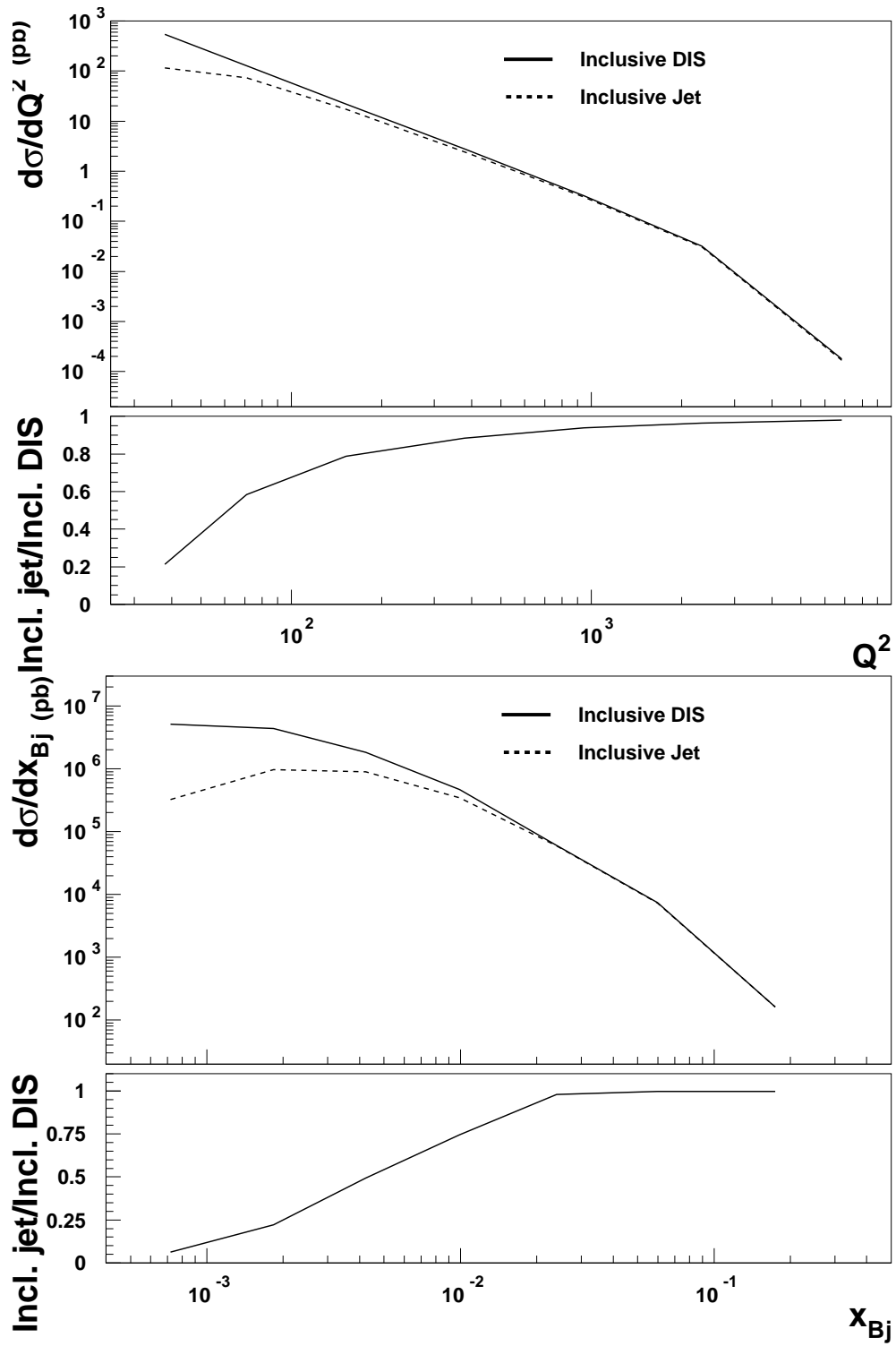


Figure 9.5: The total inclusive DIS cross section and the inclusive jet cross section, and their ratios, as a function of the variables Q^2 (top) and x_{Bj} (bottom) as predicted by the DISENT program.

9.2 Measurement of the Inclusive Jet Cross Section in the QPM Suppressed Phase Space

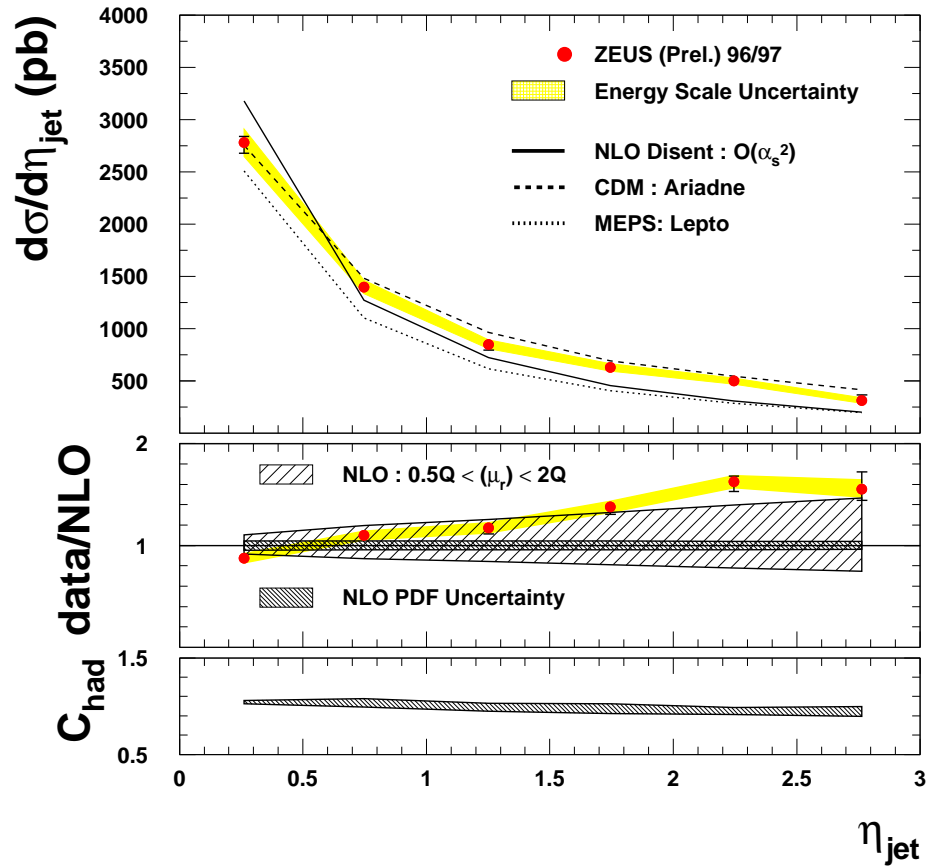


Figure 9.6: Inclusive jet cross section as a function of the jet pseudorapidity in the QPM suppressed phase space. All other details are as in Fig. 9.1

In order to further investigate the discrepancy between the NLO calculations and the data, we examine a phase space with a higher purity of Boson-Gluon Fusion events. This is done by measuring the cross sections with the requirement that the hadronic angle be in the central or rear part of the

detector and the jet be in the forward part of the detector ¹. These requirements strongly suppress the contribution from QPM events. For that reason, the order of α_s in the DISENT calculation is redefined. Since the leading order diagrams contributing to the measured cross section are from BGF and QCD-Compton diagrams, the LO DISENT calculation is made at $\mathcal{O}(\alpha_s^1)$ and NLO at $\mathcal{O}(\alpha_s^2)$. In Fig. 9.6, the differential inclusive jet cross section in the “QPM Suppressed” Phase Space in η_{jet} is shown. The measured cross section is now described by the DISENT calculation, within the increased experimental and theoretical errors. The renormalization scale uncertainty has increased dramatically over that found in the inclusive phase space, particularly in the forward region where it is 40%. The PDF uncertainty is small, around 5%. Although the relative difference between the data and the DISENT prediction has decreased substantially with respect to the cross section in the Inclusive phase space, the large increase in the renormalization scale uncertainty makes quantifying the level of agreement in the QPM Suppressed cross section difficult.

The differential inclusive jet cross section in $E_{T,jet}$ is shown in Fig. 9.7. The measured result is very well described by the DISENT calculation. The bold inner error bars represent the statistical error on the measurement. The outer thinner error bars represent the total systematic error.

Shown in Fig. 9.8 and 9.9 are the differential cross sections for events containing at least one jet in Q^2 and x_{Bj} , respectively. Again, the data are well described by the DISENT calculation. The renormalization scale uncertainty is large, particularly at low x_{Bj} .

¹The reader is reminded that in Boson-Gluon Fusion events, the hadronic angle is not necessarily aligned with a jet. Indeed, as the tree-level BGF diagram gives rise to two final state partons, two jets are expected in the event sample.

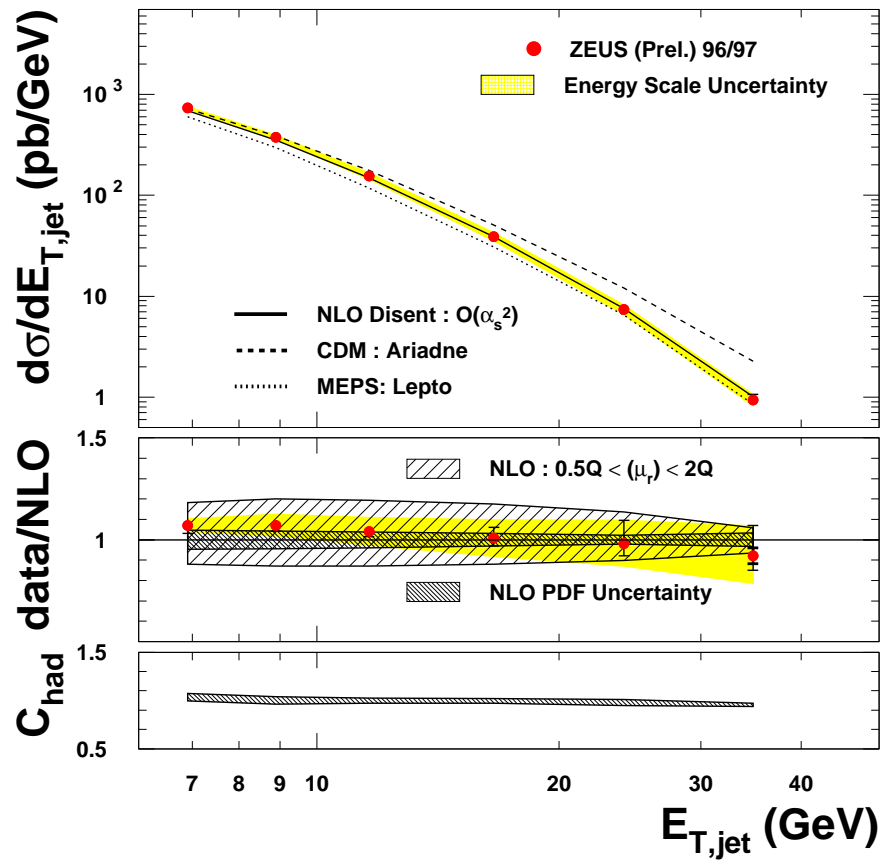


Figure 9.7: Inclusive jet cross section as a function of the jet transverse energy in the QPM suppressed phase space. All other details are as in Fig. 9.1

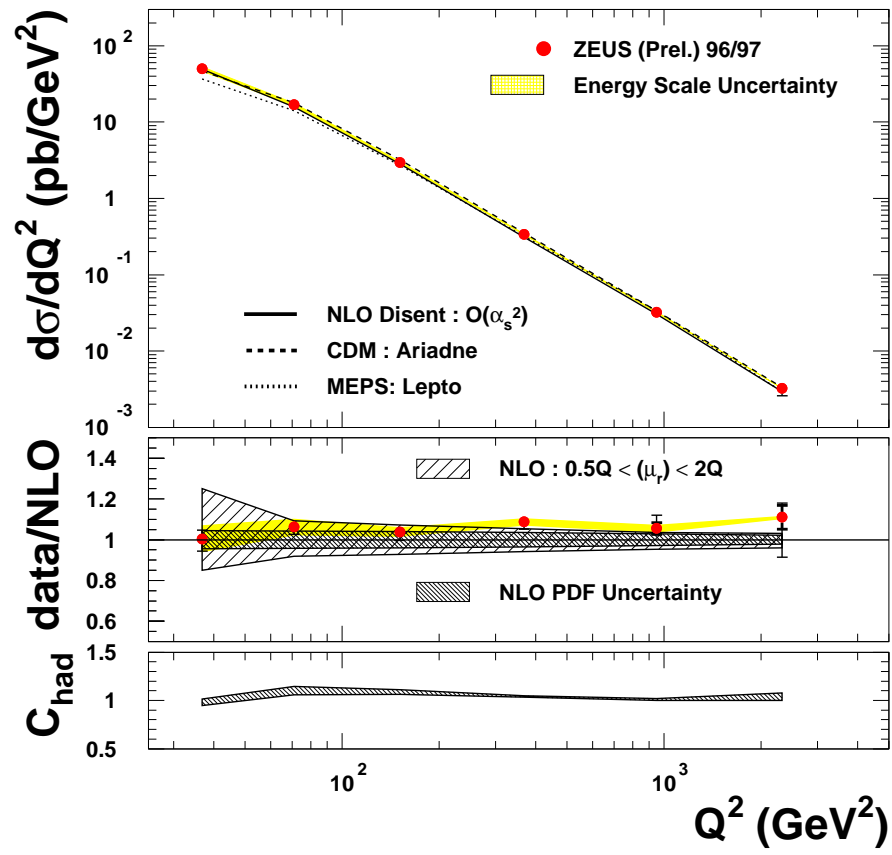


Figure 9.8: Inclusive jet cross section as a function of Q^2 in the QPM suppressed phase space. All other details are as in Fig. 9.1

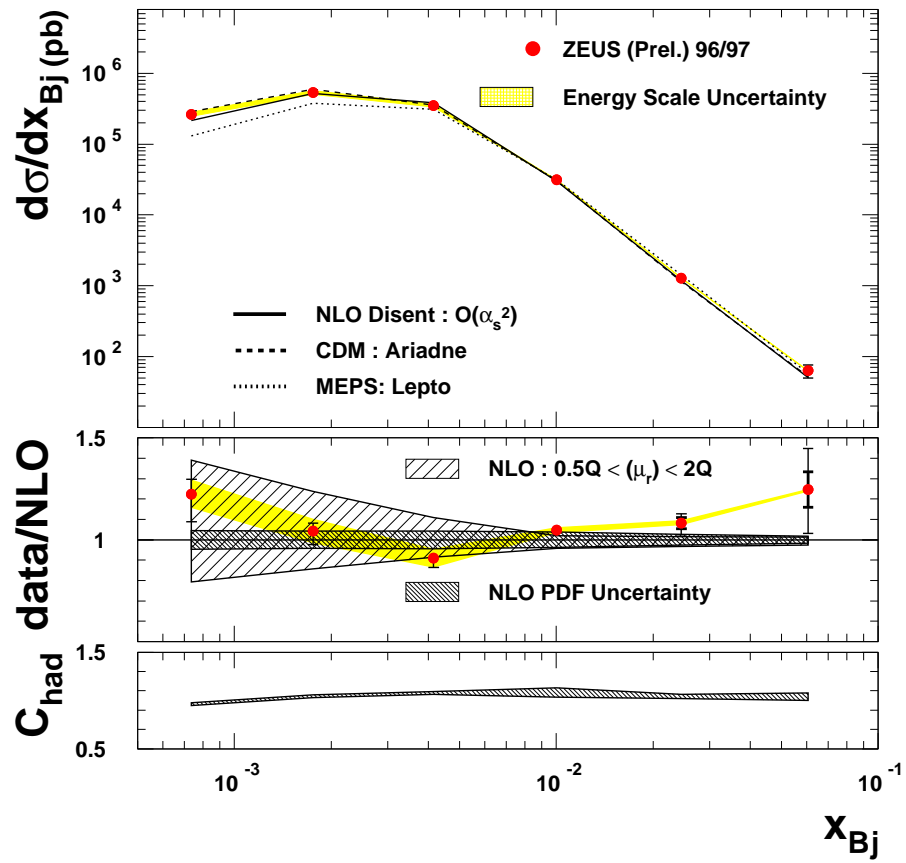


Figure 9.9: Inclusive jet cross section as a function of x_{Bj} in the QPM suppressed phase space. All other details are as in Fig. 9.1

9.3 BFKL Forward Jet Cross Section

We perform an additional measurement of the forward jet cross section with the new requirement that the transverse energy of the jet be comparable with Q^2 , $\frac{1}{2} < \frac{E_{T,jet}^2}{Q^2} < 2$. This requirement limits the evolution of the partons along the gluon ladder in Q^2 , thereby enhancing the fraction of events that could exhibit BFKL evolution [19, 20].

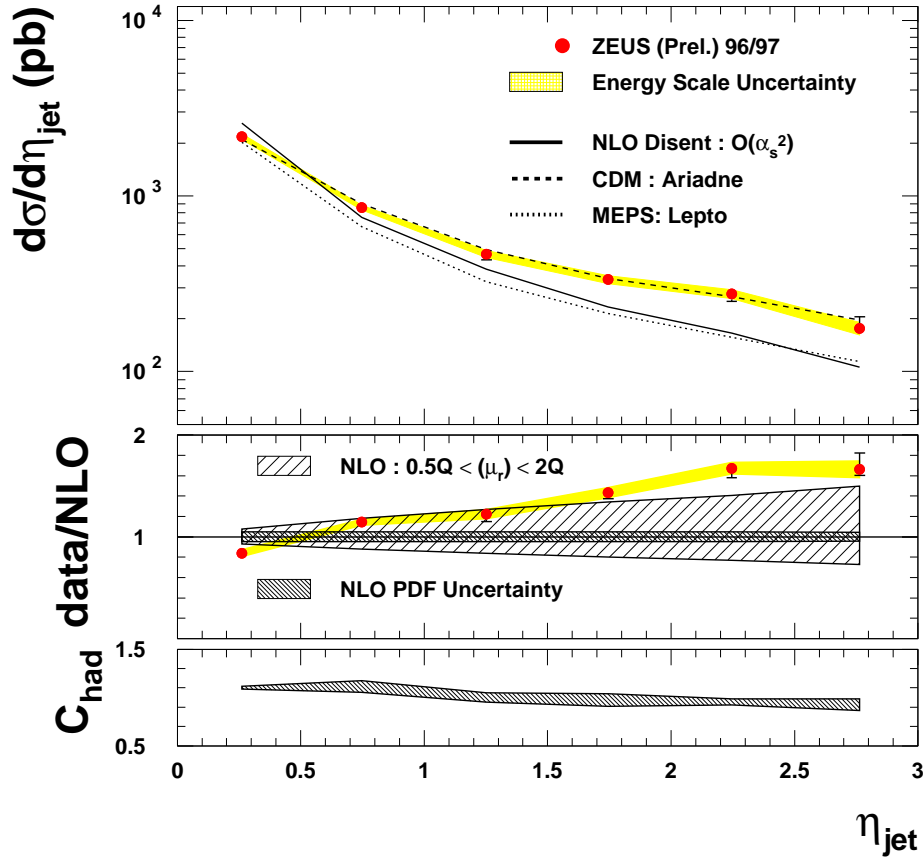


Figure 9.10: Inclusive jet cross section as a function of the jet pseudorapidity in the BFKL phase space. All other details are as in Fig. 9.1

The differential inclusive jet cross section is shown in η_{jet} in Fig. 9.10. The NLO calculation as computed with DGLAP can describe the data fairly well, although the agreement deteriorates somewhat in the most forward region. Ariadne does an excellent job of describing the data. The uncertainty due to the hadronization model chosen increases in this phase space with respect to the previous two. This is expected as the Color-Dipole Model for parton showering mimics BFKL dynamics in the way it distributes the transverse energy of the event among its partons. Lepto has the same transverse energy ordering among the partons as in DGLAP.

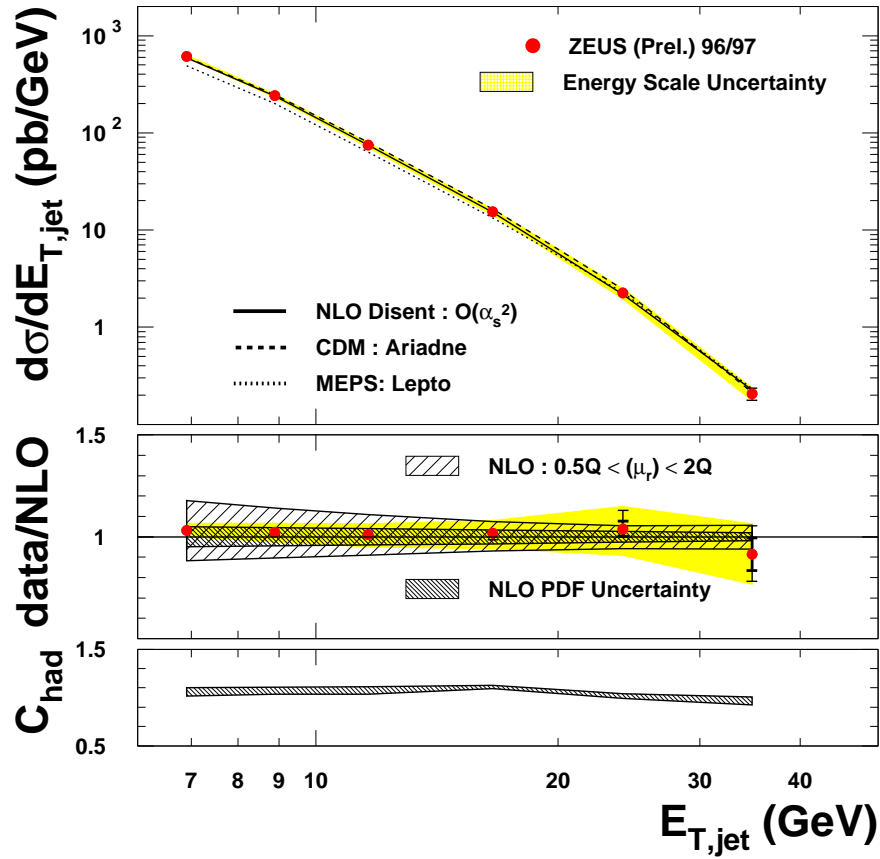


Figure 9.11: Inclusive jet cross section as a function of the jet transverse energy in the BFKL phase space. All other details are as in Fig. 9.1

The differential inclusive jet cross section in $E_{T,jet}$ and the differential cross sections for events with at least one jet in Q^2 , x_{Bj} are shown in Figs. 9.11,9.12 and 9.13. The DISENT calculation describes the data for all these measurements.

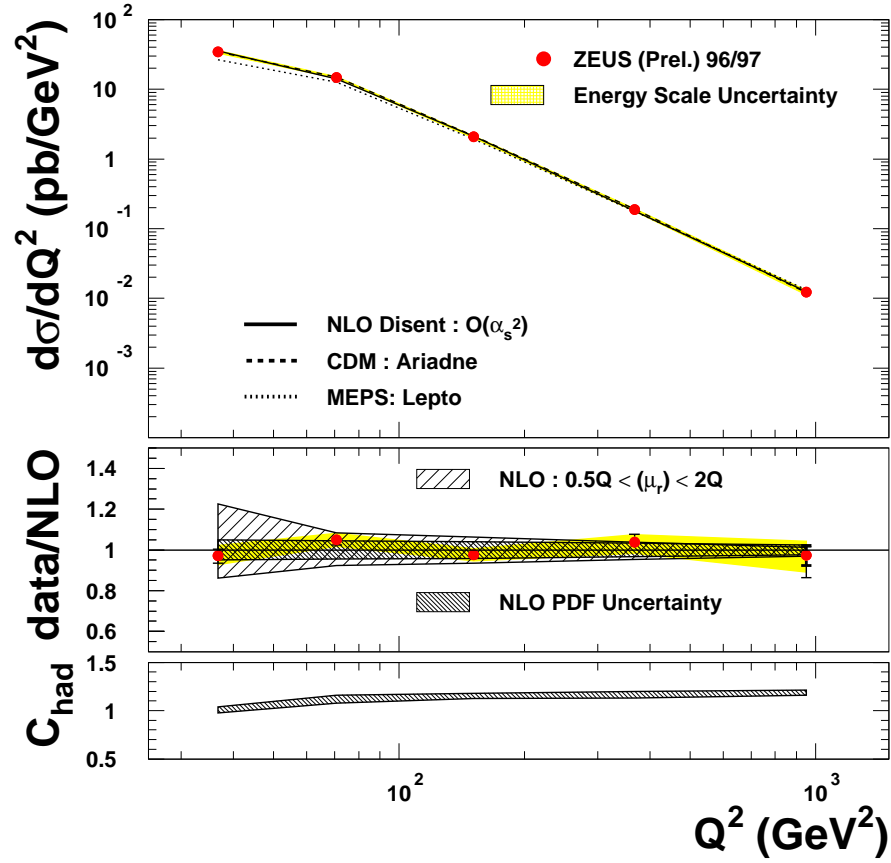


Figure 9.12: Inclusive jet cross section as a function of Q^2 in the BFKL phase space. All other details are as in Fig. 9.1

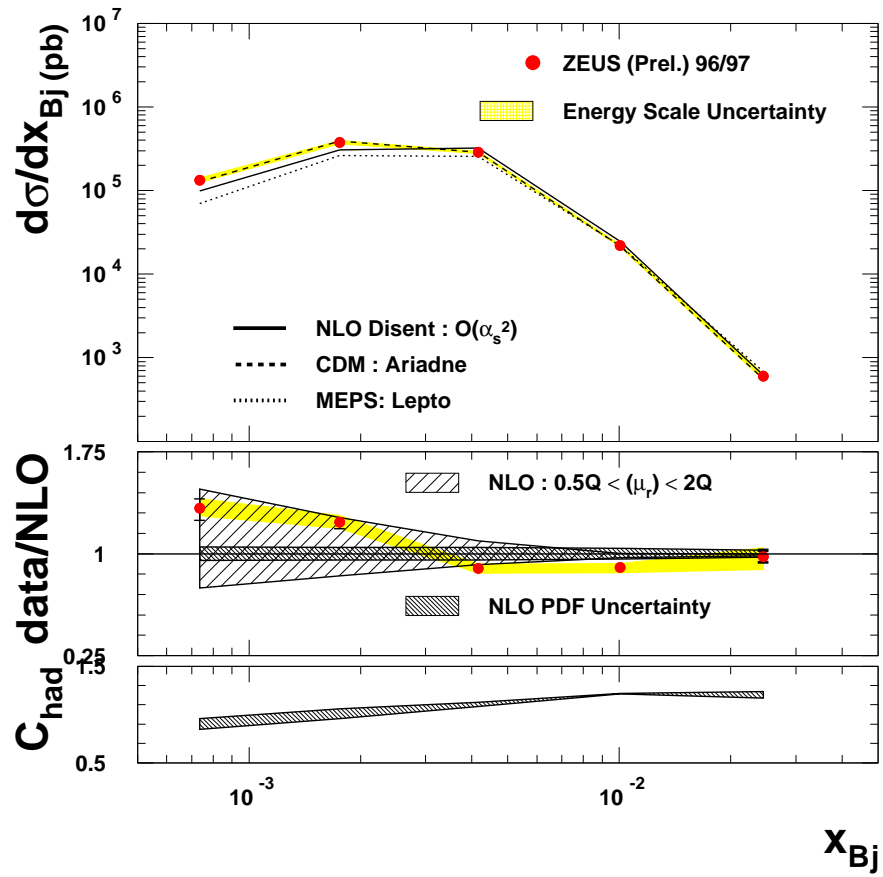


Figure 9.13: Inclusive jet cross section as a function of x_{Bj} in the BFKL phase space. All other details are as in Fig. 9.1

9.4 Systematic Uncertainties

An analysis of the systematic uncertainties in these measurements was performed. These uncertainties arise from, among other effects, the resolution of measured quantities, such as the calorimeter energies. The calorimeter energy scale uncertainty was studied for single-jet events and is described in [62]. The calorimeter energy scale uncertainty was found to be within $\pm 3\%$ in all three detectors (FCAL, RCAL and BCAL). The effect of this uncertainty on the measured cross section is estimated by varying the jet transverse energies in the data up and down by 3% before applying the jet cuts and measuring the resultant cross section. This variation results in a typical uncertainty on the measured cross sections of 5-10%. The uncertainty due to the calorimeter energy measurement is the largest experimental uncertainty. The cross section is highly sensitive to the energy measurement at the cut boundary because the jet transverse energy spectrum is steeply falling. A small shift in transverse energy results in a large fraction of events migrating across the cut boundary.

A systematic uncertainty is introduced by every cut made in the measurement due to the reliance on the Monte Carlo description of the data distributions. If the shape of the Monte Carlo distributions could describe the data perfectly at the cut boundary, the systematic uncertainty on the choice of cut would be zero. This is not the case, since the Monte Carlo relies on imperfect models of the physics processes and detector effects. Therefore, the cuts used in this analysis are varied by one sigma in the resolution (at the cut boundary) of the variable in consideration. The systematic uncertainty introduced by each cut is determined by varying the specific cut while keeping all other cuts at their nominal value in data and detector level Monte Carlo. The difference in the resulting cross section from the nominal one is the systematic uncertainty. The cuts that are investigated are:

- $E_{T,jet} \text{ cut } \pm 1 \text{ GeV}$
- $upper \ \eta_{jet} \text{ cut } \pm 0.2$
- $E_{electron} \text{ cut } \pm 1 \text{ GeV}$
- $Q^2 \text{ cut } \pm 3 \text{ GeV}^2$

- Z_{vtx} cut ± 10 cm.
- low $E - p_z$ cut ± 3 GeV
- high $E - p_z$ cut ± 3 GeV
- $\cos\gamma_h$ cut ± 0.1

Systematic uncertainty is also introduced by the physics model dependencies of the Monte Carlo programs used for unfolding the cross sections. To estimate the magnitude of this uncertainty, the LEPTO MC sample is used to correct the data instead of ARIADNE. The difference in the corrected cross sections is taken to be the absolute value of systematic uncertainty.

The effect of these systematic variations on all cross sections in the Inclusive Phase Space are shown in Figs. 9.14 and 9.15. The largest systematic uncertainty is due to the uncertainty in the energy scale, which averages about 5%, but can reach values as high as 20% in bins with low statistics, where bin migrations of just a few events can change the cross section dramatically. The second largest contribution to the systematic error arises from using Lepto instead of Ariadne to correct the data, but is still generally within 5%. All other uncertainties are generally on the order of 1-2% and never more than 5% of the measured cross section.

The effect of the systematic variations on all cross sections in the QPM Suppressed Phase Space are shown in Figs. 9.16 and 9.17. Again, the systematic uncertainty introduced by the calorimeter energy scale and the model dependence on the Monte Carlo for correcting the data are dominant. A systematic uncertainty due to the hadronic angle cut is included for the measurement in the QPM Suppressed Phase Space. The variation in the hadronic angle cut chosen can induce an uncertainty as large as 15% in low statistics bins, but is generally less than 5%. Some large systematic uncertainties are present, for instance the uncertainty introduced in the cross section in the highest bin of η_{jet} due to a variation of the jet transverse energy cut. However, most uncertainties are still within 5% of the measured cross section, except in bins with low statistics.

The effect of the systematic variations on all cross sections in the BFKL Phase Space are shown in Figs. 9.18 and 9.19. The behavior of the systematic uncertainties are similar to those found in the QPM Suppressed Phase Space, but are smaller percentages of the measured cross section.

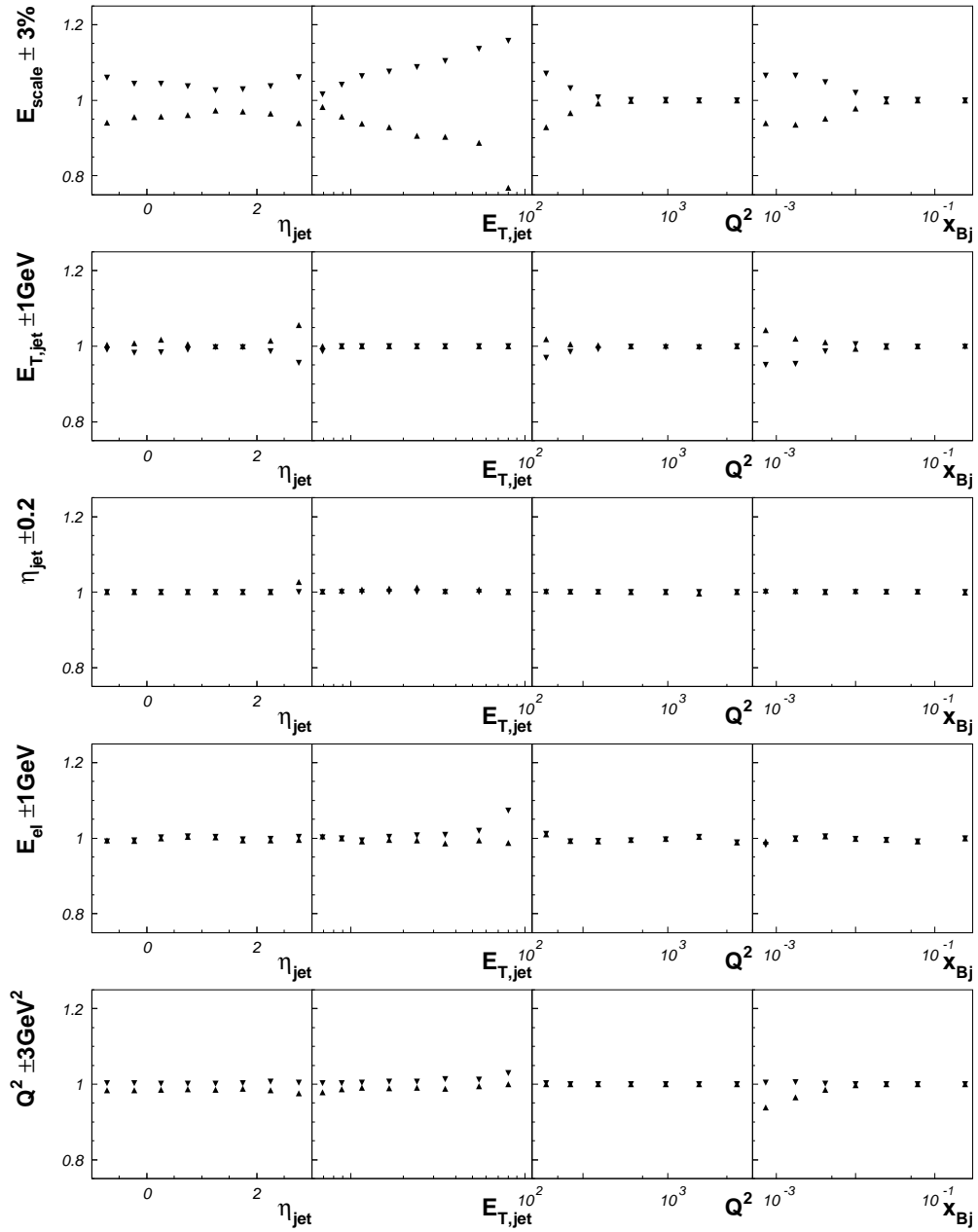


Figure 9.14: Systematic uncertainties for cross sections in the Inclusive Phase Space.

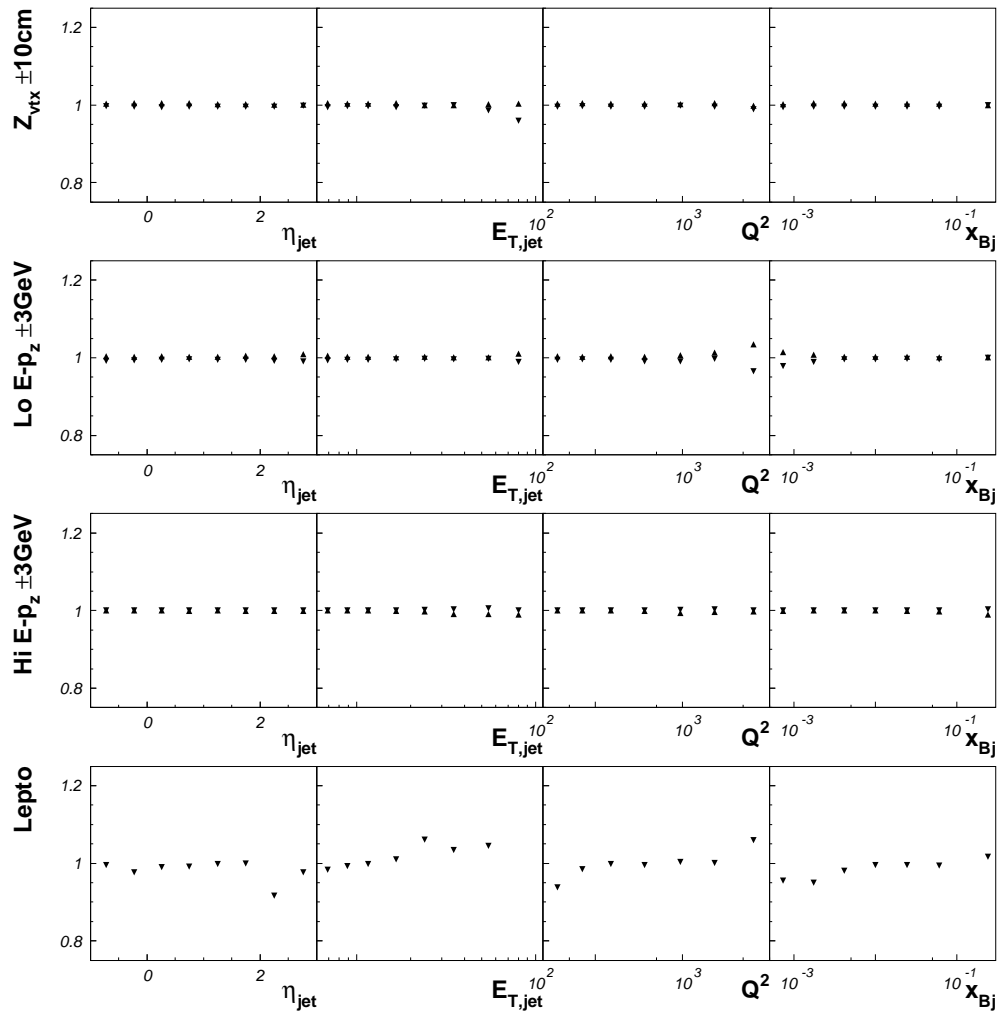


Figure 9.15: Systematic uncertainties for cross sections in the Inclusive Phase Space.

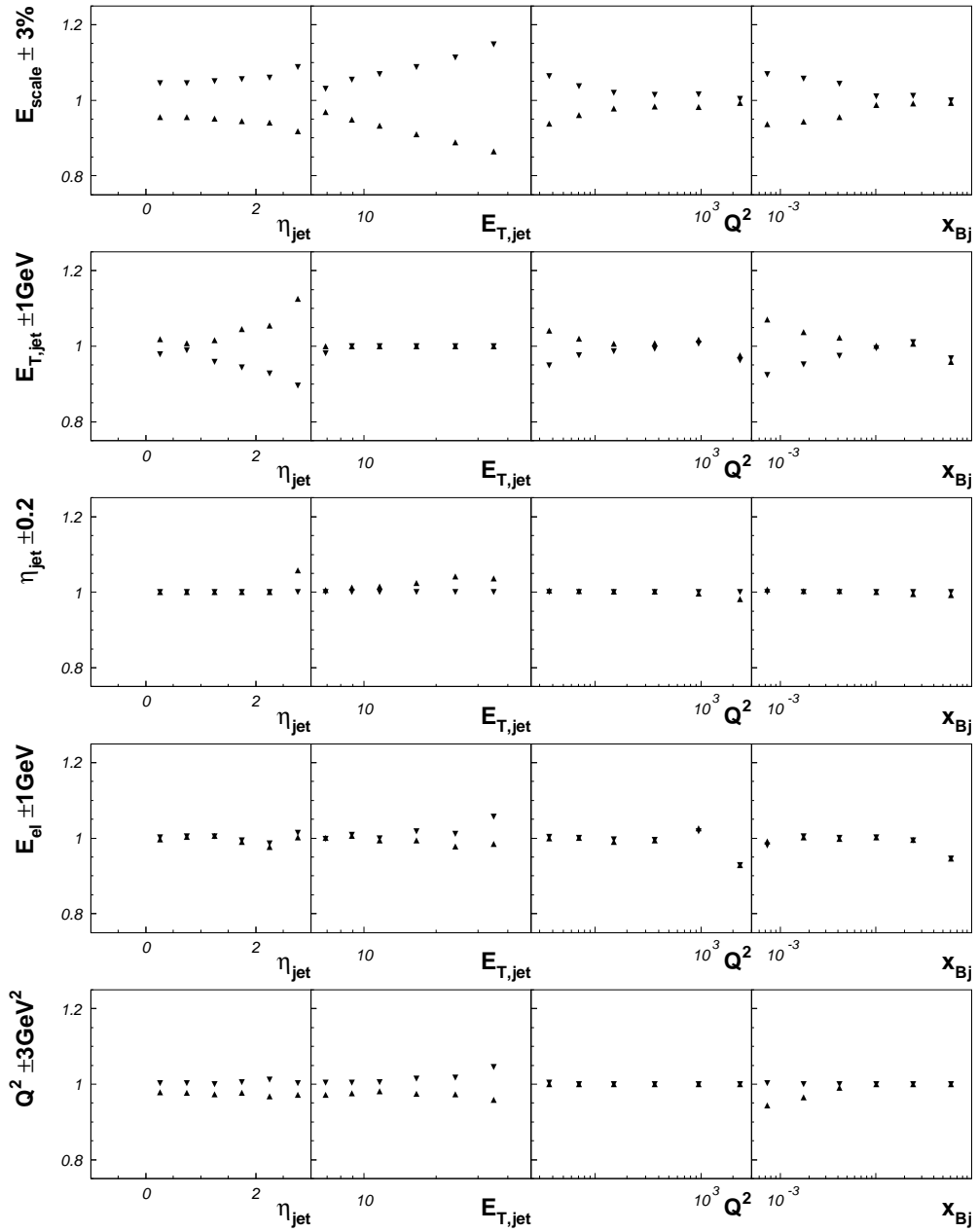


Figure 9.16: Systematic uncertainties for cross sections in the QPM Suppressed Phase Space.

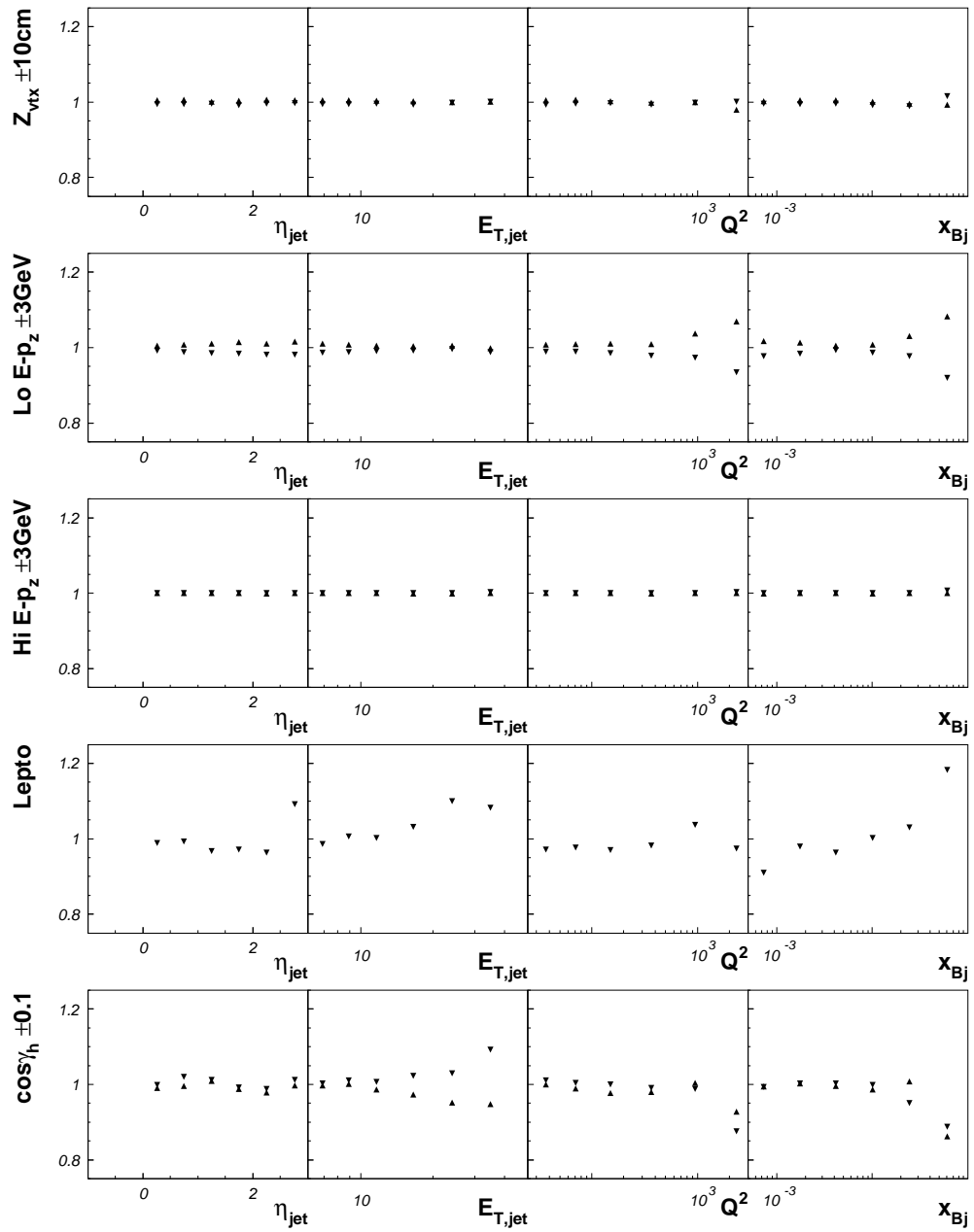


Figure 9.17: Systematic uncertainties for cross sections in the QPM Suppressed Phase Space.

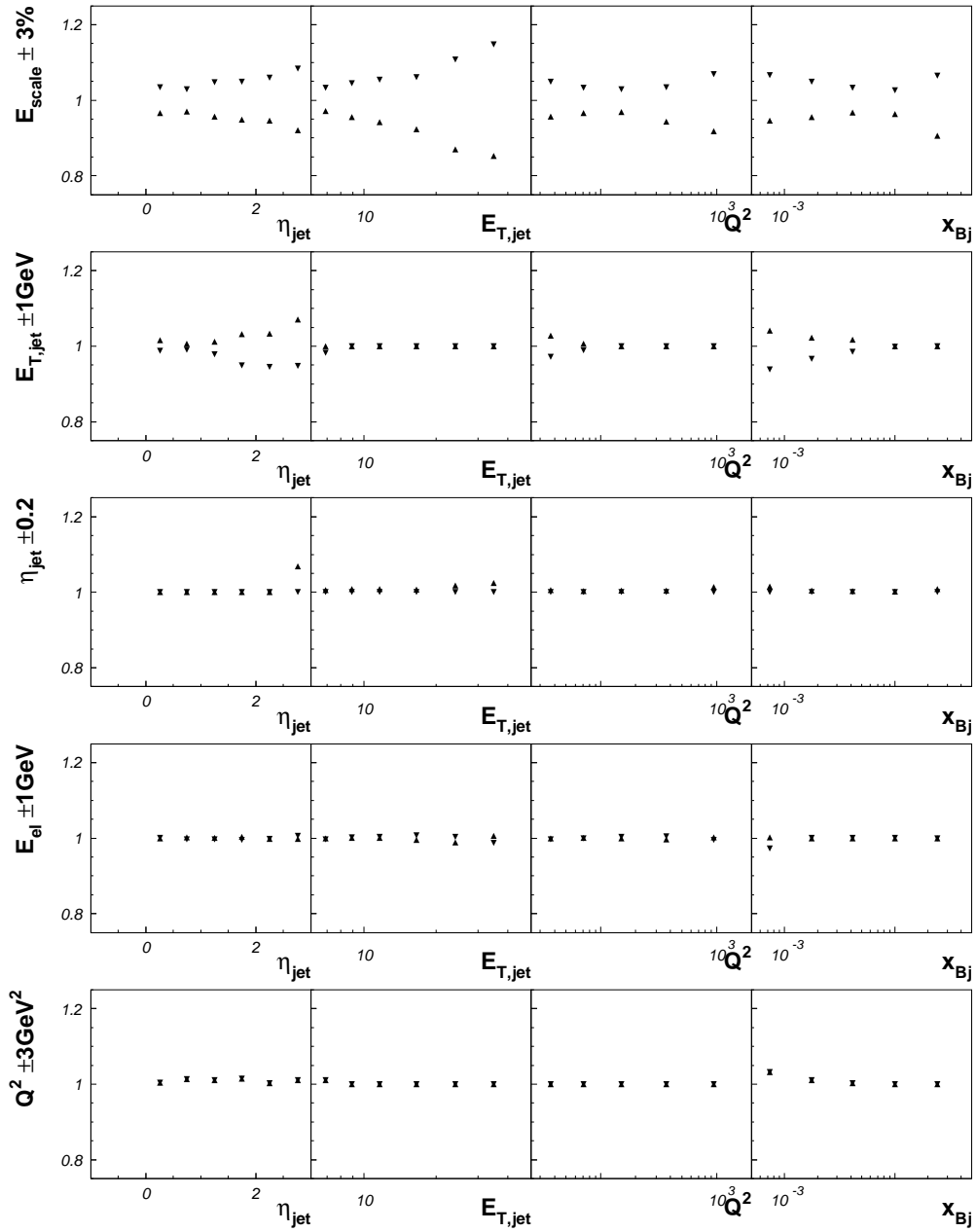


Figure 9.18: Systematic uncertainties for cross sections in the BFKL Phase Space.

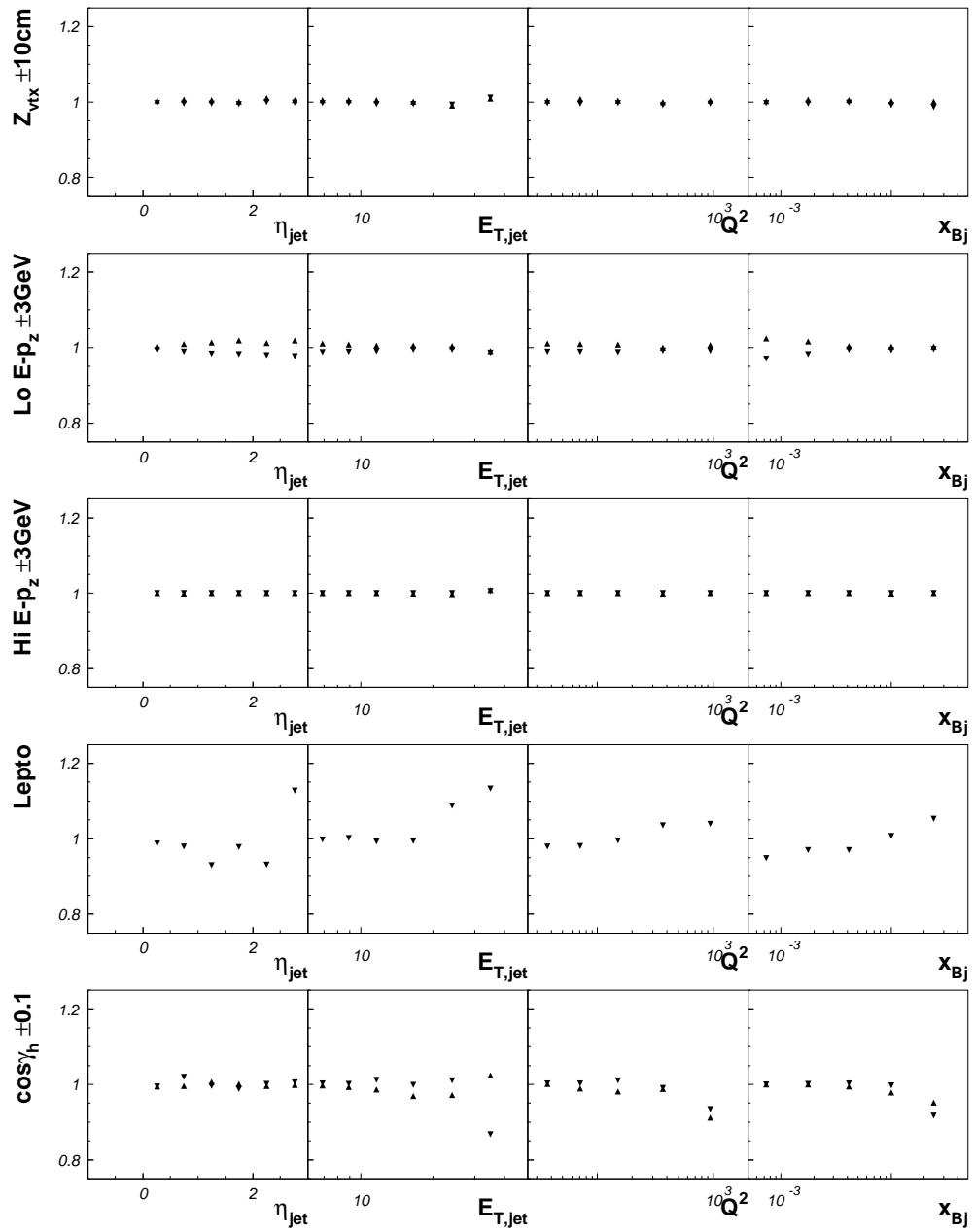


Figure 9.19: Systematic uncertainties for cross sections in the BFKL Phase Space.

The total systematic uncertainty shown on the measured cross sections is calculated by adding the individual components in quadrature. In the plots of the cross sections, the systematic uncertainty due to the calorimeter energy scale is shown separately, due to the fact that it is correlated with other errors.

Chapter 10

Conclusion

Measurements of differential cross sections in $E_{T,jet}$, η_{jet} , Q^2 and x_{Bj} for inclusive jet production in neutral current deep inelastic scattering have been presented using 38.7 pb^{-1} of ZEUS data. The low x_{Bj} region has been probed for events with $Q^2 > 25 \text{ GeV}^2$ and at least one jet with 6 GeV of transverse energy. Three phase space regions have been studied: one inclusive region, one with both an additional requirement on the hadronic angle of the event ($\cos \gamma_h < 0$) and a more limited window of jet pseudorapidity ($\eta_{jet} > 0$) (QPM Suppressed Phase Space), and one with the additional requirement $0.5 < \frac{E_{T,jet}^2}{Q^2} < 2.0$ (BFKL Phase Space). The restrictions imposed on the second phase space region enhance the dijet and multijet contributions while not restricting the transverse energy of the lower transverse energy jet(s). The added restriction for the third phase space region limits the Q^2 evolution of the partons along the gluon ladder.

The leading-logarithm parton shower calculations can describe the shape of the data in most variables, but the color-dipole model generally gives a better description of both the data shape and normalization than the parton shower model MEPS. A large excess of the data over the NLO calculation is observed in the jet cross section for the inclusive phase space at high jet η and low x_{Bj} . This excess is significantly diminished in the QPM Suppressed phase space where the cross section is dominated by boson-gluon fusion events, but the theoretical uncertainty increases significantly. The description of the data by the NLO calculation in the BFKL phase space is generally good, although a slight excess of the data over the prediction is observed at high η_{jet} . The uncertainty due to the renormalization scale uncertainty is persistently large and dwarfs all other theoretical and experimental uncertainties. Accordingly, the present theoretical limitations prevent establishing

an environment suitable for decisive tests of BFKL dynamics in these data. Improved calculations, perhaps using the BFKL approach, are needed to give a more accurate prediction in this region.

Experimental improvements in the measurement could be made by extending the jet kinematics to lower transverse energy and higher pseudorapidity. Jet reconstruction in this extended region can be studied with the Forward Plug Calorimeter that was installed inside the forward beampipe for the 1998-2000 running period and with new forward tracking components that have been added to the detector for the HERA II data collection period.

Bibliography

- [1] Donald H. Perkins. *Introduction to High Energy Physics*. Addison-Wesley Publishing Co., Inc., 1987.
- [2] David Griffiths. *Introduction to Elementary Particles*. John Wiley & Sons, 1987.
- [3] R.G. Roberts. *The Structure of the Proton*. Cambridge University Press, 1990.
- [4] S.L. Glashow. *Nucl. Phys.* 22, 579, 1961.
- [5] H. D. Politzer. *Phys Rev. Lett*, 30:1346, 1973.
- [6] D. J. Gross and F. Wilczek. *Phys Rev. Lett*, 30:1343, 1973.
- [7] F. Halzen and A.D. Martin. *Quarks and Leptons: An Introduction Course in Modern Particle Physics*. John Wiley & Sons, 1984.
- [8] M. Peskin and D.V. Schroeder. *An Introduction to Quantum Field Theory*. Addison-Wesley, 1995.
- [9] A. Martin. Lectures given at the XXI Int. Meeting on Fundamental Physics, Miraflores de la Sierra, Madrid (Spain), 1993.
- [10] S. Aid et al. A measurement and qcd analysis of the proton structure function $f_2(x, q^2)$ at hera. *Nucl. Phys.*, B470:3–40, 1996.
- [11] V.N. Gribov and L.N. Lipatov. Deep inelastic ep scattering in perturbation theory. *Sov. J. Nucl. Phys.*, 15:438, 1972.
- [12] L.N. Lipatov. The parton model and perturbation theory. *Sov. J. Nucl. Phys.*, 20:94, 1975.
- [13] Yu.L. Dokshitzer. Calculation of the structure functions for deep inelastic scattering and e^+e^- annihilation by perturbation theory in Quantum Chromodynamics [in Russian]. *JETP*, 46:641, 1977.
- [14] G. Altarelli and G. Parisi. Asymptotic freedom in parton language. B 126:298, 1977.
- [15] L.N. Lipatov E.A. Kuraev and V.S. Fadin. The Pomeranchuk singularity in nonabelian gauge theories. *JETP*, 45:199, 1977.
- [16] Ya.Ya. Balitskii and L.N. Lipatov. The Pomeranchuk singularity in Quantum Chromodynamics. *Sov. J. Nucl. Phys.*, 28:822, 1978.
- [17] M. Riveline. *Probing the Parton Evolution in DIS at Low x_{BJ} Using Jet Observables*. PhD thesis, Magill University, Montreal, 1999. DESY-THESIS 1999-005.

- [18] R.K. Ellis et al. *QCD and Collider Physics*. Cambridge Univ. Press, 1996.
- [19] A.H. Mueller. *Nucl. Phys. Proc. Suppl.*, C 18:125, 1991.
- [20] A.H. Mueller. Jets at LEP and HERA. *J. Phys.*, G 17:1443, 1991.
- [21] The zeus detector: Status report 1993. The ZEUS detector: Status report 1993, ZEUS-STATUS-REPT-1993.
- [22] M. Derrick et al.. Design and construction of the ZEUS barrel calorimeter. *Nucl. Inst. and Meth.*, A 309:77, 1991.
- [23] A. Andresen et al.. Construction and beam test of the ZEUS forward and rear calorimeter. *Nucl. Inst. and Meth.*, A 309:101, 1991.
- [24] A. Caldwell et al.. Design and implementation of a high-precision readout system for the ZEUS calorimeter. *Nucl. Inst. and Meth.*, A 321:356, 1992.
- [25] A. Bernstein et al.. Beam tests of the ZEUS barrel calorimeter. *Nucl. Inst. and Meth.*, A 336:23, 1993.
- [26] B.G. Bylsma et al.. Optical readout components for the ZEUS barrel calorimeter. *Nucl. Inst. and Meth.*, A 305:354, 1991.
- [27] N. Harnew et al.. Vertex triggering using time difference measurements in the ZEUS central tracking detector. *Nucl. Inst. and Meth.*, A 279:290, 1989.
- [28] B. Foster et al.. The performance of the ZEUS central tracking detector z -by-timing electronics in a transputer based data acquisition system. *NPPS*, B 32:181, 1993.
- [29] B. Foster et al.. The design and construction of the ZEUS central tracking detector. *Nucl. Inst. and Meth.*, A 338:254, 1994.
- [30] W.H. Smith et al.. The ZEUS calorimeter first level trigger. *Nucl. Inst. and Meth.*, A 355:278, 1995.
- [31] G.P. Heath et al.. The ZEUS first level tracking trigger. *Nucl. Inst. and Meth.*, A 315:431, 1992.
- [32] D. Kisielewska et al.. Fast luminosity monitoring at HERA. *Nukleonika*, 31:205, 1986. also in Report DESY-HERA-85-25.
- [33] A. Bamberger et al.. The presampler for the forward and rear calorimeter in the ZEUS detector. *Nucl. Inst. and Meth.*, A 382:419, 1996.
- [34] A. Bamberger et al.. The small angle rear tracking detector of ZEUS. *Nucl. Inst. and Meth.*, A 401:63, 1997.
- [35] I. Ambats et al.. Studies of hadron-electron separators for the ZEUS barrel calorimeter. *Nucl. Inst. and Meth.*, A 368:364, 1996.
- [36] J. Pumplin et al.. cteq6. *JHEP*, 0207:012, 2002.
- [37] Mats Bengtsson and Torbjorn Sjostrand. Parton showers in leptoproduction events. *Z. Phys.*, C37:465, 1988.
- [38] A. Edin G. Ingelman and J. Rathsman. LEPTO 6.5: A Monte Carlo generator for deep inelastic lepton–nucleon scattering. *Comp. Phys. Comm.*, 101:108, 1997.

- [39] Y. Azimov et al.. The string effect and QCD coherence. *Phys. Lett.*, B 165:147, 1985.
- [40] G. Gustafson. Dual description of a confined color field. *Phys. Lett.*, B 175:453, 1986.
- [41] G. Gustafson and U. Pettersson. Dipole formulation of QCD cascades. *Nucl. Phys.*, B 306:746, 1988.
- [42] B. Andersson et al.. Coherence effects in deep inelastic scattering. *Z. Phys*, C 43:625, 1989.
- [43] L. Lönnblad. ARIADNE version 4 – a program for simulation of QCD cascades implementing the colour dipole model. *Comp. Phys. Comm.*, 71:15, 1992.
- [44] L. Lönnblad. Rapidity gaps and other final state properties in the color dipole model for deep inelastic scattering. *Z. Phys*, C 65:285, 1995.
- [45] B. Andersson et al.. Parton fragmentation and string dynamics. *Phys. Rep.*, 97:31, 1983.
- [46] H. Spiesberger A. Kwiatkowski and H.-J. Möhring. HERACLES: An event generator for ep interactions at HERA energies including radiative processes (version 1.0). *Comp. Phys. Comm.*, 69:155, 1992. also in *Proc. Workshop Physics at HERA*, 1991, DESY, Hamburg.
- [47] G.A. Schuler K. Charchula and H. Spiesberger. Combined QED and QCD radiative effects in deep inelastic lepton-proton scattering: The Monte Carlo generator DJANGO6. *Comp. Phys. Comm.*, 81:381, 1994.
- [48] H. Spiesberger. HERACLES and DJANGO: *Event Generation for ep Interactions at HERA Including Radiative Processes*, 1998.
- [49] T.Kinoshita. *J. Math. Phys*, 3:650, 1962.
- [50] T.D. Lee and M. Nauenberg. *Phys. Rev.*, 133(B):1549, 1964.
- [51] S. Catani and M.H. Seymour. Disent. *Nucl. Phys.*, B 485:291 (1997). Erratum in *Nucl. Phys. B* 510, 503 (1998).
- [52] D. Graudenz. *hep-ph/9710244*.
- [53] J. Engelen S. Bentvelsen and P. Kooijman. Reconstruction of (x, Q^2) and extraction of structure functions in neutral current scattering at HERA. In W. Buchmüller and G. Ingelman, editors, *Proc. Workshop on Physics at HERA*, volume 1, page 23, Hamburg, Germany, 1992. DESY.
- [54] S.Catani et al.. Longitudinally invariant k_t clustering algorithms for hadron-hadron collisions. *Nucl. Phys.*, B406:187, 1993.
- [55] Douglas Chapin. *A Measurement of Dijet Production in Neutral Current Deep Inelastic Scattering with ZEUS at HERA*. PhD thesis, University of Wisconsin-Madison, 2001.
- [56] M. Wodarczyk. *Measurement of the F_2 structure function of the proton at HERA from 1996 and 1997 ZEUS data*. PhD thesis, University of Wisconsin, 1999.
- [57] A. Savin. Zeus-note 98-007. 1998.
- [58] M. Wodarczyk. Rcalcorr, zeus phantom library. 1998.
- [59] A. Caldwell H. Abramowicz and R. Sinkus. Neural network based electron identification in the ZEUS calorimeter. *Nucl. Inst. and Meth.*, A 365:508, 1995.
- [60] S. Chekanov et al. ZEUS Coll.. Measurement of the neutral current cross-section and F_2 structure function for deep inelastic e^+p scattering at HERA. *Eur. Phys. J.*, C 21:443, 2001.

- [61] S. Chekanov et al. ZEUS Coll.. Dijet production in neutral current deep inelastic scattering at HERA. *Eur. Phys. J., C* 23:13, 2002.
- [62] S. Lammers and D. Chapin. Zeus-note 01-006. 2001.